Experimentally testing quantum field theory concepts with spinor Bose gases far from equilibrium

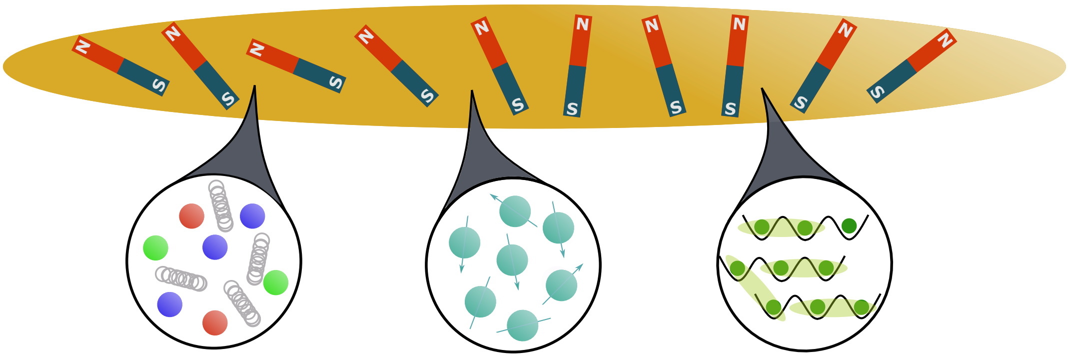

Maximilian Prüfer
2020

Dissertation
submitted to the
Combined Faculty of Natural Sciences and Mathematics
of Heidelberg University, Germany
for the degree of
Doctor of Natural Sciences

Put forward by
Maximilian Prüfer
Born in: Wiesbaden
Oral examination: 05.02.2020

Experimentally testing quantum field theory concepts with spinor Bose gases far from equilibrium

Referees:	Prof. Dr. Markus K. Oberthaler
	PD Dr. Stefan Flörchinger

Experimentally testing quantum field theory concepts with spinor Bose gases far from equilibrium

The number of parameters needed to specify the state of a many-body quantum system grows exponentially with the number of its constituents. This fact makes it computationally intractable to exactly describe dynamics and characterize the state on a microscopic level. In this thesis, we employ quantum field theory concepts for experimentally characterizing a spinor Bose gas far from equilibrium. First, we introduce the relevant concepts, which provide efficient descriptions for emerging macroscopic phenomena, in a formulation matching the capabilities of ultracold atomic systems. For our experimental study we employ a ^{87}Rb spinor Bose-Einstein condensate in a quasi-one-dimensional trap geometry. We explore the phase diagram as a function of the effective quadratic Zeeman shift by measuring the fluctuations in the spin degree of freedom and identify three distinct phases. With this knowledge, we study the instabilities which occur after an instantaneous quench across the quantum phase transition separating the different phases. These instabilities allow us to drive the system far from equilibrium in a highly controlled fashion. For long times after the quench we observe universal dynamics associated with the emergence of a non-thermal fixed point. The structure factor of the angular orientation of the transversal spin features rescaling in time and space with universal exponents as well as a universal scaling function. Using the experimental control, we probe the insensitivity of this phenomenon to details of the initial condition. Spatially resolved snapshots of the complex-valued transversal spin field allow for the extraction of one-particle irreducible correlation functions, the building blocks of the quantum effective action. We find a strong suppression of the 4-vertex at low momenta emerging in the highly occupied regime. The introduced concepts together with the presented experimental applicability give new means for studying many-body systems at all stages of their evolution: from the initial instabilities and across transient phenomena far from equilibrium to the eventual thermalization.

Experimentelle Untersuchung von quantenfeldtheoretischen Konzepten mit spinbehafteten Bose Gasen fern des Gleichgewichts

Die Anzahl der Parameter, die zur Spezifizierung des Zustandes eines Quantenvielteilchensystems erforderlich sind, wächst exponentiell mit der Anzahl seiner Bestandteile. Dies macht es auf mikroskopischer Ebene zu rechenintensiv, die Dynamik genau zu beschreiben sowie den Zustand zu charakterisieren. In dieser Arbeit verwenden wir quantenfeldtheoretische Konzepte zur experimentellen Charakterisierung eines spinbehafteten Bose Gases fern des Gleichgewichts. In einer Formulierung passend zu den experimentellen Möglichkeiten führen wir zunächst die relevanten Konzepte ein. Diese erlauben effiziente Beschreibungen emergenter makroskopischer Phänomene. Für unsere experimentelle Studie benutzen wir ein ^{87}Rb Bose-Einstein Kondensat mit Spinfreiheitsgrad in einer quasi-eindimensionalen Fallengeometrie. Wir untersuchen das Phasendiagram als Funktion der effektiven quadratischen Zeeman-Verschiebung, indem wir Fluktuationen im Spinfreiheitsgrad messen und identifizieren drei unterschiedliche Phasen. Darauf basierend untersuchen wir die Instabilitäten nach einer schnellen Parameteränderung über den Quantenphasenübergang mit Impulsauflösung. Diese Instabilitäten erlauben uns das System kontrolliert fernab des Gleichgewichts zu präparieren. Für lange Zeiten nach dem Quench beobachten wir universelle Dynamik, welche mit dem Auftreten eines nichtthermischen Fixpunktes assoziiert wird. Der Strukturfaktor der transversalen Spinorientierung reskaliert in Zeit und Raum mit universellen Exponenten und einer universellen Skalenfunktion. Mit Hilfe der experimentellen Kontrolle überprüfen wir die Insensitivität des Phänomens gegenüber Änderungen der Anfangsbedingung. Aus räumlich aufgelösten Schnappschüssen des komplexwertigen transversalen Spinfeldes extrahieren wir einteilchenirreduzibel Korrelationsfunktionen. Diese sind die Grundbausteine der quanteneffektiven Wirkung. Wir finden eine starke Unterdrückung des 4-Vertex für kleine Impulse im hochbesetzten Bereich. Zusammen mit der demonstrierten experimentellen Anwendbarkeit bieten die vorgestellten Konzepte neue Möglichkeiten, um Vielteilchensystemen in allen Stufen ihrer Entwicklung zu untersuchen: von anfänglichen Instabilitäten, über transiente Phänomene fernab des Gleichgewichts bis hin zu der schlussendlichen Thermalisierung.

Contents

List of Figures

Chapter 1

Introduction

Since the laws of quantum mechanics where postulated at the beginning of the 20th century, our understanding of fundamental processes described by quantum mechanical laws has deepened continuously [1]. From first principles, a closed quantum system is fully described by the Schrödinger equation and a Hamiltonian. Together with an initial condition, these determine all dynamical processes on a microscopic level. However, it is apparent that modelling this dynamics on the microscopic level is a nearly impossible task when dealing with large systems as complex as condensed matter materials, biological cells or our Universe [2]. This is why there is a need for effective theories giving efficient descriptions in certain limits [3].

Already in classical systems we observe that in the many-body limit macroscopic phenomena can emerge from microscopic descriptions. The probably best known example is hydrodynamics which gives quantitative predictions of the macroscopic behaviour without needing to know about explicit details of the constituents of the fluids. The idea is to write down equations, like the Navier-Stokes equation [4], which contain just a few parameters as for example viscosity [5]. These equations describe the dynamics of the fluid in terms of, e.g. , density and velocity fields – certainly only possible when looking at large length scales compared to any microscopic scale. In a general setting, solving the hydrodynamic equations is still hard, but it is in certain limits possible to obtain insights into the macroscopic dynamics, even though one has not solved a microscopic model including all details about the $\sim 10^{23}$ particles.

Exactly tracking how these macroscopic phenomena emerge from a given microscopic theory is a hard problem. A general framework for describing the emergence of macroscopic phenomena can be found in field theoretical descriptions [6, 7]. Here, the renormalization group program gives a recipe for setting up a theory at a certain length scale: rather then dealing with all length scales at once it takes them into account in an iterative fashion [8, 9]. For including all effects of quantum-statistical fluctuations one has to use *quantum field theory* (QFT), which gives efficient descriptions for quantized fields. Its efficiency is rooted in the possibility to identify the relevant degrees of freedom and to derive effective theories for their description. Phenomena unique to quantum mechanics may lead to new forms of collective behaviour in many-body systems. For example, entanglement was found to allow for thermalization of isolated many-body quantum systems [10].

Nowadays, probing theoretical predictions becomes possible with highly controlled experimental platforms. The big challenge is to access the relevant degrees of freedom including the capability to monitor them space- and time-resolved. An active and thriving field of research in this direction concerns heavy-ion collisions, for example at the LHC or RHIC. Here, the phase shortly after these little-bangs[1] where the quark-gluon plasma forms [11] is described by hydrodynamic models [12]. The subsequent transition to a thermalized state in the hadronized phase is already understood in great detail and measured particle yields are in agreement with predictions to a high precision [13]. These emergent phenomena are, however, not yet understood on all spatial and temporal scales.

In this thesis, we present a new experimental approach for probing macroscopic quantum phenomena. The approach is based on the highly controlled platform of ultracold atomic systems. Employing a large number of atoms in an appropriate trapping potential, the density can be increased such that the system can be mapped to continuous fields which are described by QFT. Further, the controllability allows for a spatially resolved readout of different observables, making the identification of relevant degrees of freedom possible [14]. Based on the spatial resolution, correlation functions of the relevant fields can be inferred. They provide an efficient way of representing the information contained in a many-body system. Combined with the experimental control this allows for characterizing the system. Especially for far-from-equilibrium situations, ultracold atomic systems offer the advantage that they may be probed at any time during the evolution and thus dynamical phenomena can be studied. Indeed, the employed methods can be applied for probing systems in stationary situations like thermal equilibrium as well. Thus, a characterization on all stages of the evolution from the initial instabilities, across transient phenomena far from equilibrium to the eventual thermalization is possible.

In the cosmological context it was discussed [15] that the described insensitivity to microscopic details may lead to new non-thermal universal phenomena even out of equilibrium. These universal phenomena feature transport of particles towards the infrared and power-law-like momentum distribution functions which are distinct from the thermal solutions [15, 16]. In this respect, ultracold atomic gases give unique experimental possibilities: Spatial resolution allows for characterizing momentum distributions and the direction of transport can be determined by probing the time evolution [17–20].

If the concept of universality far from equilibrium proves to be successful, the next step is to study the defining properties of the underlying universality classes. This task may be tackled by the high degree of control on microscopic details offered by ultracold atomic systems. Concretely, by engineering suitable Hamiltonians, one can probe the sensitivity to symmetries of interactions and determine which microscopic details are relevant respectively irrelevant. The knowledge of the fundamental building blocks opens the perspective of doing quantum simulations as well as quantum computations of problems which are theoretically hard to study [21].

---

[1] The name refers to the idea of simulating the processes that happened during the Big Bang, which unfortunately cannot be repeated and studied.

Structure of the thesis

In **Chapter 2** we start by describing different phenomena which can occur in many-body systems out of equilibrium. We present a scenario for thermalization of isolated many-body systems and introduce the notion of universality. Furthermore we motivate the need for an efficient way of extracting information from many-body systems.

In **Chapter 3** we present the quantum field theoretical concepts which are relevant in the scope of this thesis. After introducing quantum fields, we introduce the quantum effective action as the generating functional of one-particle irreducible correlation functions. In the Wigner formalism we derive a full quantum evolution equation for the particle number distribution. We review some basic results from the renormalization group approach and the O(N)-model.

In **Chapter 4** we discuss quantum simulation as well as quantum computation. For this, we give a brief definition which allows us to put the experimental observations into context.

In **Chapter 5** we present the details of the experimental setup used in this thesis. The hyperfine states of ^{87}Rb constitute a spin-1 system and we present the corresponding microscopic Hamiltonian describing the dynamics. Finally, we present schemes for probing the dynamics experimentally and elaborate on the challenges of long evolution times.

In **Chapter 6** we present a study of the phase diagram of a spin-1 system with ferromagnetic interactions. We compare our experimental study to predictions obtained within mean-field theory.

In **Chapter 7** we discuss how extreme conditions are prepared experimentally. For this we introduce Bogoliubov theory as a tool to study the quadratic fluctuations around a given mean-field ground state. This leads to predictions for the instabilities after an instantaneous quench. We study these instabilities experimentally and show that this allows us to bring the system out of equilibrium in a controlled way. We conclude by discussing spin-waves as a different way to prepare interesting initial conditions.

In **Chapter 8** we report on the observation of universal dynamics in a spinor Bose gas. After presenting the experimental parameters and concepts, we show a method for extracting the angular orientation of the transversal spin. We define the scaling regime and show the collapse of the experimental data onto a universal curve after rescaling. The experimental control allows us to study the expected insensitivity of the phenomenon to changes of the initial condition.

In **Chapter 9** we show that the spin-lifetime is enhanced by optimizing the trapping potentials. Combined with the readout of the complex valued transversal spin field we are able to observe universal dynamics for up to 40 s.

In **Chapter 10** we identify the transversal spin field as the emergent relevant degree of freedom. We show how to extract equal-time one-particle irreducible correlation functions experimentally and discuss how the significance of higher order correlations is verified. The momentum dependence of the 4-vertex is presented and we find a suppression of the 4-vertex in the highly occupied momentum regime. Finally, we investigate the time evolution of the vertices.

In **Chapter 11** we conclude by summarizing the results, before in **Chapter 12** we present an outlook on ongoing efforts and future prospects including local control and box-like trapping potentials.

In the **Appendix** we present details of Bogoliubov theory and supplementary plots on the universal dynamics observed in chapter 8. Finally, we discuss what happens when defining momentum conserving objects for correlation functions.

List of publications

- D. Linnemann, J. Schulz, W. Muessel, P. Kunkel, *M. Prüfer*, A. Frölian, H. Strobel, M. K. Oberthaler, ”Active SU(1,1) atom interferometry”, Quantum Science and Technology **2**, 044009 (2017)
- P. Kunkel, *M. Prüfer*, H. Strobel, D. Linnemann, A. Frölian, T. Gasenzer, M. Gärttner, M. K. Oberthaler, ”Spatially distributed multipartite entanglement enables EPR steering of atomic clouds”, Science **360**, 413-416 (2018)
- *M. Prüfer*, P. Kunkel, H. Strobel, S. Lannig, D. Linnemann, C.-M. Schmied, J. Berges, T. Gasenzer, M. K. Oberthaler, ”Observation of universal dynamics in a spinor Bose gas far from equilibrium”, Nature **563**, 217-220 (2018)
- C.-M. Schmied, *M. Prüfer*, M. K. Oberthaler, T. Gasenzer, ”Bidirectional universal dynamics in a spinor Bose gas close to a non-thermal fixed point”, Physical Review A **99** (3), 033611 (2019)
- P. Kunkel, *M. Prüfer*, S. Lannig, R. Rosa-Medina, A. Bonnin, M. Gärttner, H. Strobel, M. K. Oberthaler, ”Simultaneous Readout of Noncommuting Collective Spin Observables beyond the Standard Quantum Limit”, Physical Review Letters **123** (6), 063603 (2019)
- *M. Prüfer*, T. V. Zache, P. Kunkel, S. Lannig, A. Bonnin, H. Strobel, J. Berges, M. K. Oberthaler, ”Experimental extraction of the quantum effective action for a non-equilibrium many-body system”, arXiv preprint arXiv:1909.05120

Part I

Quantum field theory concepts for ultracold gases

Chapter 2

Efficient descriptions of many-body systems

We start by giving the main motivation covering this thesis: finding efficient descriptions for many-body systems. We examine this problem from two different perspectives. First, we are interested in the description of quantum many-body dynamics for systems out of equilibrium. For this we consider the general question of thermalization in the context of isolated quantum dynamics and introduce the notion of universality giving a new handle on the description of far-from-equilibrium dynamics. The second topic is concerned with efficiently determining the information content of a many-body system. Here, we introduce an encoding of information in correlation functions.

2.1 Many-body systems out of equilibrium

For the dynamics of many-body systems far from equilibrium, very little is known about possible general scenarios. Thus one is tempted to generalize or even adapt successful concepts known from equilibrium physics [22]. Prominent examples are mean-field theory, universality and renormalization group treatments. These will be discussed in more detail throughout this thesis in the context of the experimental results. Up to now there exists no general approach for generic quantum systems - only for specific situations and systems results have been achieved.

Quantum quenches

The first task when studying many-body systems far from equilibrium is the preparation of an interesting initial condition. For this we use the fact that quantum systems whose dynamics is described by a Hamiltonian $\mathcal{H}(\lambda_1, \dots, \lambda_n)$, can feature different ground states depending on the choice of the Hamiltonian parameters $\lambda_1, \dots, \lambda_n$. The qualitatively different ground state manifolds are separated by so-called *quantum phase transitions* (QPT) [23]. QPTs are strictly defined for systems at zero temperature such that the transition cannot be explained by thermal fluctuations - the phenomenon instead arises from quantum fluctuations. Preparing a system at $T = 0$ is experimentally impossible, however, characteristics of a quantum phase

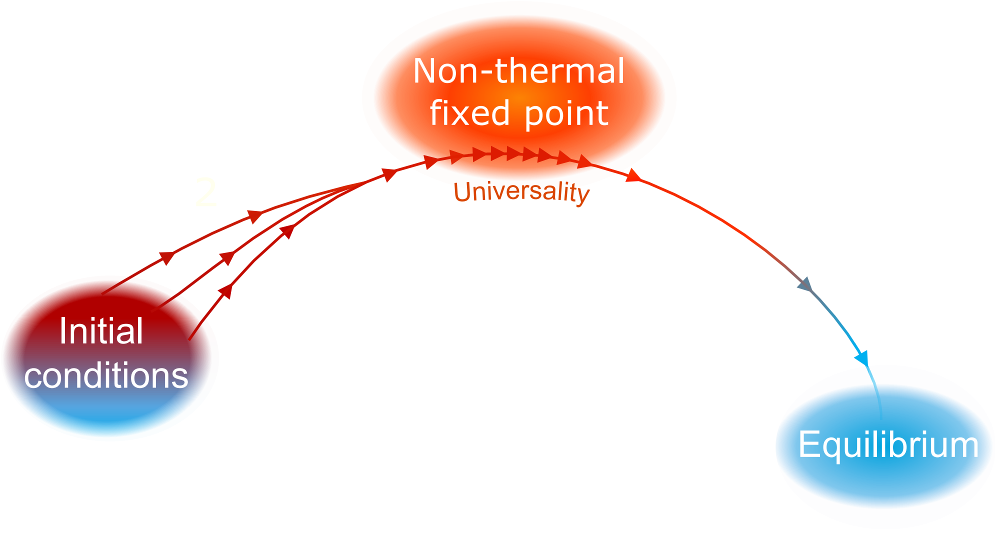

Figure 2.1: **Thermalization scenario.** We envision a generic isolated quantum system which is prepared out of equilibrium (red area). Before eventually thermalizing, the system may feature a so-called non-thermal fixed point which is characterized by universal dynamics. The universal feature is independent of the microscopic details and initial conditions as indicated by the three merging lines.

transition still manifest at $T > 0$ in the so-called quantum critical region [24]. For studying QPTs experimentally, one has to be able to change at least one Hamiltonian parameter in a controlled way. It turns out that the control offered by ultracold atomic systems enables these studies which has been shown for various systems [25–28].

Knowing the underlying phase diagram of a given system allows the implementation of *quantum quenches* [29]. To implement such a quantum quench, one prepares the system at a fixed set of parameters in the corresponding ground state and subsequently employs a rapid change of one (or few) parameters in the vicinity or across a quantum phase transition. After the quench the wavefunction gets projected onto the new eigenmodes of the Hamiltonian and therefore the system is out of equilibrium. In the following, we discuss possible scenarios which can be encountered after such a quench.

Thermalization of quantum systems

Isolated quantum many-body systems exhibit unitary time evolution following a quench [30]. Even though the global system remains pure, these systems are believed to thermalize in the long-time limit [10, 31, 32]. Thermalization is signalled by local observables that become describable by a statistical ensemble. This is possible as entropy can be generated in subsystems by the build-up of entanglement [33]. One exception from this paradigm are integrable systems which exhibit as many conserved quantities as degrees of freedom [34, 35] and thus in principle do not thermalize. However, in realistic scenarios there always exists a small integrability-breaking term eventually leading to thermalization. Transiently these system can feature prethermalization [36]. Here, after a quench the system exhibits equipartition of the new eigenmodes and dephasing leads to loss of coherences. This results in a thermal-like state with a temperature that differs from the final equilibrium temperature [37]. In this regime the system may be described by a generalized Gibbs ensemble and revivals can occur given the integrability-breaking perturbation is small enough. These phenomena have been observed experimentally in split 1D Bose gases [38–40]. Also many-body localized systems [41–43] do not thermalize. In this case all eigenstates get localized leading to the absence of transport [44].

The scenario which we consider is schematically depicted in Fig. 2.1. An isolated quantum system is prepared far out of equilibrium. Before eventually thermalizing the system may exhibit universal dynamics which is associated to the existence of *non-thermal fixed points* [15]. In the vicinity of a non-thermal fixed point the system features universal dynamics which is connected to an effective loss of detail about microscopic parameters and the initial condition. The simple descriptions in terms of universal scaling functions and exponents may allow for a classification of quantum systems far from equilibrium (see [45, 46] for reviews).

The concept of universality

In this section we elaborate in more detail on the concept of universality which is a central topic of this thesis. Universality refers to the observation that a large class of systems can behave very similar independent of the details of the microscopic description [47], which is already known in statistical physics [48]. It is a very successful concept for systems close to equilibrium in the vicinity of a temperature phase transition [49–51]. In the many-particle limit a system can get universal as the correlation length diverges at a critical point and microscopic details become irrelevant. In this regime the concept of universality is well understood for example by the renormalization group approach [8]. Within the renormalization program one identifies relevant, marginal and irrelevant operators and it turns out that systems whose microscopic description just differ by irrelevant operators show the same macroscopic phenomena. Only a few global parameters are then enough to describe the systems and they may be grouped into universality classes. These are known to depend on dimensionality and the relevant symmetry governing the microscopic description.

Universality is signalled by the phenomenon of scaling. Scaling means that certain observables become self-similar under the rescaling of a parameter. Scaling close to a quantum phase transition can be probed experimentally by an adiabatic preparation of the ground-state and the measurement of e.g. the correlation length as a function of the distance to the critical point [52]. Further, one can probe this feature dynamically using the so-called Kibble-Zurek mechanism [53–55]. Here, a non-adiabatic but not infinitely fast quench across a quantum phase transition is employed which creates topological defects as the system cannot follow the change of the parameter. From empirical arguments one can deduce scaling laws of the defect density as a function of the ramp speed. This was experimentally observed both in the mean-field limit [56, 57] as well as in the quantum regime [58, 59]. In these experiments the system was probed at a fixed time after the quench and one finds self-similarity of e.g. correlation functions for different ramp speeds.

Up to now we considered universality in a sense that one finds scaling in a Hamiltonian parameter. However, it is possible to extend the concept to dynamical phenomena where the time evolution may get universal and the scaling ”parameter” is the evolution time itself. This is well known from phase ordering kinetics in temperature-driven systems [60] where topological defects created by a quench across a temperature phase transition dissolve in the course of the dynamics and thereby lead to coarsening of equilibrium-like domains of the order parameter. For example a typical domain size will scale as $t^{1/z}$ where z is the dynamical critical exponent belonging to a certain phase.

In isolated quantum systems far from equilibrium the concept of universal dynamics is well studied numerically and has been found in examples as different as the reheating process in inflationary universe cosmology [61, 62], the dynamics of nuclear collision experiments described by quantum chromodynamics [63, 64], or the post-quench dynamics in dilute quantum gases in non-relativistic quantum field theory [65–69]. A rigorous analytical treatment is, however, missing, e.g. a proper renormalization group treatment with time as parameter is still not fully developed. Far from equilibrium universality is identified through the scaling of the spatio-temporal evolution of the system, captured by universal exponents and functions. The dynamics of an observable, for example the occupation number distribution $f(k,t)$, is described by

$$f(k,t) = t^{\alpha} f_{\mathrm{S}}\big(t^{\beta} k\big) \ , \tag{2.1}$$

with a scaling function f_{S} and the universal exponents α, describing the amplitude change, and β, describing the change of the typical length scale. From equilibrium it is known that universal phenomena are connected to the existence of fixed points in a renormalization group treatment. Transferring this concept to the far-from-equilibrium scenario discussed here, the idea is that universality classes may be connected to the existence of so-called non-thermal fixed points. In contrast to close-to-equilibrium, the same system with the same microscopic parameters can feature different non-thermal fixed points [70–72].

Universality far from equilibrium is believed to occur in systems in extreme conditions - featuring either large couplings or high occupations. Here, we consider initial instabilities producing large occupations for a certain range of momenta; in numerical simulations this situation is often produced by employing a box-like initial occupation up to a characteristic scale.

2.2 Efficiently extracting information from a many-body quantum system

Here, we want to discuss the question how to handle the amount of information “stored” in a many-body quantum system and how to efficiently extract the relevant details.

Employing the formalism of quantum mechanics one is used to the density matrix $\hat{\rho}$ being the object containing all information about the quantum many-body system. From the density matrix the expectation values of every operator $\mathcal{O}$ can be deduced as $O = \langle \mathcal{O} \rangle = \operatorname{tr}\{\hat{\rho}\mathcal{O}\}$. However, the size of the density matrix for a system with f degrees of freedom and N particles scales as $\propto \left(f^N\right)^2$. This exponential scaling in the number of constituents impedes a complete characterization of the quantum state in the many-body limit which is in the case of few qubit systems achieved by tomography [73–75].

Here, we pursue a different idea based on correlation functions. We later introduce the notion of quantum field theory and interpret the fluctuating field $\hat{\psi}_x$ describing the system as a random variable drawn from an underlying probability distribution characterizing the quantum system. By measuring the field $\hat{\psi}_x$ several times, one can measure the full distribution function. This is an arduous quantity to interpret as it is a high dimensional object. Indeed, the information about the system is equivalently stored in the moments of the random variable, i.e. the correlation functions of the field (see section 3.1). The complexity is encoded in the fact that one has to know all orders of correlation functions $\langle \hat{\psi}_{a_1} \cdots \hat{\psi}_{a_n} \rangle$ which is a multivariate problem as the field $\hat{\psi}_a$ has a dependence on spatial and internal degrees of freedom. This seems to be no simplification of the extraction, however, it turns out that there exist situations where only a few degrees of freedom become relevant and only the lowest orders of the correlation functions need to be extracted. Further, the reduction to experimentally observable expectation values of the underlying quantum fields maps the problem onto the ability to measure higher-order correlation functions in synthetic quantum systems [44, 76–78].

Chapter 3

An experimentalist's view on quantum field theory

In this chapter we want to motivate why quantum field theory can give (efficient) theoretical descriptions for many-body systems realized by ultracold atomic gases. For this we introduce and motivate a field notation in second quantization. This formalism allows us to employ formulations for an arbitrary number of particles. At the same time it provides an elegant way incorporating bosonic (fermionic) symmetries via the corresponding commutation relation of the field operators. We elucidate the relevant concepts, the underlying structure and the similarities to the quantum mechanical description based on the density matrix from an experimentalist's point of view[1]. Further we introduce the quantum effective action as the generating functional for one-particle irreducible correlation functions. We use the Wigner formalism to deduce a full quantum evolution equation for two-point correlation functions. Finally, we comment the notion of running couplings and the $O(N)$-model.

3.1 Quantum fields

Using quantum mechanics, the description of systems with many particles or even systems with changing number of particles is a tedious task. Hence, we introduce in this section the basic notion of quantum fields giving access to efficient descriptions for these cases.

Basic notion of fields

Here, we deal with bosonic particles and therefore start by defining *bosonic creation* and *annihilation operators* $\hat{a}_p^\dagger$ and $\hat{a}_p$ which create and annihilate a particle in the mode p, respectively [79]. This means they act on a Fock state $|N_1, \ldots, N_p, \ldots\rangle$ like

$$\hat{a}_p^\dagger \, |N_1, \ldots, N_p, \ldots\rangle = \sqrt{N_p + 1} \, |N_1, \ldots, N_p + 1, \ldots\rangle \tag{3.1}$$

---

[1] This is an overview of the concept necessary for this thesis. When possible we try to add information and references for the interested reader. Technical parts are, however, impossible to avoid.

and

$$\hat{a}_p \left| N_1, \ldots, N_p, \ldots \right\rangle = \sqrt{N_p} \left| N_1, \ldots, N_p - 1, \ldots \right\rangle \,. \tag{3.2}$$

The Fock states are described by having N_p particles in the mode p with mode functions $\varphi_p(\vec{r})$, which are for example plain waves or modes of an external trapping potential. The mode functions constitute a complete orthonormal basis set. For bosons the operators fulfil the defining commutation relations

$$\left[\hat{a}_p, \hat{a}_k^\dagger\right] = \delta_{pk} \qquad \text{and} \qquad \left[\hat{a}_p^{(\dagger)}, \hat{a}_k^{(\dagger)}\right] = 0, \tag{3.3}$$

with the Kronecker delta $\delta_{pp} = 1$. For fermions the commutator is replaced by the anticommutator.

We define the bosonic *field operator* $\hat{\psi}(\vec{r}) = \sum_p \hat{a}_p \varphi_p(\vec{r})$ which fulfils the commutation relation

$$\left[\hat{\psi}(\vec{r}), \hat{\psi}^\dagger(\vec{r'})\right] = \delta(\vec{r} - \vec{r'}) \qquad \text{and} \qquad \left[\hat{\psi}^{(\dagger)}(\vec{r}), \hat{\psi}^{(\dagger)}(\vec{r'})\right] = 0\,. \tag{3.4}$$

This formulation of quantum physics in a field-quantized notation (or second-quantized notation) is inherently many-body, as it can deal with an arbitrary number of particles and modes in an efficient way and respects by definition the bosonic (fermionic) exchange symmetry [80].

Many-body operators

Given this notation we have to find an expression for single- and two-particle operators [81]. Generally, a one-particle operator $\mathcal{O}$ with matrix elements $\mathcal{O}_{pp'}$ is written in second-quantized form as

$$\hat{\mathcal{O}} = \int \mathrm{d}\vec{r}\, \hat{\psi}^\dagger(\vec{r}) \mathcal{O}(r) \hat{\psi}(\vec{r}) \equiv \int \mathrm{d}\vec{r} \sum_{pp'} \hat{a}_p^\dagger \varphi_p^*(\vec{r}) \mathcal{O}_{pp'} \hat{a}_{p'} \varphi_{p'}(\vec{r})\,. \tag{3.5}$$

We can extend this quite naturally to two-particle operators $\mathcal{U}$ by writing

$$\hat{\mathcal{U}} = \int\int \mathrm{d}\vec{r} \mathrm{d}\,\vec{r'}\, \hat{\psi}^\dagger(\vec{r}) \hat{\psi}^\dagger(\vec{r'}) \mathcal{U}(r, r') \hat{\psi}(\vec{r}) \hat{\psi}(\vec{r'})\,. \tag{3.6}$$

As an example we can take the operator describing the probability for finding a particle at location $\vec{r}$ which is written as $n(\vec{r}) = \sum_i \delta(\vec{r} - \vec{r_i})$ and find

$$\hat{n}(\vec{r}) = \hat{\psi}^\dagger(\vec{r}) \hat{\psi}(\vec{r})\,. \tag{3.7}$$

With that the operator for the total atom number reads $\hat{N} = \int \mathrm{d}r\, \hat{\psi}^\dagger(\vec{r}) \hat{\psi}(\vec{r})$.

Time evolution

Time evolution is described by the many-body Hamiltonian $\hat{\mathcal{H}}$ which originates from the Hamiltonian operator $\mathcal{H}$ as described in the preceding section; the specific form for our system will be given explicitly later in chapter 5. In the so-called Schrödinger picture we can deduce the evolution equation for the state

$$|\psi\rangle = |x_1 \cdots x_N\rangle = \frac{1}{N!}\hat{\psi}^\dagger(x_1)\cdots\hat{\psi}^\dagger(x_N)\,|0\rangle \tag{3.8}$$

from the single-particle Schrödinger equation [82] and find

$$\hat{\mathcal{H}}\,|\psi\rangle = i\hbar\partial_t\,|\psi\rangle\ . \tag{3.9}$$

The field formulation offers a convenient description as the number of particles has not to be specified for formulating the Schrödinger equation.

Instead of the state being time-dependent, the Heisenberg picture employs time-dependent field operators. The Heisenberg equation of motion reads

$$\partial_t\hat{\psi} = i\hbar\left[\hat{\mathcal{H}},\hat{\psi}\right]\ , \tag{3.10}$$

where $[\cdot,\cdot]$ is the commutator. For time-independent Hamiltonians this leads to a general solution

$$\hat{\psi}^{(\dagger)}(t) = \mathrm{e}^{i\hat{\mathcal{H}}t}\hat{\psi}^{(\dagger)}(0)\mathrm{e}^{-i\hat{\mathcal{H}}t}\,, \tag{3.11}$$

where one has to specify an initial condition $\hat{\psi}(0)$. Solving this equation in the many-particle case for an interacting Hamiltonian is as hard as solving the Schrödinger equation for the same number of particles. However, quantum field theory gives efficient means for producing approximate solutions in some cases.

3.2 Correlation functions

A system in the pure state $|\psi\rangle$ is fully described by the density matrix $\hat{\rho} = |\psi\rangle\langle\psi|$. We want to present a different way of representing a quantum system, which is more common in quantum field theoretical descriptions and is based on correlation functions. The full information about a quantum system is equally contained in all correlation functions of the type $\langle\hat{\psi}_{a_1}\cdots\hat{\psi}_{a_n}\rangle = \mathrm{tr}\left\{\hat{\rho}\,\hat{\psi}_{a_1}\cdots\hat{\psi}_{a_n}\right\}$. As all operators can be expressed in terms of the field (see. Eq. (3.5)), the correlation functions can also be interpreted as the collection of the expectation values of all possible observables.

One can view the fluctuating field $\hat{\psi}$ as a multivariate random variable. With that the correlation functions are the *multivariate cumulants* of the this random variable. In analogy to statistical descriptions, we introduce generating functionals in the next section.

3.3 The quantum effective action - from microscopic to macroscopic fields

In general, there exist different types of generating functionals. They all carry the same information content and the best-suited functional depends on details of the calculation. We first introduce the generating functionals for the full correlation functions $Z[J]$ and for the connected correlation functions $E[J]$. Finally a Legendre transform yields the quantum effective action $\Gamma[\phi]$, the generating functional of the one-particle irreducible correlation functions.

Disconnected and connected correlation functions

To collect all correlation functions we define $Z[J] = \mathrm{tr}\left\{\hat{\rho}\mathrm{e}^{J_a\mathcal{O}_a}\right\}$, where Einstein's sum convention, i.e. summing over repeated indices is used. It generates the full correlation functions by

$$\left.\frac{\delta^n Z[J]}{\delta J_{a_1}\cdots\delta J_{a_n}}\right|_{J=0} = \langle\mathcal{O}_{a_1}\cdots\mathcal{O}_{a_n}\rangle\,. \tag{3.12}$$

where the so-called sources J_a correspond to the observable $\mathcal{O}_a$ and are time independent. We indicate functional derivatives with respect to J by $\frac{\delta}{\delta J}$.

The full correlation functions can be decomposed into a so-called connected and disconnected part

$$\langle\mathcal{O}_{a_1}\cdots\mathcal{O}_{a_n}\rangle = \langle\mathcal{O}_{a_1}\cdots\mathcal{O}_{a_n}\rangle_{\text{conn}} + \langle\mathcal{O}_{a_1}\cdots\mathcal{O}_{a_n}\rangle_{\text{dis}}\,. \tag{3.13}$$

The disconnected part contains redundant information of lower order correlation functions. Thus, we proceed by defining the generating functional of the connected correlation functions $E[J] = \log Z[J]$. Up to fourth order, the connected correlators are given by

$$O_a = \left.\frac{\delta E}{\delta J_a}\right|_{J=0} = \langle\mathcal{O}_a\rangle\,, \tag{3.14a}$$

$$C_{ab} = \left.\frac{\delta^2 E}{\delta J_a\delta J_b}\right|_{J=0} = \langle\mathcal{O}_a\mathcal{O}_b\rangle - O_aO_b\,, \tag{3.14b}$$

$$C_{abc} = \left.\frac{\delta^3 E}{\delta J_a\delta J_b\delta J_c}\right|_{J=0} = \langle\mathcal{O}_a\mathcal{O}_b\mathcal{O}_c\rangle - C_{ab}O_c - C_{bc}O_a - C_{ca}O_b + 2O_aO_bO_c\,, \tag{3.14c}$$

$$\begin{aligned}C_{abcd} = \left.\frac{\delta^4 E}{\delta J_a\delta J_b\delta J_c\delta J_d}\right|_{J=0} &= \langle\mathcal{O}_a\mathcal{O}_b\mathcal{O}_c\mathcal{O}_d\rangle - C_{abc}O_d - C_{cbd}O_a - C_{cda}O_b - C_{dab}O_c\\ &\quad - C_{ab}C_{cd} - C_{ac}C_{db} - C_{ad}C_{bc} - 6O_aO_bO_cO_d\\ &\quad + 2C_{ab}O_cO_d + 2C_{ac}O_dO_b + 2C_{ad}O_bO_c + 2C_{bc}O_dO_a + 2C_{bd}O_aO_c + 2C_{cd}O_aO_b\,.\end{aligned} \tag{3.14d}$$

Here, we explicitly see that the disconnected part of order n can be rewritten in sums of products of lower order correlation functions.

One-particle irreducible correlation functions

The names *connected* and *disconnected* can be understood in terms of the pictorial representation as Feynman diagrams [83]. Connected correlation functions are represented by a single diagram in which all points are connected (see Fig. 3.1).

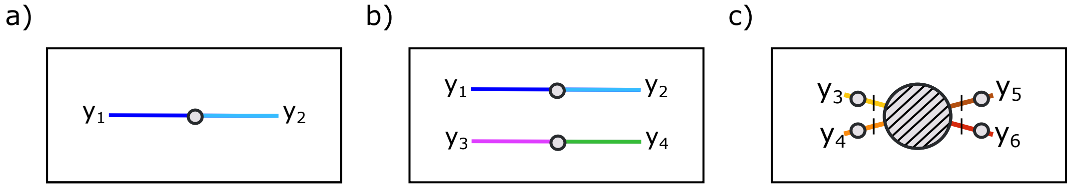

Figure 3.1: **Pictorial representation of correlation functions.** a) Connected two-point correlation functions are indicated by a coloured line and a grey circle. b) Disconnected correlation function which can be written as $\langle \mathcal{O}_{y_1} \mathcal{O}_{y_2} \rangle \langle \mathcal{O}_{y_3} \mathcal{O}_{y_4} \rangle$. c) Connected four-point correlator. It still contains information of two-point correlation functions which can be detached to obtain the four-point one-particle irreducible correlation function represented by the hatched circle.

Going even one step further it is possible to obtain the information only from tree-like diagrams [84]. Tree-like means that the diagrams are just build-up out of lines, the propagators represented by two-point functions, and effective interaction vertices. The interaction vertices are represented by the so-called *one-particle irreducible correlation functions* (short: 1PI correlation functions). Once one obtained the 1PI correlators the calculation of every diagram is done by multiplication of propagators and vertices. The complexity, though, is encoded in obtaining the 1PI vertices.

The 1PI correlation functions are obtained by their generating functional

$$\Gamma[O] = -\log Z[J(O)] + J_a(O) O_a \,, \tag{3.15}$$

which is the functional Legendre transformation of $E[J]$. When doing this transformation explicitly one has to solve the equation $O(J) = \frac{\delta E}{\delta J}$ to obtain $J(O)$. The 1PI correlators are given by

$$\Gamma_a = \left.\frac{\delta \Gamma}{\delta O_a}\right|_{O=\langle \mathcal{O} \rangle} = 0 \,, \tag{3.16a}$$

$$\Gamma_{ab} = \left.\frac{\delta^2 \Gamma}{\delta O_a \delta O_b}\right|_{O=\langle \mathcal{O} \rangle} = \left[\left(\left.\frac{\delta^2 E}{\delta J \delta J}\right|_{J=J(O)} \right)^{-1} \right]_{ab} \,, \tag{3.16b}$$

$$\Gamma_{abc} = \left.\frac{\delta^3 \Gamma}{\delta O_a \delta O_b \delta O_c}\right|_{O=\langle \mathcal{O} \rangle} = -\Gamma_{aa'} \Gamma_{bb'} \Gamma_{cc'} C_{a'b'c'} \,, \tag{3.16c}$$

$$\begin{aligned} \Gamma_{abcd} = \left.\frac{\delta^4 \Gamma}{\delta O_a \delta O_b \delta O_c \delta O_d}\right|_{O=\langle \mathcal{O} \rangle} &= -\Gamma_{aa'} \Gamma_{bb'} \Gamma_{cc'} \Gamma_{dd'} C_{a'b'c'd'} \\ &+ \Gamma_{aa'} \Gamma_{bb'} \Gamma_{cc'} \Gamma_{dd'} \left(C_{a'b'e} \Gamma_{ef} C_{fc'd'} + C_{a'c'e} \Gamma_{ef} C_{fb'd'} + C_{a'd'e} \Gamma_{ef} C_{fc'b'} \right) . \end{aligned} \tag{3.16d}$$

Quantum effective action

There are two motivations for introducing the 1PI correlation functions: First, it is a different way of sorting the information contained in the many-body system one wants to describe. Second, we introduced the generating functional of the 1PI correlators which is called the *quantum effective action.* By performing the Legendre transform Γ is no longer a functional of the sources but of the expectation value $O_a = \langle \mathcal{O}_a \rangle$, the so-called *macroscopic field* . Thus, it gives rise to an equation for the macroscopic field $O_a = \langle \mathcal{O}_a \rangle$ (see next section). The quantum effective action includes the effects of all quantum-statistical fluctuations [85] (cf. Eq. (3.21)) and with this may be viewed as the quantum analogue of the classical action.

3.4 Wigner formalism and the full quantum evolution equation

Coming historically from a relativistic physics point-of-view, time and space are treated on the same footing and the index $x = (t, x_0)$ collectively denotes these two. So QFT is formulated in terms of correlation functions

$$\langle \hat{\psi}_{x_1} \hat{\psi}_{x_2} \cdots \hat{\psi}_{x_n} \rangle = \mathrm{tr} \left[\hat{\rho} \mathcal{T} \hat{\psi}_{x_1} \hat{\psi}_{x_2} \cdots \hat{\psi}_{x_n} \right] ,$$

where in principle these correlators connect also different evolution times and $\mathcal{T}$ ensures time-ordering. This is natural for example when describing the processes happening in a heavy-ion collision. Here, two free particles starting at time $t = -\infty$ interact at some instance in time and propagate afterwards as free particles again until the time $t = +\infty$. Experimentally, the times are of course finite but large compared to any interaction timescale. From the point-of-view of an ultracold atom experimentalist a formulation based on equal-time correlation functions is much more natural. Usually the dynamics is recorded with single-time snapshots as destructive imaging methods are employed [30]. This allows for the extraction of equal-time correlation functions only.

Following the preceding reasoning, we now employ[2] an alternative but equivalent formulation of quantum field theory based on equal-time quantities [87]. Explicitly, we consider a system which depends only on the two canonically conjugate fields $\hat{\psi}$, $\hat{\psi}^\dagger$. For finding an efficient description of the generating functionals in the equal-time formalism we employ the Wigner formalism. It is a representation of quantum dynamics in phase space spanned by the coordinates ψ, ψ^* [88]. Further the symmetric ordering of the correlation functions is natural to the results obtained in ultracold atomic systems. In this language every operator $\hat{\mathcal{O}} \left[\hat{\psi}, \hat{\psi}^\dagger \right]$ is substituted by its corresponding Weyl symbol $\mathcal{O}_W$ obtained by the Wigner-Weyl transform. Explicitly we obtain the Wigner functional $W_t \left[\psi, \psi^* \right]$ at some evolution time t which is the Wigner-Weyl transform of the density matrix $\hat{\rho}_t \left[\hat{\psi}, \hat{\psi}^\dagger \right]$:

$$W_t \left[\psi, \psi^* \right] = \int \mathcal{D}\eta \mathcal{D}\eta^* \, \langle \psi_x - \frac{\eta_x}{2} | \, \hat{\rho}_t \left[\hat{\psi}_x, \hat{\psi}_x^\dagger \right] | \psi_x + \frac{\eta_x}{2} \rangle \, \mathrm{e}^{-\int_x \left[\psi_x^* \psi_x + \frac{1}{4} \eta_x^* \eta_x + \frac{1}{2} \left(\psi_x^* \eta_x - \eta_x^* \psi_x \right) \right]} . \tag{3.17}$$

---

[2] This section has partial overlap with the Methods of [86].

The complex integral measures $\mathcal{D}\eta$ and $\mathcal{D}\eta^*$ are defined by

$$\mathcal{D}\eta\mathcal{D}\eta^* = \prod_x \left[\frac{1}{\pi} d\mathrm{Re}\left(\eta_x\right) d\mathrm{Im}\left(\eta_x\right)\right] . \tag{3.18}$$

From the definition we see that the Weyl symbol is like a "Fourier"-transform of the matrix elements of the operator in the coherent state basis into phase space coordinates[3]. The exponential factor in the fields and η's comes from the fact that the coherent states are an over-complete basis.

W_t is the field theoretic version of the Wigner distribution which is extensively employed in quantum optics [89]. Here, we introduced the coherent state $|\psi\rangle$, which is an eigenstate of the annihilation operator, i.e. $\hat{\psi}\,|\psi\rangle = \psi\,|\psi\rangle$. The Wigner functional represents a quasi-probability distribution of the phase space variables and quantum expectation values of operators can be obtained as the average of the corresponding Weyl symbol weighted by the Wigner functional. The von-Neumann equation for the density matrix $i\partial_t\hat{\rho}_t = \left[\hat{\mathcal{H}}, \hat{\rho}_t\right]$ directly translates into an evolution equation for the Wigner functional. Thus, the time evolution can be obtained in the phase space representation from the Weyl symbol $\mathcal{H}_W$ of the Hamiltonian.

To obtain the time evolution of the equal time correlation functions we define the generating functional Z_t, constructed as

$$Z_t[J, J^*] = \mathrm{Tr}\left[\hat{\rho}_t\, e^{\int_x\left(J_x\hat{\psi}^\dagger_x + J^*_x\hat{\psi}_x\right)}\right] = \int \mathcal{D}\psi\mathcal{D}\psi^*\, W_t[\psi, \psi^*]\, e^{\int_x\left(J_x\psi^*_x + J^*_x\psi_x\right)} . \tag{3.19}$$

Here, we directly see that $Z_t[J, J^*]$ is constructed analogously to the moment generating functional in statistics. Z_t generates symmetrically ordered equal-time correlation functions of the two fields. The complex integral measures $\mathcal{D}\psi$ and $\mathcal{D}\psi^*$ in Z_t are implicitly defined by Eq. (3.18). In the employed formalism the quantum effective action Γ_t corresponding to Z_t is given by

$$\Gamma_t\left[\Psi, \Psi^*\right] = -\log Z_t\left[J\left(\Psi, \Psi^*\right), J^*\left(\Psi, \Psi^*\right)\right] + \int_x \left[J^*\left(\Psi, \Psi^*\right)\Psi_x + \Psi^*_x J\left(\Psi, \Psi^*\right)\right] \tag{3.20}$$

where J,J^* implicitly depend on Ψ, Ψ^* due to the Legendre transform and $\Psi = \langle\hat{\psi}\rangle = \frac{\delta Z}{\delta J^*}$ is the expectation value of the field. Going from W_t to Γ_t represents a change of description from fluctuating (microscopic) fields ψ to averaged (macroscopic) fields Ψ. This fact becomes even more visible in the identity

$$e^{-\Gamma_t[\Psi,\Psi^*]} = \int \mathcal{D}\psi\mathcal{D}\psi^*\, W_t[\psi, \psi^*]\, e^{\int_x\left[J_x\left(\psi^*_x - \Psi^*_x\right) + J^*_x\left(\psi_x - \Psi_x\right)\right]} , \tag{3.21}$$

which directly follows from the construction of the quantum effective action in Eq. (3.20). The equation explicitly includes an integral over the fluctuating phase space variables. As already mentioned the quantum effective action plays the role

---

[3] This is not directly apparent as η and η^* are complex variables and thus the i in the exponential is missing. It can be recovered by transforming the integral to the real and the imaginary part of η.

of the classical action for the quantum system including all quantum-statistical fluctuations giving an equation for the average field Ψ with

$$\frac{\delta \Gamma_t}{\delta \Psi} = J^* \, . \tag{3.22}$$

The 1PI correlators $\Gamma_t^{\alpha_1,\ldots,\alpha_n}(x_1,\ldots,x_n)$ (cf. Eq. (3.16)) are obtained via

$$\Gamma_t^{\alpha_1,\ldots,\alpha_n}(x_1,\ldots,x_n) = \left.\frac{\delta^n \Gamma_t[\Psi,\Psi^*]}{\delta \Psi_{x_1}^{\alpha_1}\cdots\delta\Psi_{x_n}^{\alpha_n}}\right|_{\langle\psi\rangle} \, . \tag{3.23}$$

Here, α_i denotes the presence/absence of a "*".

The equal-time quantum effective action constructed here, represents the information content of the quantum system for one instance in time. Only the knowledge at all evolution times is equivalent to the knowledge of the quantum effective action constructed from unequal-time correlation functions. It is important to note that if $\hat{\rho}_t$ depends on no other degrees of freedom than $\hat{\psi}$ and $\hat{\psi}^\dagger$, the knowledge of Γ_t or $\hat{\rho}_t$ is fully equivalent. Given the Hamiltonian $\hat{\mathcal{H}}$ of the system, the von-Neumann equation is then equivalent to an evolution equation for Γ_t, i.e.

$$i\partial_t\hat{\rho}_t = \left[\hat{\mathcal{H}},\hat{\rho}_t\right] \qquad \Leftrightarrow \qquad i\partial_t\Gamma_t = \mathcal{L}\Gamma_t \, . \tag{3.24}$$

Here $\mathcal{L}$ [87] is a functional-differential operator that depends on the form of $\hat{H}$. To obtain evolution equations for the equal-time 1PI correlators $\Gamma_t^{\alpha_1,\ldots,\alpha_n}(x_1,\ldots,x_n)$ one has to take functional derivatives of the evolution equation 3.24. This results in a infinite set of evolution equations, where the time evolution of the correlators at given order depends on higher order correlators. Usually one uses the term "hierarchy" for these specific type of set of equations[4].

Now, we present a way to obtain an explicit form of this evolution equation for the generating functional and with that an exact evolution equation for the particle number distribution. For this we have to assume a microscopic Hamiltonian to calculate $\mathcal{L}$. Motivated by experimental observation reported on in chapter 10, we consider a one-component non-relativistic Bose gas of particles with mass m and interaction strength g, described by

$$\hat{H} = \int_x \left[\frac{1}{2m}\left(\nabla_x\hat{\psi}_x^\dagger\right)\left(\nabla_x\hat{\psi}_x\right) + \frac{g}{2}\hat{\psi}_x^\dagger\hat{\psi}_x^\dagger\hat{\psi}_x\hat{\psi}_x\right] \, . \tag{3.25}$$

By calculating the corresponding Weyl symbol we derive $\mathcal{L}$. Together with Eq. (3.23) this translates into an evolution equation for the 1PI correlators. Assuming translation invariance, we define, in analogy to usually obtained kinetic equations [90], a *particle number distribution*

$$f(p) + \frac{1}{2} = \int_{x-y} \mathrm{e}^{-ip(x-y)}\frac{1}{2}\left\langle\left(\hat{\psi}_x^\dagger\hat{\psi}_y + \hat{\psi}_x\hat{\psi}_y^\dagger\right)\right\rangle_{\mathrm{conn}} \, . \tag{3.26}$$

---

[4] Here, we implicitly obtain a hierarchy which is a non-equilibrium, equal-time version of the Schwinger-Dyson equations.

This definition is equivalent to

$$f(p) + 1/2 = C_t^{\Psi^*\Psi}(p) \equiv \int_{x-y} \mathrm{e}^{-ip(x-y)} C_t^{\Psi^*\Psi}(x,y)\,, \tag{3.27}$$

where

$$C_t^{\Psi^*\Psi}(x,y) = \left(\Gamma_t^{\Psi^*\Psi}\right)^{-1}(x,y) \tag{3.28}$$

is the connected two-point correlator. In equilibrium, one refers to particles as well-defined, most of the time freely propagating objects. Considering for example quasi-particle excitations this is ambiguous far from equilibrium. Later, we observe the emergence of a conserved quantity corresponding to summed distribution functions which a posteriori justifies the concept of particles far from equilibrium.

Putting things together, the preceding definitions allow us to rewrite the evolution equation for the 1PI correlators into an evolution equation for the particle number distribution which takes a Boltzmann-type form

$$\partial_t f_p = C_p\left[f, \Gamma_t^{\Psi^*\Psi^*\Psi\Psi}\right]\,, \tag{3.29}$$

with the collision integral $C_p\left[f, \Gamma^{(4)}\right]$ explicitly depending on the two-point functions and the 4-vertices; it is given by

$$\begin{aligned}\partial_t C_t^{\Psi^*\Psi}(p) = g \int_{q,r,l} & i\left[\Gamma_t^{\Psi^*\Psi^*\Psi\Psi}(p,q,-r,-l) - \Gamma_t^{\Psi^*\Psi^*\Psi\Psi}(l,r,-q,-p)\right] \times \\ & \times C_t^{\Psi^*\Psi}(p) C_t^{\Psi^*\Psi}(q) C_t^{\Psi^*\Psi}(r) C_t^{\Psi^*\Psi}(l)\,.\end{aligned} \tag{3.30}$$

The evolution equation is formally exact and includes all quantum effects; it assumes only spatially translation invariant and $U(1)$ symmetric correlators. To make use of the equation the 4-vertices $\Gamma_{pqrl}^{\Psi\Psi\Psi^*\Psi^*}$ have to be determined. There exist, however, only approximate solutions for some limiting cases, e.g. thermal equilibrium [91].

3.5 Renormalization group

In physics one is often confronted with the question how macroscopic phenomena emerge from the underlying microscopic physics. Interestingly, new phenomena can emerge as in the macroscopic regime microscopic details are often washed out [9]. A well-known example is hydrodynamics of classical fluids - especially the phenomenon of turbulence. In terms of a theoretical description, it is a complicated problem as it involves details from large scales, where the system is driven, down to small scales, on which energy dissipation takes place due to viscosity.

The *renormalization group* of QFT gives a strategy for dealing with these problems which include many length scales. Instead of considering all length scales, one takes them into account separately, such that in a stepwise procedure a theory for each length scale emerges. In this description the parameters of the theory can become dependent on the length scale; that is the definition of a *running coupling*. For comparison between theory and experiment this also implies that measured parameters have to be given together with the scale, e.g. the energy, at which they are measured [80].

At so-called RG fixed points the theoretical descriptions get scale-invariant. An example for such fixed points are equilibrium phase transitions. It was suggested that non-thermal fixed points can be interpreted as fixed points of a generalized RG treatment. One already employed a non-equilibrium setting by formulating the known RG procedure on a Schwinger-Keldysh time path [92]. For obtaining a better theoretical understanding, this should be generalized taking time as a flow parameter into account [46, 93]. Being far from equilibrium permits new fixed point solutions compared to thermal equilibrium as the fluctuation-dissipation relation can be violated, which was already observed in numerical studies [94].

At this point, let us shortly comment on the idea behind the visualization of the non-thermal fixed point scenario in Fig. 2.1. At the current stage, it is a schematic drawing exactly taking up the idea of time being the flow parameter. Motivated by equilibrium RG flows, the lines with arrows show the flow in time and the fixed point is associated to the non-thermal fixed point. A visualization of the above mentioned flow in time has already been achieved in numerical simulation [95].

3.6 The O(N)-model

In the context of analytical predictions of quantum field theoretical models the so-called $O(N)$-model plays an important role as it allows for controlled expansions in orders of $1/N$, where N is the number of field components [84]. The Lagrangian L of the $O(N)$-model for a real scalar field Φ is given by

$$L = \frac{1}{2}\left[(\nabla\Phi)^2 - \mu^2\Phi^2\right] - \frac{1}{4!}\frac{\lambda}{N}\left(\Phi^2\right)^2, \tag{3.31}$$

with the mass μ and the interaction strength λ. The interaction term is explicitly N-dependent to ensure the right scaling of this term compared to the mass term in the limit $N \to \infty$. It is exactly this N-dependence which renders certain terms in a perturbative expansion zero in the limit of large N and allows for resummation of other terms.

The $O(N)$-model further allows for the prediction of scaling exponents for infrared fixed points for highly occupied systems. From a vertex-resummed kinetic theory one analytically finds $\beta = 1/2$ [68]. Further, particle number conservation in the infrared implies $\alpha = d\beta$ for the amplitude scaling exponent. Even a prediction for the scaling function in the power-law regime is possible and one finds $f_S \propto k^{-(d+1)}$. Compared to thermal equilibrium, the dimensionality d enters explicitly in the momentum distribution exponents out-of-equilibrium [92]. These predictions have been compared to numerical simulations employing different N [68, 90, 96, 97].

Chapter 4

Quantum simulation and computation

As already pointed out by Feynman [98], simulating quantum mechanics on a classical computer is hard, especially for many particles. He proposed the use of quantum systems themselves to simulate quantum mechanics. Here, the big advantage is that the simulating entity already features quantum mechanical properties [99].

In chapter 2 we introduced topical questions concerning many-body systems in and out of equilibrium. Not many general theoretical models for their descriptions are at hand. Thus, we introduced a general framework, quantum field theory, for tackling these questions. In experiments one can prepare interesting many-body states in a highly controlled fashion and characterization allows for testing these methods. This all fits in the context of quantum simulation and computation. To put the experimental efforts into context, we are going to introduce what we mean by quantum simulation and quantum computation.

For quantum simulation one distinguishes between digital and analog quantum simulation. The important ingredients for both are the ability to prepare an initial condition in a controlled fashion, the implementation of the desired time evolution and employing an appropriate read-out to extract the relevant information. In digital quantum simulation, schemes are used which are similar to the circuit model known from standard computations [100]. It has been shown that with one-bit and two-bit gates indeed a universal quantum simulator can be built [101].

The idea behind analog quantum simulation is to mimic or to emulate a system, for which control parameters are not easy to access, with a system where the degree of control is high. For this, one has to find a mapping between the Hamiltonian $\mathcal{H}_p$ of the system which should be simulated and the simulator's Hamiltonian $\mathcal{H}_{m_p}$ (see Fig. 4.1). One advantage of analog quantum simulation is the larger fault tolerance. Qualitative features and their dependence on certain parameters may even be studied if the dynamics which should be simulated is not implemented in all its details. This is for example the case when simulating superconductivity with ultracold atoms in optical lattices [102].

In [103], Horsman et al. give a detailed definition to discriminate between quantum simulation and quantum (or physical) computation. For our purposes, Fig. 4.1 summarizes the definitions in a diagrammatic way and here, we shortly introduce the

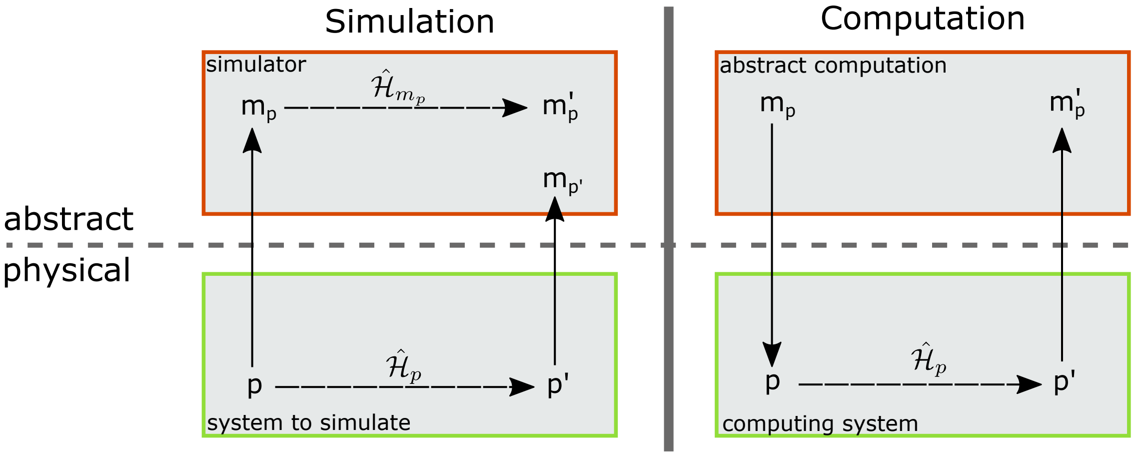

Figure 4.1: **Simulation and computation.** For the definition of simulation and computation we distinguish between the physical and the abstract system. In the case of a simulation the initial state p in the system which should be simulated is mapped onto an initial state m_p. The time evolution is implemented in the simulator to achieve m'_p. A simulation is verified by m'_p and $m_{p'}$, where $m_{p'}$ is the result from the true dynamics in the physical system mapped onto a state of the simulator, being approximately the same. In the case of a computation the controlled system plays the role of the physical system. An abstract computation has to be mapped onto the physical system. The computation is implemented by the appropriate time evolution in the physical system and the result is mapped back to the abstract level on which the computation is formulated. Figure adapted from [103].

definition step-by-step. As shown in Fig. 4.1, the first step is to distinguish between the physical and the abstract system.

In the presented definition of a simulation, the system offering a high degree of control takes the role of the abstract system in which the simulation takes place. The abstract system can, in principle, also be a classical computer or an analytical calculation. One has to find a mapping that maps the initial state p in the system which should be simulated onto an initial state m_p in the abstract system. The time evolution is implemented in the simulator with the Hamiltonian $\hat{\mathcal{H}}_{m_p}$ to achieve m'_p, where $\hat{\mathcal{H}}_{m_p}$ has to be chosen such that the relevant physics of $\hat{\mathcal{H}}_p$ is captured. For verification, we have to give a criterion for a simulation being good. This is achieved by mapping the result in the physical system p' into the abstract system onto $m_{p'}$. For practical reasons we call a simulation sufficiently good if $|m'_p - m_{p'}| < \epsilon$; the two results have to be compared by an appropriate distance measure which depends on the details of systems. Verifying the simulation is a necessary condition for performing the next step: a physical computation.

For a physical computation, the controlled system, which has prior performed the simulation, takes the role of the physical system. It is important to note that in the previous case the initial state p was a physical state whereas now it is an abstract object which initiates the calculation. As a first step, this abstract object of the computation has to be mapped onto the physical system. For this encoding step, exact knowledge about the physical system is necessary and it is the encoding which determines how the computation is implemented by an appropriate time evolution in the physical system. To obtain the result of the calculation, the state in the computing system p' is mapped back to the abstract level on which the computation is formulated. This represents the decoding step which in principle does not need to be the encoding reversed. With that the physical state is mapped back to an abstract object – the final result of the calculation.

On the basis of the definition given in Fig. 4.1, we can put our experimental observations into context. The observation of universal dynamics reported on in chapter 8 is identified as a quantum simulation of dynamics far from equilibrium in systems as different as the one-component Bose gas [68] and the quark-gluon-plasma [104]. The simulation process in that case can be verified by the measurement of the universal exponents. This verification allows us to interpret the extraction of the quantum effective action in chapter 10 as a physical computation. The final mapping onto the result m_p' is achieved by the extraction of the 1PI correlation functions.

In summary, quantum simulations and computations are based on using quantum systems such that all relevant features unique to quantum mechanics are incorporated. In combination with an efficient readout and the controllability offered by ultracold atomic systems, this allows us to study different phenomena far from equilibrium experimentally. In particular, qualitative as well as quantitative tests of the presented quantum field theoretical methods become possible.

Part II

Experimental tools

Chapter 5

Experimental platform

In this chapter we present details of the experimental platform used in this thesis. First, we give a brief overview of the experimental apparatus and describe the cycle leading to the production of Bose-Einstein condensates. We detail the trapping potentials used and connect the internal states of ^{87}Rb to the microscopic spin-1 Hamiltonian. This introduces the relevant internal and external degrees of freedom whose interplay we will study experimentally. In addition to the experimental control of the dynamics, the readout of the final quantum state is an equally important aspect of quantum simulation and computation. Hence we present the employed readout schemes. Finally, we discuss the experimental challenges resulting from the long evolution times studied here.

5.1 Physical system

5.1.1 Producing a BEC

Nowadays the routine for producing BECs is standard in many laboratories around the world. Here, we provide only a brief outline of the experimental sequence. A detailed descriptions of the whole experimental apparatus can be found in [105–108].

In our experiments we use ^{87}Rb which features two hyperfine manifolds $F = 1, 2$ in its electronic ground state [109]. These offer a large playground for studying spinor physics with ferromagnetic as well as antiferromagnetic interactions [110]. The BEC is generated in an ultra-high vacuum glass cell giving large optical access for manipulation and trapping (see Fig. 5.1a). We start with a three-dimensional magneto optical trap (MOT) which loads atoms from a transversely cold atomic beam generated from a two-dimensional MOT. After a short cycle of sub-Doppler cooling we transfer the atoms to a magnetic time-orbiting potential (TOP) trap [111], where we force evaporative cooling by lowering the amplitude of the magnetic bias field. Not yet condensed, the atoms are loaded in a dipole trap consisting of two crossed red-detuned laser beams generated from a Yb:YAG laser (1030 nm). By lowering the laser power we perform a last step of evaporative cooling, producing a BEC with $\sim 10^4$ atoms and negligible thermal fraction. This routine takes $\sim 36\,\text{s}$ and sets the lower bound on the experimental cycle time. After the desired evolution

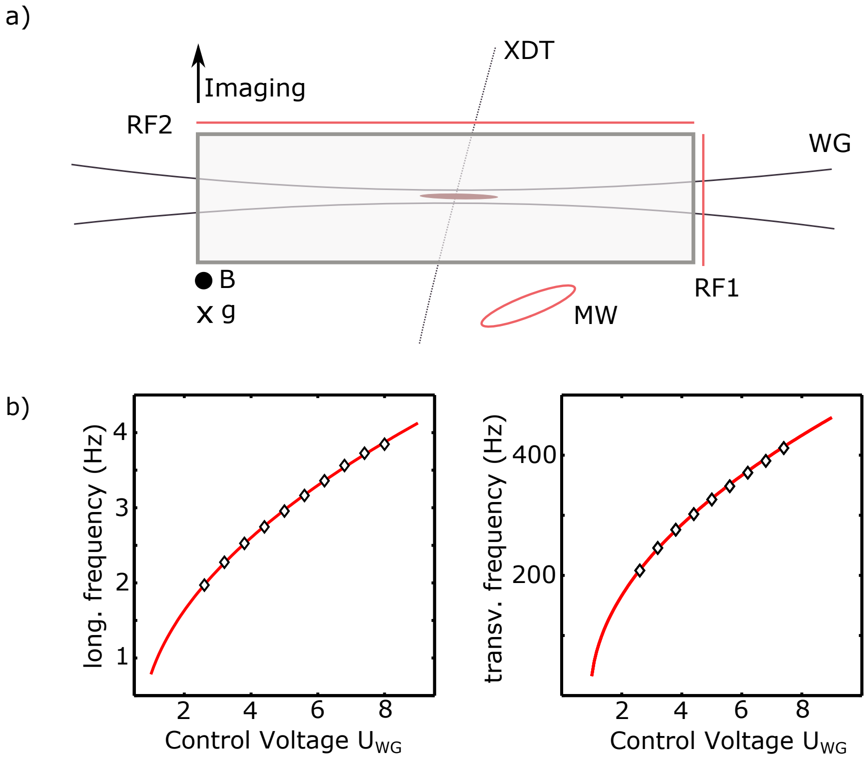

Figure 5.1: **Arrangement of optical traps and trapping frequencies.** a) The BEC is generated in an ultra-high vacuum glass cell. The atoms are loaded from the magnetic trap into a crossed dipole trap consisting of the XDT beam and WG beam. For the experiments the XDT beam is switched off adiabatically and the BEC (red cloud) expands in the WG trap giving a quasi-one-dimensional trapping potential. We apply a homogeneous magnetic offset field **B** pointing in z-direction, whereas gravity g points in $-z$-direction. The coils (red) are used for control of the internal states by applying microwave (mw) and radio-frequency (RF1 and RF2) magnetic fields. b) Experimentally measured longitudinal and transversal trapping frequencies in the WG as a function of the control voltage U_{WG}. The fit (red line) is a square root fit to the experimental data.

time we employ state-selective absorption imaging [108] of all eight levels in the two hyperfine manifolds.

5.1.2 Quasi one-dimensional trap

The experiments described within this thesis are carried out in a quasi-one-dimensional optical dipole trap (see also [107, 112] for details). After condensation, one beam of the crossed dipole trap (XDT) is adiabatically switched off; we are left with one single dipole beam, called waveguide (WG), with a trapping frequency ratio of the longitudinal and transversal directions of ~ 100. The absolute values of the trapping frequencies can be tuned by changing the power of the laser beam which is controlled by the set point voltage U_{WG} of a control loop PID. In Fig. 5.1 the experimentally measured longitudinal $\omega_{\|}/2\pi$ and the transversal $\omega_{\perp}/2\pi$ trapping

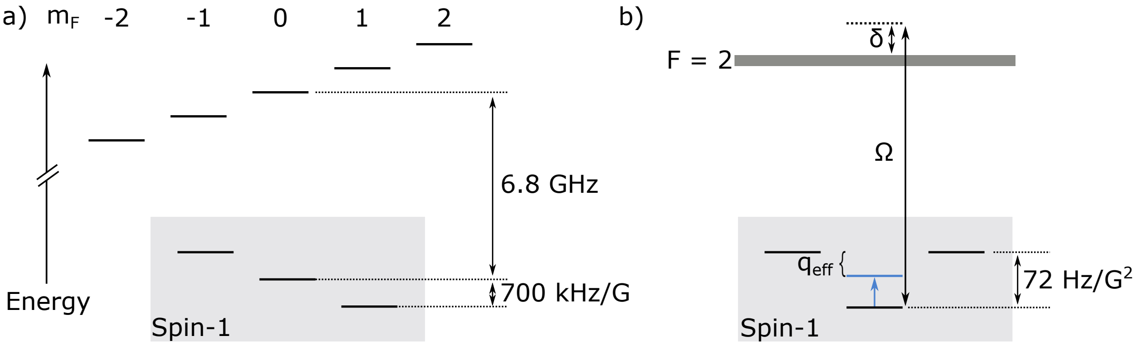

Figure 5.2: **Electronic ground state structure.** a) Hyperfine manifolds in the electronic ground state of ^{87}Rb. The $F = 1$ hyperfine manifold is used as a spin-1 system (grey box). The linear Zeeman effect splits the magnetic sublevels by $\sim 700\,\mathrm{kHz/G}$. b) In the rotating frame of the linear Zeeman effect one is left with the second-order Zeeman effect shifting the $m_F = 0$ level by $72\,\mathrm{Hz/G}^2$. This energy shift is tuned by applying off-resonant microwave dressing with Rabi frequency Ω and detuning δ to $(F, m_F) = (2, 0)$ leading to an effective energy shift q_{eff}, the experimental control parameter for employing the quenches.

frequencies are shown as function of the control voltage. The fit (red line) reveals the expected square-root behaviour of the trapping frequency as a function of the laser power which is proportional to the voltage U_{WG}. A change of the longitudinal trapping frequency also shifts the position of the trap centre as the beam is slightly tilted against gravity. The harmonic oscillator length $a_\perp = \sqrt{\hbar/(m\omega_\perp)}$ in the radial direction for all employed laser powers is on the order of the density healing length [113] and smaller than the typical size of spin excitations. This leads to dynamics predominantly in the longitudinal direction and allows for imaging of the atomic densities spatially resolved without averaging possible structures in the radial direction.

Due to the harmonic confinement, the atomic densities are inhomogeneous. The spin-spin interaction is density-dependent and thus the inhomogeneous density leads to spatially dependent interaction parameters which is in principle disadvantageous. In the post-analysis, we use the central $\sim 200\,\mu$m of the cloud, where the density only changes by approximately 10%. This corresponds to ~ 40 times the size of a typical spin excitation, giving access to a system which is large enough to observe long time dynamics with minimal finite size effects.

5.2 Physical implementation of a spin-1

In this section we describe how a spin-1 is realized using ^{87}Rb atoms and how we control the dynamics.

In its electronic ground state ^{87}Rb has two hyperfine manifolds with quantum numbers $F = 1, 2$ (see Fig. 5.2a). The results in this thesis are carried out in the $F = 1$ hyperfine manifold giving access to a "real" spin-1; "real" is meant in distinction to pseudo-spin systems [107, 114] and effective spin-1 systems [115] which

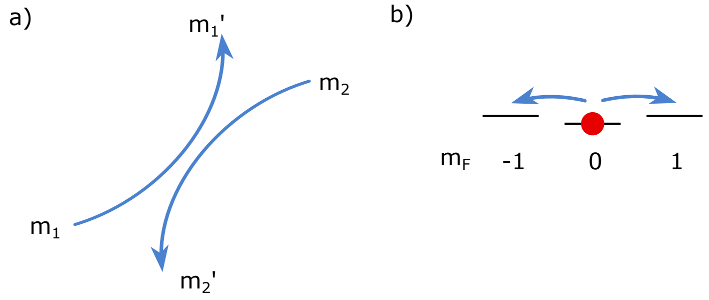

Figure 5.3: **Spin-changing collisions.** a) Two atoms in the magnetic sub states m_1 and m_2 collide and produce two atoms in the states m_1' and m_2'. Within the approximations described in the main text the total angular momentum $\sum_{i=1,2} m_i$ is conserved. b) Spin-changing collisions allow for redistribution of populations among the different sub states

for example can be employed by using the $F = 2$ manifold. The two hyperfine manifolds are energetically split by $\sim 6.8\,\mathrm{GHz}$ and by applying microwave (mw) radiation we are able to transfer populations between the manifolds coherently. This gives full controllability over the initial populations of the different levels and allows for splitting populations.

Throughout the thesis we will use a shorthand notation for the sublevels: (F, m_F). The g-factors of $F = 1$ and $F = 2$ are nearly the same in magnitude, however, the sign is different [109]. This is important for the hyperfine selective radiofrequency (rf) rotations employed later. In Fig. 5.2a all eight energy levels are shown, where the magnetic sublevels are energetically shifted due to the linear Zeeman effect in a magnetic field B by $p = 700\,\mathrm{kHz/G} \times B$. This energy shift leads to a rotation of the spin around the z-axis with the Larmor frequency $\omega_\mathrm{L} = 2\pi \times p$.

Intuitive picture of the interaction processes

Before further describing the effects of energy shifts induced by the magnetic field we give an intuitive picture for the possible interaction processes.

In a BEC the collisions, even in the many-body limit, can be described by two-body quantum scattering because of the diluteness of the gas [110]. We assume that the particles only interact via s-wave scattering as described by the cold-collision approximation. Further, we make use of the "spinor-gas" collision approximation, i.e. we assume that the short-range potential is rotationally invariant and guarantees the conservation of the total angular momentum of the colliding pair. Neglecting dipolar relaxation we only have to take care about the internal angular momentum. In practice this leads to a conservation of $m_1 + m_2$ where m_j is the magnetic sub state of the particle j (see Fig. 5.3a). A more detailed discussion of the approximations is found in [110, 116].

The simplest interaction is the case of $m_j = m_j'$, i.e. no change of the magnetic sub states. The three levels also give rise to spin-changing collisions (SCC). For example, Fig. 5.3b shows the interaction of two atoms with $m_1 = m_2 = 0$ leading to $m_1' = +1$ and $m_2' = -1$. This allows for redistribution among the different states with conserved imbalance of the side modes, where we refer to the $m_F = \pm 1$ states as side modes. This process is similar to parametric down-conversion in optics and in principle produces highly entangled states [117].

Effects of magnetic field shift

Having the process of spin-changing collision in mind, it is apparent that the linear Zeeman effect only affects the dynamics for finite F_z magnetization (not employed here) or magnetic field gradients. Thus, we give a description of the dynamics in the rotating frame of the Larmor frequency. The resulting level scheme is shown in Fig. 5.2b, where $(1, 0)$ is energetically shifted with respect to $(1, \pm 1)$ by $q_B = 72\,\mathrm{kHz}/\mathrm{G}^2 \times B^2$.

This detuning prohibits spin-changing collision dynamics at the magnetic fields employed in our experiments ($B = 0.884\,\mathrm{G}$) as the interaction strength is on the order of 2 Hz. A convenient way for tuning q is so-called microwave dressing [118]. Applying off-resonant mw fields with Rabi frequency Ω and detuning δ leads to an effective detuning $q_{\text{eff}} = q_B + \Omega^2/4\delta$. Thus, we use it as the experimental control parameter for initiating dynamics. Infinitely fast quenches (on the order of all relevant energy scales) are conveniently implemented by switching on or changing the detuning of the mw fields.

In the following we will use the notation of q_{eff} for the experimentally adjusted value of the dressing. It is calculated using only the coupling of the microwave to the $(1, 0) \rightarrow (2, 0)$ transition. Couplings of other levels and effects due to the effective trapping potentials are not taken into account and potentially lead to a shift of the absolute values. Therefore we always adjust q_{eff} relative to a spectroscopy measurement described later. For distinction, we will hereafter refer to the theoretical value of the detuning simply as q.

5.3 Theoretical basis for describing spin-1 systems

In this section we first introduce some notations concerning spin-1 algebras which are necessary for introducing the Hamiltonian. We discuss the order of magnitude of the experimentally relevant parameters for the situation employed and its implications for the stability of the setup. This section is based on [110, 116].

5.3.1 Spin operators

On the microscopic level we need three bosonic field operators for describing the physical processes. These are labelled by the magnetic quantum numbers $m \in (0, \pm 1)$, where $\hat{\psi}_m^{(\dagger)}(\vec{r})$ annihilates (generates) an excitation in the magnetic sub state m at position $\vec{r}$. They satisfy the commutation relation

$$[\hat{\psi}_m(\vec{r}), \hat{\psi}^\dagger_{m'}(\vec{r'})] = \delta_{mm'}\delta(\vec{r} - \vec{r'})\,, \tag{5.1}$$

$$[\hat{\psi}_m(\vec{r}), \hat{\psi}_{m'}(\vec{r'})] = [\hat{\psi}^\dagger_m(\vec{r}), \hat{\psi}^\dagger_{m'}(\vec{r'})] = 0\,, \tag{5.2}$$

with $\delta_{mm'}$ being the Kronecker delta. The bosonic fields, in our case, describe the three magnetic sublevels $m = 0, \pm 1$ of the $F = 1$ hyperfine manifold of ^{87}Rb.

The interaction Hamiltonian is conveniently formulated in the language of spins. The group of all spin-1 operators has eight generators of which we, for simplicity, only introduce the three spin operators $\hat{F}_x$, $\hat{F}_y$ and $\hat{F}_z$. They can be written as $\hat{F}_i = \hat{\psi}^\dagger f_i \hat{\psi}$ with $\hat{\psi} = (\hat{\psi}_{+1}, \hat{\psi}_0, \hat{\psi}_{-1})^\mathrm{T}$ and the spin matrices f_i $(i = x, y, z)$

$$f_x = \frac{1}{\sqrt{2}} \begin{pmatrix} 0 & 1 & 0 \\ 1 & 0 & 1 \\ 0 & 1 & 0 \end{pmatrix}, \quad f_y = \frac{\mathrm{i}}{\sqrt{2}} \begin{pmatrix} 0 & 1 & 0 \\ -1 & 0 & 1 \\ 0 & -1 & 0 \end{pmatrix}, \quad f_z = \begin{pmatrix} 1 & 0 & 0 \\ 0 & 0 & 0 \\ 0 & 0 & -1 \end{pmatrix}. \tag{5.3}$$

With this we find

$$\hat{F}_x = \frac{1}{\sqrt{2}} \left(\hat{\psi}^\dagger_{+1} \hat{\psi}_0 + \hat{\psi}^\dagger_{-1} \hat{\psi}_0 \right) + \text{h.c.}, \tag{5.4}$$

$$\hat{F}_y = \frac{i}{\sqrt{2}} \left(\hat{\psi}^\dagger_{+1} \hat{\psi}_0 - \hat{\psi}^\dagger_{-1} \hat{\psi}_0 \right) + \text{h.c.}, \tag{5.5}$$

$$\hat{F}_z = \hat{\psi}^\dagger_{+1} \hat{\psi}_{+1} - \hat{\psi}^\dagger_{-1} \hat{\psi}_{-1}, \tag{5.6}$$

where h.c. is the Hermitian conjugate. Spin-changing collisions lead to dynamics predominantly in the transversal spin plane and thus we introduce the transversal spin

$$\hat{F}_\perp = \hat{F}_x + i\hat{F}_y = \sqrt{2} \left(\hat{\psi}^\dagger_0 \hat{\psi}_{+1} + \hat{\psi}^\dagger_{-1} \hat{\psi}_0 \right), \tag{5.7}$$

which we will identify as the emergent relevant degree of freedom.

5.3.2 Microscopic Hamiltonian

The microscopic Hamiltonian is build up out of a non-interacting and an interacting part. The non-interacting part includes a kinetic term and the trapping potential. In a magnetic field, it additionally contains the linear and the quadratic Zeeman effect. As discussed, for the description of the dynamics we will work in a rotating frame of the linear Zeeman effect and we can combine the term of quadratic shift with the microwave dressing by introducing the control parameter q. With this the *non-interacting part* reads

$$\hat{\mathcal{H}}_0/h = \int \mathrm{d}\vec{r}\; \hat{\psi}^\dagger \left[-\frac{\hbar \nabla^2}{4\pi m} + V_\text{ext} + q f_z^2 \right] \hat{\psi}, \tag{5.8}$$

where m is the atomic mass and V_ext is the external trapping potential. The *interacting part* consists of all terms obeying the described symmetries. With the assumptions from section 5.2 it can be written as

$$\hat{\mathcal{H}}_\text{int}/h = \frac{1}{2} \int \mathrm{d}\vec{r} \left[c_0 : \hat{n}^2(\vec{r}) : + c_1 : \hat{\vec{F}}^2(\vec{r}) : \right], \tag{5.9}$$

with $\hat{n} = \sum_{i=0,\pm1} \hat{n}_i = \sum_{i=0,\pm1} \hat{\psi}^\dagger_i \hat{\psi}_i$ and $\hat{\vec{F}} = \left(\hat{F}_x, \hat{F}_y, \hat{F}_z \right)^T$. The interaction constants c_0 and c_1 are given by

$$c_0 = \frac{g_0 + 2g_2}{3h}, \qquad c_1 = \frac{g_2 - g_0}{3h} \tag{5.10}$$

and can be related to the scattering lengths $a_{\mathcal{F}}$ of the two scattering channels $\mathcal{F} = 0, 2$ by $g_{\mathcal{F}} = \frac{4\pi\hbar^2}{m} a_{\mathcal{F}}$ [110].

The microscopic Hamiltonian under the given assumption and neglecting dipole-dipole interactions is then written as

$$\hat{\mathcal{H}} = \hat{\mathcal{H}}_0 + \hat{\mathcal{H}}_{\text{int}}. \tag{5.11}$$

Let us shortly discuss the different energy scales of the Hamiltonian. With the scattering lengths [110] we find that $c_0 \simeq 200 c_1$, i.e. the time scale associated with density-density interactions is 200 times larger than the spin-spin interactions. The dynamics leads to a highly excited spin degree of freedom whereas density excitations are suppressed. We find that the typical energy scale of spin-dependent interactions for the atom numbers employed is $nc_1 \simeq 2\,\text{Hz}$, where n is the total atom number density.

5.4 Typical experimental sequence

Generally one can separate a quantum simulation into different tasks the experimentalist has to accomplish. Usually it consists of three main steps:

1. Preparation of the initial condition
2. Evolving the system under a certain Hamiltonian
3. Readout of the final state

In this section we shortly detail the experimental sequence.

Preparation of the initial condition

In the magnetic trap all high field seeking states are repelled. We do not additionally pump the atoms into $F = 2$ and thus the BEC is initially created in the state $(1, -1)$. For preparing the polar state, i.e. all atoms in the state $(1, 0)$, we use the microwave coil (cf. Fig. 5.1) to couple two levels in different hyperfine manifolds. The coupling is described by the Hamiltonian

$$\hat{\mathcal{H}}_{\text{mw}}/h = \frac{1}{\pi\sqrt{8}} \Omega_{\text{mw}} \left(\psi^\dagger_{1,m_1} \psi_{2,m_2} + \text{h.c.} \right) , \tag{5.12}$$

where $\psi^\dagger_{F,m_F}$ is the field creation operator of the hyperfine state (F, m_F). $\hat{\mathcal{H}}_{\text{mw}}$ is the generator of rotations $\exp\left(-i\hat{\mathcal{H}}_{\text{mw}} t\right)$ of the corresponding two level system. We use a π-pulse, i.e. a pulse with length t such that $\Omega_{\text{mw}} t = \pi$, to transfer the atoms from the state (1,-1) to (2,0) and a second pulse to transfer the atoms from (2,0) to (1,0).

After the pulses, a strong magnetic field gradient is applied to repel residual atoms in the side modes $(1, \pm 1)$ from the trap. After this we wait for 100 ms to allow the magnetic field to stabilize to its set value.

Quench

Following the preparation we initiate the dynamics by employing an instantaneous quench of the detuning q_{eff} by switching on the microwave dressing. We let the system evolve under the Hamiltonian 5.11 for the desired evolution time t_{evo}.

Readout

After the evolution time we readout the state by destructive absorption imaging. For the readout of transversal spin components we use radio-frequency fields applied with the rf-coils RF1 and RF2 (cf. Fig. 5.1). The rotations are described by the Hamiltonian

$$\hat{\mathcal{H}}_{\text{RF}} = \frac{\Omega_{\text{RF}}}{2\pi}\left[\cos\left(\phi_{\text{RF}}\right)\hat{F}_x + \sin\left(\phi_{\text{RF}}\right)\hat{F}_y\right], \tag{5.13}$$

where ϕ_{RF} is the phase of the rf field and can be adjusted using an arbitrary waveform generator. Tuning the rf-fields of the two coils $\sim 90°$ out of phase we employ hyperfine-state selective rf rotations [119].

5.5 Probing the dynamics of a spinor BEC

The many degrees of freedom inherent to the spin-1 Bose gas make it challenging to keep track of the dynamical processes. In this section we describe the different schemes used in this thesis to probe these different degrees of freedom. All imaging techniques are based on spatially resolved absorption imaging. We further employ spin rotations and splitting mw pulses to simultaneously access different directions of the spin degree of freedom.

5.5.1 Spatially resolved absorption imaging

In our experiments we employ high intensity absorption imaging [120] with a spatial resolution of $\sim 1.1\,\mu$m [114]. We use two $15\,\mu$s light pulses resonant on the $F = 2 \rightarrow F' = 3$ transition of the D_2 line. The first pulse images the $F = 2$ population, whereas the second pulse, accompanied by repumper light, images the $F = 1$ populations. We use a short time of flight of $\sim 1\,$ms to reduce the densities and achieve state-selectivity by applying a Stern-Gerlach magnetic field gradient in z-direction, parallel to the magnetic field, while switching off the waveguide to separate the different hyperfine states spatially. After the two imaging pulses we record empty reference pictures to determine the light intensity without any atoms.

5.5.2 Accessing the spin degree of freedom

The described imaging sequence allows us to measure the populations of all eight hyperfine states. This directly gives access to the spin in z-direction at position y with

$$F_z(y) \equiv \langle \hat{F}_z(y) \rangle_{y,y+\Delta y} = \frac{N_{+1}(y) - N_{-1}(y)}{N_{\text{tot}}(y)} \tag{5.14}$$

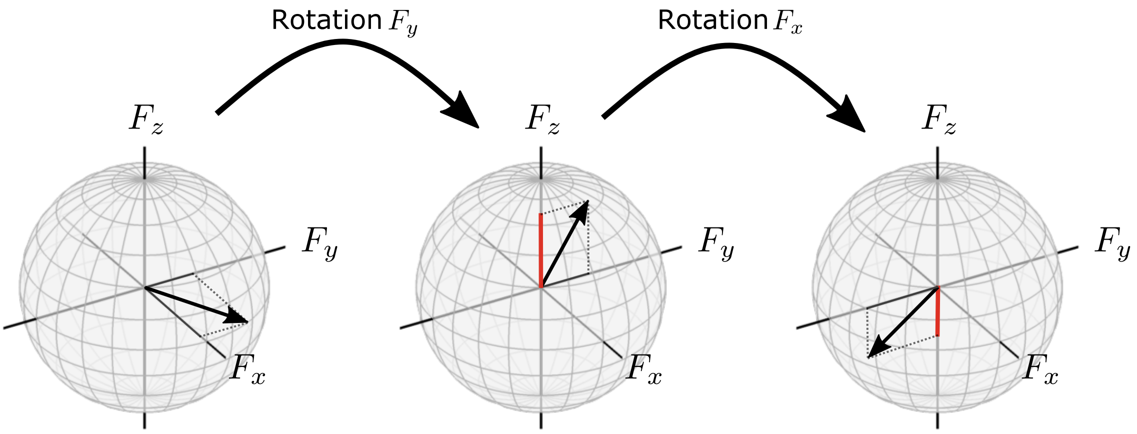

Figure 5.4: **Visualization of rf rotations on spin sphere.** By changing the phase of the rf field we employ rotations around different axes on the spin sphere (see the Hamiltonian in Eq. (5.13)). The Stern-Gerlach splitting gives access to the F_z-component of the spin. With $\pi/2$ rf rotations we map the different transversal spin projections (red) onto the z-axis.

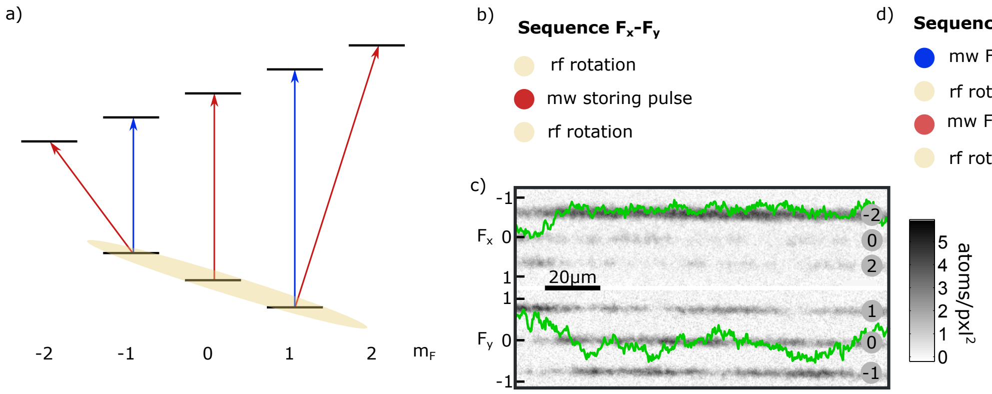

Figure 5.5: **Imaging sequence and typical picture.** a) Level scheme of $F = 1$ and $F = 2$ hyperfine manifold. The blue and red arrows indicate the employed microwave pulses for storing the F_z and the F_x projection of the spin, respectively. To extract information about additional observables we employ hyperfine selective $\pi/2$ spin rotations in the $F = 1$ manifold. b) Sequence for measuring the complex valued field $F_\perp(y)$. c) Sample image acquired after 18 s evolution time with the readout b). The atomic densities of the hyperfine states are indicated by the grey shading. Green lines show the inferred spin projections F_x and F_y. d) Sequence for the full spin readout.

Here $N_{\pm1}(y)$ is the atom number in state $m_F = \pm 1$ and $N_{\text{tot}}(y)$ is the total atom number. The bracket $\langle\cdot\rangle_{y,y+\Delta y}$ indicates that the single realization measurement result at position y is already the average over the number of atoms in the given interval $[y, y + \Delta y]$, where Δy is the pixel size. From now on we use the notation $F_i(y)$ for the single realization result and the used pixel size is indicated only when necessary.

The transversal spin $F_\perp$ is connected to coherences, i.e. densities and relative phases of the magnetic sub states. We access the coherences by coupling the three levels with rf magnetic fields resonant to the energy splitting of the linear Zeeman effect. This effectively employs rotations in spin space around for example the x-axis; relative phases of the rf fields for two coupling pulses lead to different rotation axes. The rotations are visualized in Fig. 5.4.

Imaging one projection

First, we present the simplest readout for imaging just one transversal spin direction, which we will call F_x. For this we apply after the desired evolution time a resonant $\pi/2$ rf-pulse to rotate one transversal spin projection onto the z-axis (first two panels of Fig. 5.4). The direction of the readout pulse either defines the x-direction (when starting from the polar) or is randomized already after "short" evolution times ($> 100\,\text{ms}$) due to magnetic field fluctuations. Therefore we image a different projection in each experimental realization; this does not hamper a detection as we assume the system/dynamics to be invariant under a rotation around the z-axis. We calculate the x-projection from the atomic densities $N_i^{F=1}$ measured after the rotation by

$$F_x(y) = \frac{N_{+1}^{F=1}(y) - N_{-1}^{F=1}(y)}{N_{\text{tot}}^{F=1}(y)} \,. \tag{5.15}$$

Imaging the complex valued transversal spin

During this thesis we developed a new readout technique which is capable of detecting simultaneously multiple (even non-commuting) spin observables. Here we present the pulse sequences employed and how the observables are obtained from the measured densities. Details about the theoretical background, the connection to POVM's, the limits of the scheme and the experimental details can be found in [119] and the PhD thesis of Philipp Kunkel [121].

Building on the scheme already presented, we have to implement another rf rotation to obtain a second, orthogonal, spin direction. We first split the populations of the $F = 1$ hyperfine manifold with three $\pi/2$ mw-pulses and store the result obtained for F_x in $F = 2$. A second $\pi/2$ rf rotation around the x-axis maps the y-projection of the transversal spin on the z-direction in $F = 1$ (third panel of Fig. 5.4). We use a hyperfine selective rf rotation to not disturb the populations stored in $F = 2$. This is implemented by using two rf-coils $\sim 90°$ out of phase which produce a rotating magnetic field coupling only to the $F = 1$. The rotation in $F = 2$ is off-resonant because of the different signs of the g-factors. We read out the two

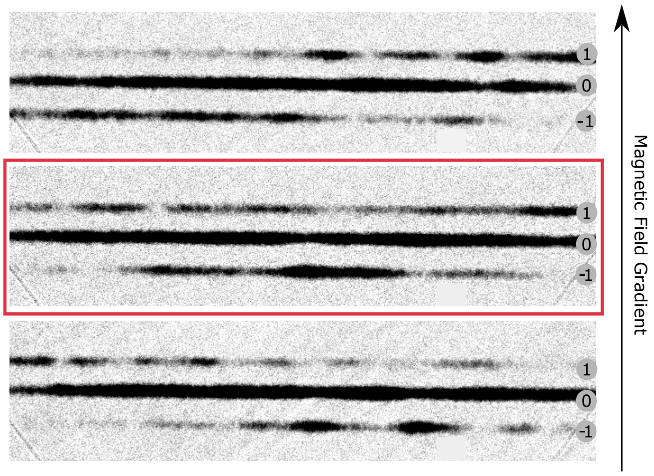

Figure 5.6: **Compensation of magnetic field gradient.** For compensating the magnetic field gradient we observe the density in the three hyperfine states after 4 s evolution time in the regime of $q \approx 1.5|nc_1|$. We optimize for the minimal asymmetry of the ± 1 components. The red box marks the compensated setting.

spin projections with

$$F_x(y) = \frac{N_{+2}^{F=2}(y) - N_{-2}^{F=2}(y)}{N_{\text{tot}}^{F=2}(y)} \tag{5.16}$$

$$F_y(y) = \frac{N_{+1}^{F=1}(y) - N_{-1}^{F=1}(y)}{N_{\text{tot}}^{F=1}(y)} \,. \tag{5.17}$$

We obtain a spatially resolved snapshot of the complex-valued field

$$F_\perp(y) = F_x(y) + iF_y(y)$$

.

Full spin readout

As a last step we add again the F_z-projection to obtain a full readout of the spin-degree of freedom. This is achieved by storing the F_z projection in the states $(2, \pm 1)$ by two variable mw-pulses coupling $(1, \pm 1) \leftarrow (2, \pm 2)$ prior to the first rf pulse. For a pulse covering an angle of ϕ_{rot} the three projections are obtained with

$$F_x(y) = \frac{1}{\cos(\phi_{\text{rot}}/2)} \frac{N_{+2}^{F=2}(y) - N_{-2}^{F=2}(y)}{N_{\text{corr}}^{F=2}(y)} \,, \tag{5.18}$$

$$F_y(y) = \frac{1}{\cos(\phi_{\text{rot}}/2)} \frac{N_{+1}^{F=1}(y) - N_{-1}^{F=1}(y)}{N_{\text{corr}}^{F=1}(y)} \,, \tag{5.19}$$

$$F_z(y) = \frac{1}{\sin^2(\phi_{\text{rot}}/2)} \frac{N_{+1}^{F=2}(y) - N_{-1}^{F=2}(y)}{N_{\text{corr}}^{F=2}(y)} \,, \tag{5.20}$$

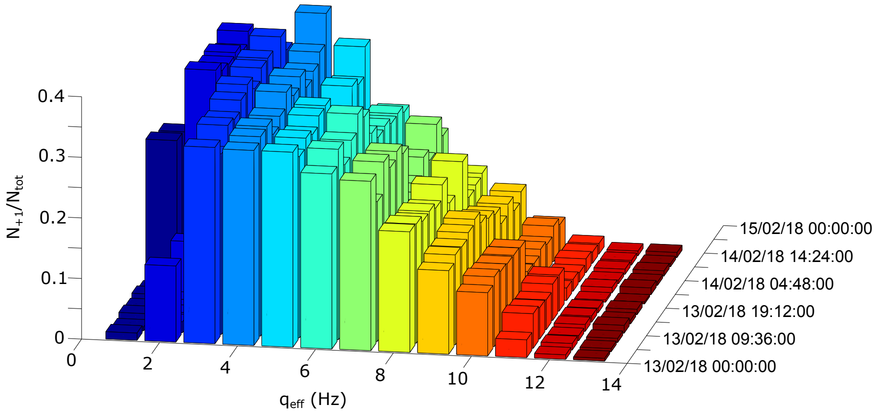

Figure 5.7: **Stability of SCC spectroscopy.** Spin changing collisions control measurement over the course of two days. The summed fractional population N_{+1}/N_{tot} is plotted as a function of q_{eff}.

with the corrected total atom numbers

$$N_{\text{corr}}^{F=2}(y) = N_{+2}^{F=2}(y) + N_{-2}^{F=2}(y) + N_{0}^{F=2}(y) + \frac{1}{2}\left(N_{+1}^{F=2}(y) + N_{-1}^{F=2}(y)\right) , \quad (5.21)$$

$$N_{\text{corr}}^{F=1}(y) = N_{+1}^{F=1}(y) + N_{-1}^{F=1}(y) + N_{0}^{F=1}(y) + \frac{1}{2}\left(N_{+1}^{F=2}(y) + N_{-1}^{F=2}(y)\right) . \quad (5.22)$$

We implement this imaging with $\phi_{\text{rot}} = \pi/3$.

5.6 Long-time stabilization

The slow dynamics resulting from the spin-spin interaction makes it necessary to employ long evolution times $> 2\,$s to observe dynamics beyond initial instabilities. Thus, for gathering enough experimental realizations, to achieve statistically significant results, a long time ($\sim$ two weeks) stability is important. All these time scales are experimentally challenging and require active stabilizations and control measurements for compensating drifts on different time scales (hours to days).

First, we actively stabilize the magnetic field in the experimental chamber by a magnetic flux gate to achieve magnetic field fluctuations below 0.1 mG [122]. Magnetic field gradients along the z-direction are compensated by applying a constant current to the rf-coil RF1. For this, we minimize the asymmetry of the demixing of the $(1, \pm 1)$ states after 4 s evolution time (see Fig. 5.6). After setting the experimental parameters this measurement is repeated every $\sim 5\,$h to ensure stability. The room temperature of the laboratory is stabilized to $\sim 0.1°$C.

Further, the microwave power of the employed microwave dressing is stabilized by a feed-back mechanism. We measure the Rabi frequency of the microwave dressing implicitly by employing a spectroscopic measurement of the spin-changing collisions every $\sim 5\,$h. We ensure the stability of the microwave dressing by observing the right edge of a spectroscopic measurement which is detailed in the next chapter. Fig. 5.7 shows this measurement over the course of two days. If the spectroscopic measurement changes, we adjust the value of q_{eff} accordingly.

Part III

Experimental results

Chapter 6

Probing the phase diagram

We motivated in chapter 2 that quantum quenches are an efficient way for driving systems far out of equilibrium. For employing those quenches, knowledge of the phase diagram of the underlying system is essential as it allows anticipating the relevant degrees of freedom and adjusting the corresponding parameters. Here, we discuss the mean-field phase diagram for a homogenous system and show the ground states of the Hamiltonian in this limit. To probe the phase diagram of the spin-1 system experimentally, we prepare the polar state, i.e. all atoms in (1,0), for a large positive detuning and quench the detuning q_{eff} to different values by rapidly switching on the microwave dressing. We let the system evolve for long evolution times (15 s) and probe the result by employing the full spin readout. Finally, we compare to the experimental results; the found degrees of freedom fit in the different regimes for long evolution times to the ground state predictions.

6.1 Mean-field predictions

For obtaining a mean-field picture (see [116] for details) we expand the field operators

$$\hat{\psi}_m(\vec{r}) = \sum_i \hat{a}_{mi}\varphi_{mi}(\vec{r})\,, \tag{6.1}$$

where ϕ_{mi} are basis functions of the spatial mode i of the magnetic quantum number m and $\hat{a}_{mi}$ are the associated annihilation operators. As we are dealing with a homogeneous condensate we assume that all atoms occupy the spatial mode $i = 0$. We define a normalized spinor ξ_m as $\psi_m = \sqrt{N}\xi_m$ and a normalized spin density $\vec{f} = \sum_{mm'} \xi^*_m f_{mm'} \xi_{m'}$. Inserting this in the microscopic Hamiltonian we find the mean-field energy functional

$$\epsilon = \sum_m q_{\text{eff}} m^2 |\xi_m|^2 + \frac{1}{2}c_0 n + \frac{1}{2}c_1 n |\vec{f}|^2. \tag{6.2}$$

^{87}Rb features repulsive density-density interaction, i. e. $c_0 > 0$ and the $F = 1$ hyperfine manifold features ferromagnetic spin-spin interactions $c_1 < 0$. In principle antiferromagnetic interactions can be probed using the $F = 2$ hyperfine manifold [110].

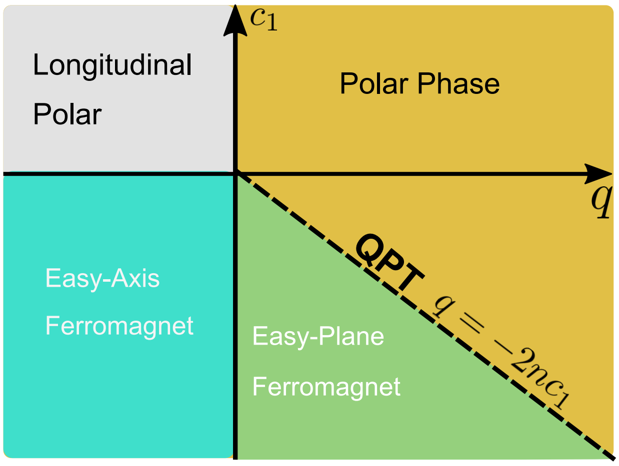

Figure 6.1: **Spin-1 mean-field phase diagram.** For ferromagnetic interactions ($c_1 < 0$) three different regimes are found. The easy-axis ferromagnet (negative q), the easy-plane ferromagnet and the polar phase. The latter two are separated by a quantum phase transition at $q = -2nc_1$.

From minimizing this energy functional we obtain the three different ground states for the ferromagnetic case (see Fig. 6.1). For negative detunings $q < 0$ we find the *easy-axis ferromagnetic phase* with a ground state spinor $\xi = (1, 0, 0)$ or $\xi = (0, 0, 1)$. This state can, however, only be reached by preparing the system with finite magnetization as the z-component of the spin is globally conserved by the dynamics. Reminding ourself of the level scheme (Fig. 5.2b), for $q < 0$ the behaviour is intuitively clear as the $m_F = \pm 1$ levels are energetically lower than $m_F = 0$. Reversing this argument, we find that for a large positive detuning the mean-field ground state is the *polar state* with $\xi = (0, 1, 0)$. When the detuning q is on the order of the interaction energy nc_1 the system favours a magnetization in the transversal direction. For $0 < q < 2nc_1$ one finds the *easy-plane ferromagnetic phase* with the ground state spinor

$$\left(\sin\theta/\sqrt{2}, \cos\theta, \sin\theta/\sqrt{2}\right)^T , \tag{6.3}$$

where $\sin\theta = \sqrt{1/2 + q/(4nc_1)}$. In this regime the system favours occupation in all three states and the negative sign of the interaction in front of the spin-spin interaction term leads to a spin in the transversal plane as the ground state. All spin directions in plane are equally likely as the Hamiltonian is invariant under rotations around F_z and with that this symmetry gets spontaneously broken in the ground state. The spin length is a smooth function of q and maximal at $q = 0$, where the system features the so-called *isotropic phase* and the ground state is a fully elongated spin in any direction of the spin sphere.

Up to now the discussion refers to a homogeneous condensate at $T = 0$. In general, the spin and the density degree of freedom can have different condensation temperatures [123]. In [124] a finite T phase diagram for the spin-1 system is discussed. The authors find that the phase transition boundary to the easy-plane ferromagnet is temperature-dependent. For temperatures above a certain threshold,

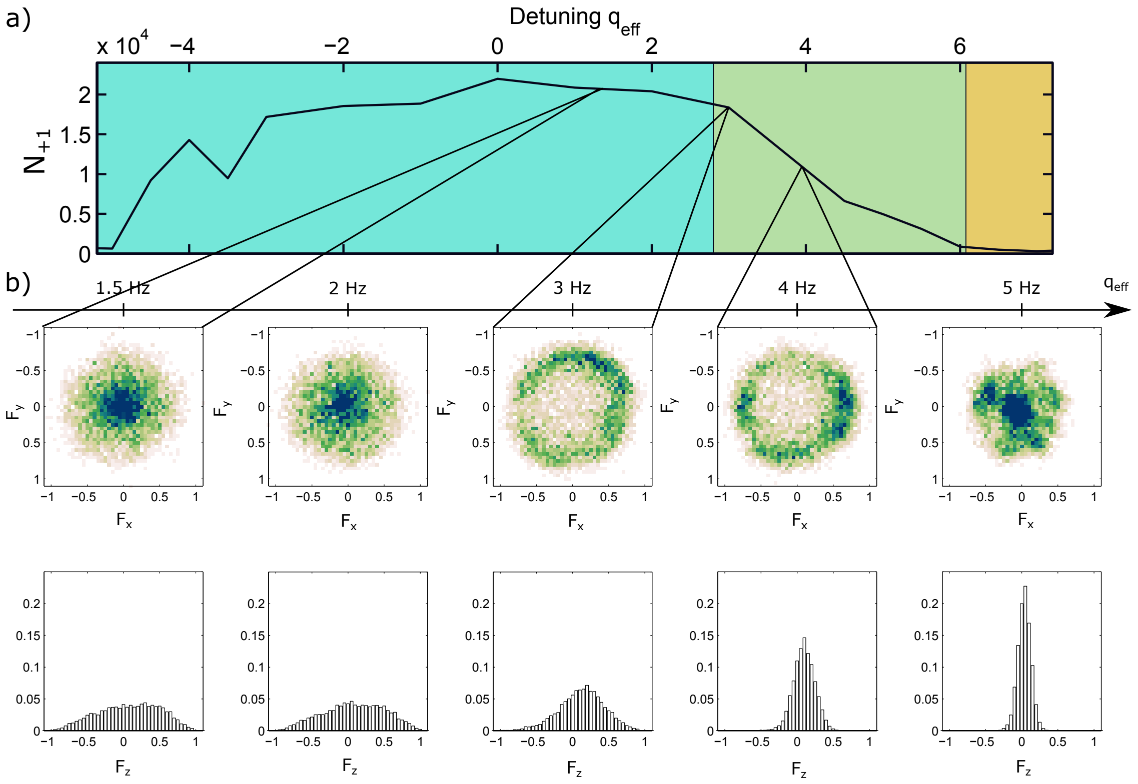

Figure 6.2: **Histograms of spin degree of freedom for different regimes.** a) Spectroscopic measurement of spin-changing collision resonance for the employed parameters. Colours indicate the region in the phase diagram (see Fig. 6.1). b) We show the histograms for the transversal spin (upper row) as well as for the z-direction of the spin for different q_{eff}. The histograms incorporate ~ 50 experimental realizations and all spatial points. In the easy-plane phase we find an elongated spin in the transversal plane with well defined spin length. However, the easy-axis phase features enhanced fluctuations in z-direction.

the easy-plane ferromagnetic phase is absent. This can be understood as the different "density condensates" having no coherences any more.

6.2 Experimental study

Different to earlier studies [125], we probe the mean-field ground states by observing the dynamics after a quench. Initially we prepare the polar state at a large positive detuning and perform a quench by switching on the microwave dressing. For $q_{\mathrm{eff}} < 5\,\mathrm{Hz}$ we find a growth of the side mode populations (see chapter 7).

To properly adjust q_{eff}, we make a spectroscopic measurement of the spin-changing collision resonance [126] consisting of 4 s evolution at a fixed q_{eff} starting from the polar state and measuring the atom numbers in the side modes. Plotting the summed relative side mode population N_{+1}/N_{tot} (see Fig. 6.2a) as a function of q_{eff} we find a resonance-like feature. For all measurements shown in this thesis we adjust the value of q_{eff} relative to the right edge, which we identify as $q = 2nc_1$, where the phase transition separating the polar and the easy-plane ferromagnetic phase takes place. Indeed, there is an offset of q_{eff} relative to "real" q which is determined in the next chapter by probing the instabilities and comparing to Bogoliubov theory. This means that values of q_{eff} given in the following have always to be seen relative to the corresponding spectroscopy.

Here, we employ the full spin readout after 15 s evolution time. This constitutes a measurement of the system at long evolution times – both absolute and relative to the spin-spin interaction time scale. With absolute we mean that for an ultracold atomic system these long times demand for high stability of the employed parameters. The spin-spin interaction is on the order of 2 Hz resulting in a typical time scale of $t_s = 500\,\text{ms}$. Thus, we probe the system at $\sim 30\,t_s$ when evaluating the histograms.

We characterize the state after the evolution time by showing histograms of the spin degree of freedom obtained from taking into account a central region of the trap ($\sim 150\,\mu$m) and ~ 50 experimental realizations. In Fig. 6.2b we show the measured two-dimensional probability distributions of the spin in the transversal plane (upper panel). We find structures qualitatively resembling the expectations from the mean-field phase diagram. In the regime $2.5\,\text{Hz} < q_{\text{eff}} < 5\,\text{Hz}$, corresponding to the easy-plane ferromagnetic phase, the histograms feature a ring-like shape. This results from a well-defined spin length in the plane with small fluctuations of its length. The fluctuations in the z-direction of the spin for large q are relatively small, which can be expected for the easy-plane phase, but grow when going to smaller q. Finally, for $q_{\text{eff}} < 2.5\,\text{Hz}$ we still find finite fluctuations in plane but no ring-like shape. However, the fluctuations in z-direction grow and get even larger than the fluctuations in the transversal plane.

It is important to note that the system (presumably) has not equilibrated to the final ground state of the system in the time regime probed within the experiment. In contrast, we show, in the following chapter, that especially the transversal spin degree of freedom is still highly excited in the phase degree of freedom even though its transversal spin length resembles the mean-field ground state expectation.

Chapter 7

Extreme conditions

In chapter 2 we discussed under what conditions we expect new features far from equilibrium and especially when the system is expected to behave universal. Here, we resume this discussion and describe how these conditions can be prepared experimentally using the controllability offered by the implemented spin-1 system. First, we give a brief introduction into Bogoliubov theory [127] with which we will identify unstable momentum modes in the different regimes of the phase diagram depending on the initial condition. We present experimental studies of these instabilities from two different initial conditions and compare our findings to the theoretical predictions. Finally, we show an implementation of a different initial condition, prepared near the bottom of the mexican hat potential but highly excited in the phase degree of freedom. This also results in an extreme condition giving access to new dynamics.

7.1 Bogoliubov theory for spin-1 systems

In this section we present the results known from Bogoliubov theory for the spin-1 system which will be essential to understand the initial unstable dynamics. We provide a summary of the results obtained in [116, 128]. Bogoliubov theory aims to describe the fluctuations around a given state derived in mean-field theory. Generally the idea is to expand the bosonic fields as

$$\hat{\psi}_m = \psi_m + \delta\hat{\psi}_m, \tag{7.1}$$

where ψ_m is the mean-field result calculated in chapter 6 and $\delta\hat{\psi}_m$ are the fluctuations. This ansatz is put in the Hamiltonian and only terms at most quadratic in the fluctuations are kept.

For the homogeneous case it is sensible to work in momentum space by Fourier transforming the bosonic field operators as

$$\hat{\psi}_m = \frac{1}{\sqrt{L}} \sum_k \hat{a}_{k,m} \mathrm{e}^{i2\pi ky}. \tag{7.2}$$

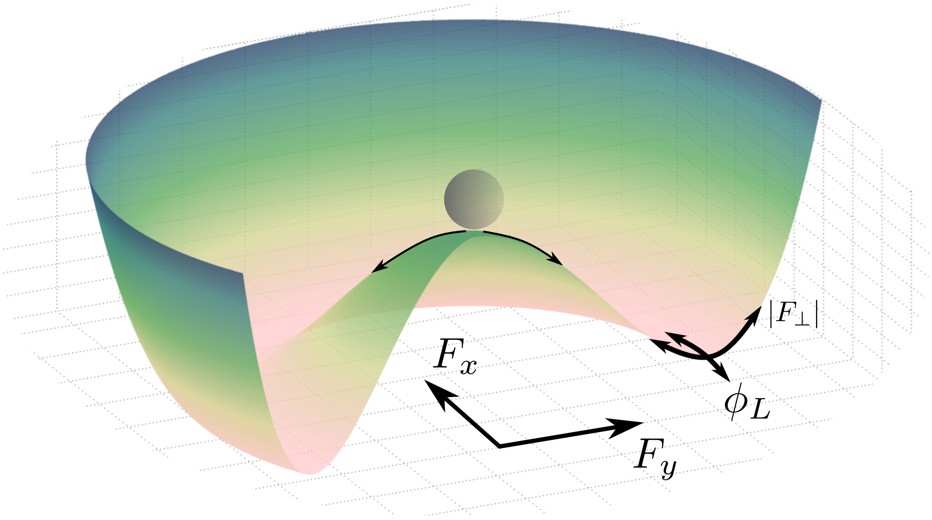

Figure 7.1: **Extreme condition.** Placing the system at the unstable fixed point of the mean-field energy potential leads to unstable momentum modes in the transversal spin degree of freedom. The flat bottom along the Larmor phase ϕ_L degree of freedom is reminiscent of the massless excitations of the $\hat{a}_{k,f_z}$-mode (see Eq. (7.6)).

$\hat{a}_{k,m}$ is the annihilation operator at momentum k in the mode m and L is the length of the system. As we only discuss the one-dimensional case here, we use $k = 1/\lambda$ as the spatial momentum variable[1] and y as the space coordinate.

The idea is now to insert relation 7.1 in the microscopic Hamiltonian and keep only terms up to second order in the fluctuations. The highly occupied $k = 0$ mode is substituted by a c-number $\hat{a}_{0,m} = \sqrt{N}\xi_m$. This procedure is appropriate as long as the interaction is weak and with that the resulting quantum depletion $\sum_{k\neq 0,m} \hat{a}^\dagger_{k,m}\hat{a}_{k,m}$. The exact form of the Hamiltonian for the different mean-field states can be found in [116].

For diagonalizing the obtained quadratic Hamiltonian we define new quasiparticle operators

$$\hat{b}_{k,i} = \sum_m u^*_{k,m}\hat{a}_{k,m} + v_{-k,m}\hat{a}^\dagger_{-k,m}\,, \tag{7.3}$$

where the index i is not necessarily connected to the hyperfine state but can also indicate fluctuations in different spin directions. The mode functions $u_{k,m}$ and $v_{k,m}$ are implicitly defined by diagonalizing the Hamiltonian. Further, the b's have to satisfy the bosonic commutation relation which leads to the restriction $\sum_m |u_{k,m}|^2 - |v_{k,m}|^2 = 1$.

We are going to find two types of excitations: stable excitations around the mean-field ground state and instabilities featuring exponential growth. The first type has purely real eigenfrequencies, giving the energy of the excitations as a function of the spatial momentum k. The instabilities are identified by a purely imaginary dispersion relation; the time evolution, usually described by $\mathrm{e}^{-i\omega t}$, will then lead to

---

[1] Throughout this thesis the spatial momentum $k = 1/\lambda$ has unit 1/length missing the usual 2π, such that the associated length scale can be read off as $1/k$.

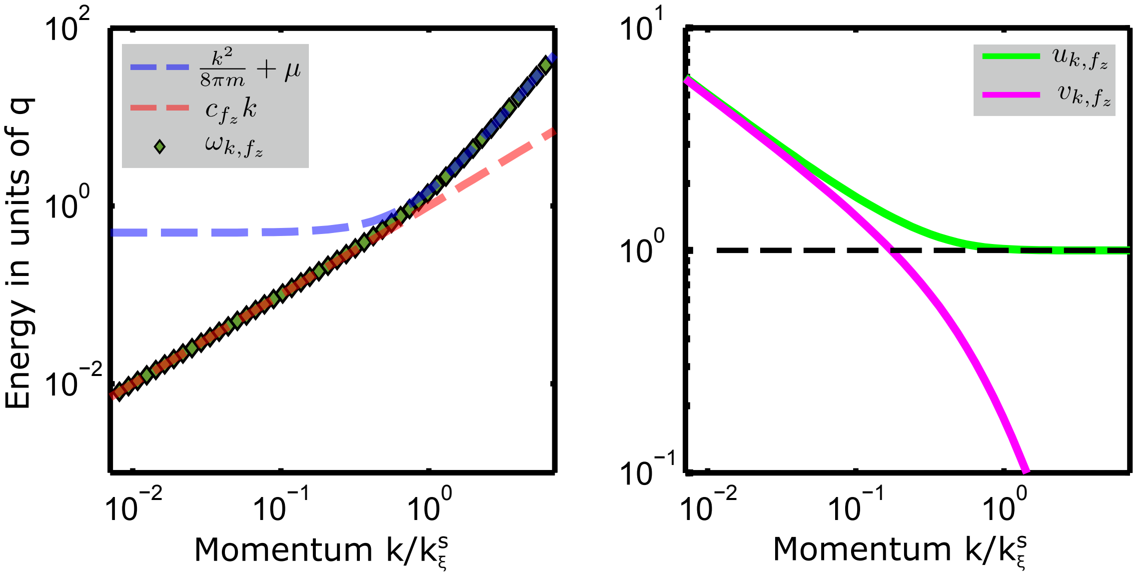

Figure 7.2: **Dispersion and mode functions in easy-plane phase.** a) The green diamonds show the Bogoliubov spectrum from equation 7.8 as a function of momentum k/k_ξ^s in units of q. We compare to a linear dispersion with speed of sound c_{f_z} (red) and a quadratic dispersion (blue) with $\mu = q/2$. b) Dimensionless mode functions u_{k,f_z} (magenta) and v_{k,f_z} (green) as a function of k/k_ξ^s.

exponentially fast growth of the occupation of the corresponding modes. It helps to think about placing the mean-field solution on the unstable fixed point of a mexican-hat-like potential. For example for the polar state we will identify the axes of the energy landscape to be F_x and F_y (see Fig. 7.1). The quadratic approximation in the fluctuations corresponds to a solution which is only valid close to the unstable fixed point where the negative quadratic part dominates. The fast initial dynamics describe how the state “rolls” down into the valley. In the following chapters we conclude that this picture also gives an intuition for the long time behaviour.

Here, we compare our experimental findings to Bogoliubov theory for the homogeneous system. Recently, it was shown that the character of the excitations and the properties of the most unstable modes found do not change qualitatively in the presence of a trapping potential in one spatial direction [129].

7.1.1 Spin modes for the easy-plane ferromagnet

Here, we first introduce the Bogoliubov modes about a spin in the transversal plane. In the preceding chapter we already gave the mean-field ground state in the easy-plane ferromagnetic phase as $\left(\sin\theta/\sqrt{2}, \cos\theta, \sin\theta/\sqrt{2}\right)^T$. For ease of notation we introduce the following fluctuation operators

$$\hat{a}_{k,d} = \frac{\sin\theta}{\sqrt{2}}\left(\hat{a}_{k,1} + \hat{a}_{k,-1}\right) + \cos\theta \hat{a}_{k,0} \,, \tag{7.4}$$

$$\hat{a}_{k,\theta} = \frac{\cos\theta}{\sqrt{2}}\left(\hat{a}_{k,1} + \hat{a}_{k,-1}\right) - \sin\theta \hat{a}_{k,0} \,, \tag{7.5}$$

$$\hat{a}_{k,f_z} = \frac{1}{\sqrt{2}}\left(\hat{a}_{k,1} - \hat{a}_{k,-1}\right) . \tag{7.6}$$

Let us first discuss the f_z mode $\hat{a}_{k,f_z}$: We diagonalize the subpart of the Hamiltonian belonging to $\hat{a}_{k,f_z}$ by

$$u_{k,f_z} = \sqrt{\frac{\epsilon_k + hq/2 + E_{k,f_z}}{2E_{k,f_z}}} \,, \qquad v_{k,f_z} = \sqrt{\frac{\epsilon_k + hq/2 - E_{k,f_z}}{2E_{k,f_z}}} \,, \tag{7.7}$$

with the single particle energy $\epsilon_k = \hbar^2 k^2/2m$. The Bogoliubov spectrum E_{k,f_z} is given by

$$\hbar\omega_{k,f_z} = \sqrt{\epsilon_k \left(\epsilon_k + hq\right)}. \tag{7.8}$$

In Fig. 7.2 we show the spectrum and the mode functions as a function of k in units of the *spin healing momentum* $k_\xi^s = \sqrt{2mhq}/h$. For low momenta $k/k_\xi^s < 1$, the dispersion is linear with a speed of sound $c_{f_z} = \sqrt{hq/(2m)}$ and $\mu = hq/2$. We further see that $u_{k,f_z} \approx v_{k,f_z}$ in this regime which indicates that the excitations are phononic phase excitations. Expanding the underlying fluctuation operator $\hat{a}_{k,f_z}$ for low k and neglecting density fluctuations we find that these excitations are connected to changes in the Larmor phase (see Appendix A). This corresponds to the Goldstone mode along the rim of the mexican hat potential (see Fig. 7.1).

For the two remaining modes we define the following Bogoliubov operators

$$\hat{b}_k^+ = u_{k11}\hat{a}_{k,d} + u_{k12}\hat{a}_{k,\theta} + v_{k11}\hat{a}^\dagger_{-k,d} + v_{k12}\hat{a}^\dagger_{-k,\theta} \tag{7.9}$$

$$\hat{b}_k^- = u_{k21}\hat{a}_{k,d} + u_{k22}\hat{a}_{k,\theta} + v_{k21}\hat{a}^\dagger_{-k,d} + v_{k22}\hat{a}^\dagger_{-k,\theta} \tag{7.10}$$

For the definitions of u_{kij} and v_{kij} see [128]. The '+'–branch is dominated by u_{k11} and v_{k11}. With that we find that $\hat{b}_k^-$ features exactly the same structure as the Bogoliubov result for a one-component Bose gas, here, however, with $g = c_0 + c_1$; it describes the density fluctuations on top of the condensate. The '-'–branch is dominated by u_{k22} and v_{k22}. We find a gapped spectrum with gap $\Delta = \sqrt{4(nc_1)^2 - q^2}$ and the excitations are connected to fluctuations of the transversal spin length (see Appendix A).

The gapped mode in the radial direction is reminiscent of the Higgs mode in a mexican hat effective potential describing the fluctuations around the easy-plane ground state. We have already seen in chapter 6 that the phase excitations are energetically favoured. The histograms of $F_\perp$ showed a structure resembling a circle indicating reduced fluctuations in the radial directions and a highly excited phase degree of freedom (see Fig. 6.2).

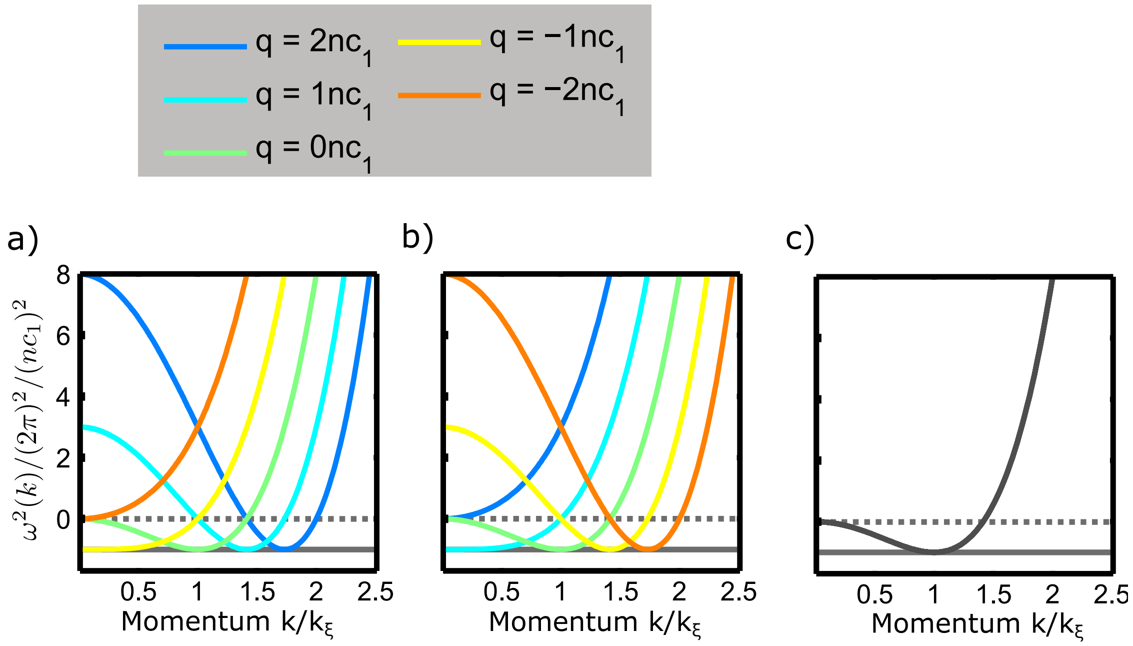

Figure 7.3: **Energy spectra for spin instabilities.** We show the squared dispersion relation $\omega(k)^2$ as a function of k/k_ξ, with $k_\xi = \sqrt{2mhn|c_1|}/h$, for the spin instabilities expanding about the polar state a) and the antiferromagnetic state b). Different values of q are colour-coded. In contrast to the transversal spin instability, the demixing instability (shown in c) does not depend on q and features excitations in F_z. The solid black line indicates $\omega(k) = 2\pi \times nc_1$ and the dashed line indicates $\omega(k) = 0$.

7.1.2 Instabilities from expanding about the polar and the antiferromagnetic state

Up to now, we discussed stable configurations and thus the found spectra are real-valued. However, if the state is not the ground state in the investigated phase, the eigenfrequencies can become imaginary. This results from the negative curvature of the energy landscape when prepared at an unstable fixed point. For purely imaginary eigenfrequencies $\omega_k = i\gamma$ this leads to unstable momentum modes. These will grow exponentially in time $\propto \exp(\gamma t)$ resulting in high occupations of initially unoccupied modes. This mechanism is used to drive the system far out of equilibrium.

Strictly speaking, Bogoliubov theory can only capture infinitesimally short times of unstable evolution. However, it was shown that it can give good descriptions of the observations made in experiment [130]. We proceed by introducing the relevant instabilities after initializing the polar state and the antiferromagnetic state.

Polar state

Diagonalizing the Hamiltonian obtained from expanding about the polar state gives the following two Bogoliubov modes:

$$\hat{b}_{k,\pm 1} = -\sqrt{\frac{\epsilon_k + hq + hnc_1 + E_{k,\pm 1}}{2E_{k,\pm 1}}}\hat{a}_{k,\pm 1} + \sqrt{\frac{\epsilon_k + hq + hnc_1 - E_{k,\pm 1}}{2E_{k,\pm 1}}}\hat{a}^{\dagger}_{-k,\mp 1}\,. \tag{7.11}$$

The associated dispersion relation reads

$$\hbar\omega_{k,\pm 1} = \sqrt{(\epsilon_k + hq)\,(\epsilon_k + hq + h2nc_1)}. \tag{7.12}$$

The two modes are degenerate and thus the sum and the difference of the two operators also diagonalize the Hamiltonian. These modes describe excitations in the transversal spin degree of freedom.

In Fig. 7.3a we show the square of the dispersion relation for different values of q. We find negative values, indicating unstable momenta, for $q < -2nc_1$ where the polar state is not the mean-field ground state. The most unstable mode, defined by the largest instability rate, is given by

$$k_{\mathrm{mu}} = 0 \qquad \text{for} \qquad -nc_1 < q < -2nc_1\,, \tag{7.13}$$

$$k_{\mathrm{mu}} = \frac{\sqrt{2mh(q + nc_1)}}{h} \qquad \text{for} \qquad q < -nc_1\,. \tag{7.14}$$

The corresponding rate is bounded by the interaction energy hnc_1.

Antiferromagnetic state

The *antiferromagnetic state* $\xi = 1/\sqrt{2}\,(1,0,1)^T$ features two different instabilities. Besides transversal spin excitations it also has dynamics in the F_z-component of the spin.

First we find one Bogoliubov mode describing transversal spin excitations

$$\hat{b}_{k,0} = -\sqrt{\frac{\epsilon_k - hq + hnc_1 + E_{k,0}}{2E_{k,0}}}\hat{a}_{k,0} + \sqrt{\frac{\epsilon_k - hq + hnc_1 - E_{k,0}}{2E_{k,0}}}\hat{a}^\dagger_{-k,0} \tag{7.15}$$

with the corresponding dispersion relation

$$\hbar\omega_{k,0} = \sqrt{(\epsilon_k - hq)\,(\epsilon_k - hq + h2nc_1)}, \tag{7.16}$$

which is shown for different q in Fig. 7.3b. We find unstable modes for $q > 2nc_1$ and the most unstable mode is given by

$$k_{\mathrm{mu}} = 0 \qquad \text{for} \qquad nc_1 > q > 2nc_1\,, \tag{7.17}$$

$$k_{\mathrm{mu}} = k_{\mathrm{mu}} = \frac{\sqrt{2mh(q - n|c_1|)}}{h} \qquad \text{for} \qquad q > nc_1\,. \tag{7.18}$$

The q-dependence is similar to the polar state instability, however, it is mirrored at $q = 0$.

We further find a mode whose dynamics we can easily study in the experiment. It describes the demixing dynamics of the $m_F = \pm 1$-components. The Bogoliubov quasiparticle operator is given by

$$\hat{b}_{k,-1} = \sqrt{\frac{\epsilon_k + hnc_1 + E_{k,-1}}{2E_{k,-1}}}\frac{\hat{a}_{k,1} - \hat{a}_{k,-1}}{\sqrt{2}} + \sqrt{\frac{\epsilon_k + hnc_1 + E_{k,-1}}{2E_{k,-1}}}\frac{\hat{a}^\dagger_{-k,1} - \hat{a}^\dagger_{-k,-1}}{\sqrt{2}}\,. \tag{7.19}$$

It features unstable momentum modes in the F_z projection of the spin and is independent of q. The dispersion relation is given by

$$\hbar\omega_{k,-1} = \sqrt{\epsilon_k\,(\epsilon_k + h2nc_1)}\,. \tag{7.20}$$

From this we find the most unstable mode

$$k_{\mathrm{mu}} = k_\xi = \frac{\sqrt{2mhn|c_1|}}{h}. \tag{7.21}$$

Physically, it results from the difference of the inter- and intraspecies scattering lengths of $m_F = \pm 1$. It is energetically favourable for the atoms to spatially separate which is the underlying reason for the demixing dynamics.

The demixing instability in two-component gases was already studied experimentally exploring phase transition physics [112] and numerical studies suggest the possibility of finding coarsening dynamics in the long-time limit [67]. Our system allows us to employ values of q with the demixing instability only and therefore may give access to interesting two-component BEC physics.

In the experiment we measure particle numbers which we can associate with the particle operators a_i. Thus the Bogoliubov transformation has to be inverted to find the particle operators in terms of the quasi-particles. For measuring the spin, it is clear that the particle operator is linear in the quasi-particle operator featuring the instability. However, in case of measuring the F_z-component as employed later for the demixing it is not evident that $\hat{F}_z$ is linear in $\hat{b}_{k,-1}$. In Appendix A we show that it is indeed true and explain why we expect also the correlation functions of F_z to grow at k_{mu} (see Eq. (7.21)).

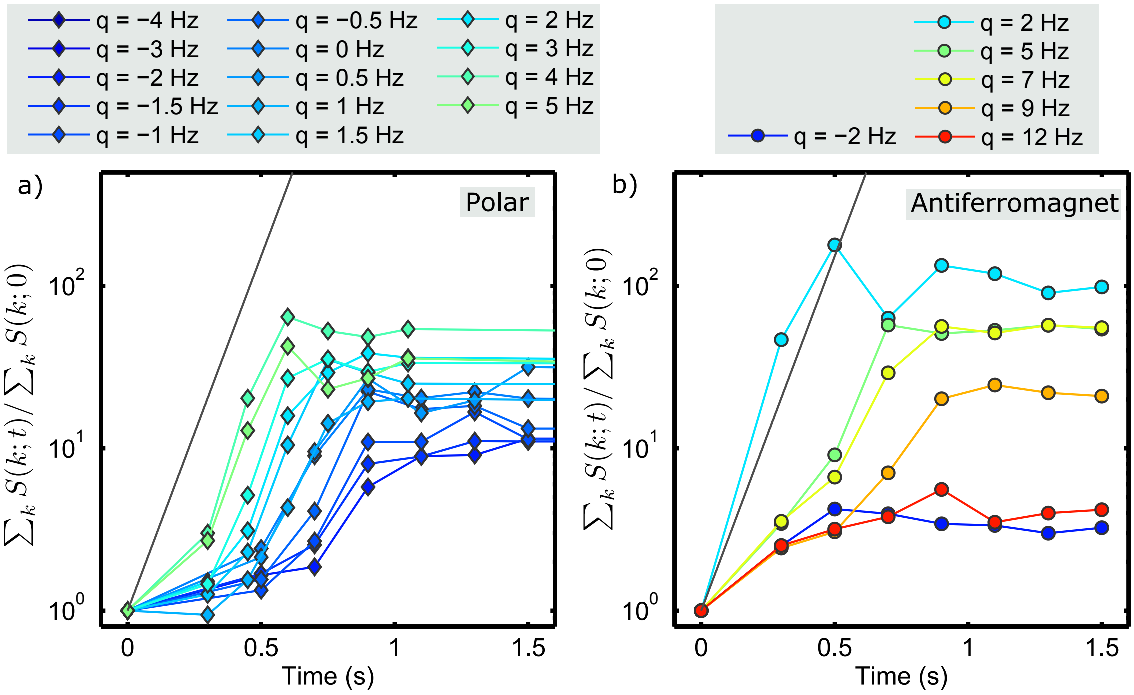

Figure 7.4: **Exponential growth of summed spectra.** We show the summed structure factor for $F_\perp(y)$ as a function of evolution time for the polar a) and the antiferromagnetic b) initial state. For comparability, the sums are normalized to their initial value at $t = 0\,\mathrm{s}$. The data points show the expected exponential growth for short times ($< 1\,\mathrm{s}$) and a saturation behaviour. We compare to the maximal expected exponential growth $\propto \exp(\gamma_{\max} t)$ with $\gamma_{\max}/2\pi = nc_1$ (grey line).

7.2 Studying instabilities experimentally

For preparing the polar state we transfer the atoms via a microwave π-pulse from $(1, -1)$, where the BEC is produced, to $(2, 0)$. A second microwave π-pulse from $(2, 0)$ to $(1, 0)$ initializes the polar state. We clean the residual population in $(1, \pm 1)$ by applying a strong magnetic field gradient repelling the atoms in $m_F \neq 0$ from the trap. In case of the antiferromagnetic state we further apply a $\pi/2$ rf rotation in $F = 1$ which leads to an equal population of $(1, \pm 1)$. After the preparation the microwave dressing is switched on and the detuning is adjusted corresponding to the desired value of q_{eff}.

For the instabilities in the transversal spin we observe the dynamics by employing the full spin readout, which gives us access to all three spin directions. The demixing is observed with direct imaging of the F_z-projection without further rotations. We calculate the *structure factor* $S(k)$ for the observable $F_i(y)$ by Fourier transforming the spatial correlation function [2]

$$G(\Delta y) = \langle \frac{1}{N} \sum_y F_i(y) F_i(y + \Delta y) \rangle \ , \tag{7.22}$$

---

[2] We calculate the correlation function using the MATLAB function *xcorr.m*.

where $i \in \{\perp, x, z\}$ and $\langle \cdot \rangle$ is the ensemble average; for this chapter we use ~ 50 experimental realizations for averaging. The Fourier transform is performed with respect to the coordinate Δy giving spatial momenta $k = 1/\lambda$, where the smallest momentum is $k_L = 1/2L$ with $L \approx 166\,\mu\text{m}$ being the system size. We normalize the correlation function to the number of points $N = 132$. This results in a correlation function going to zero for $\Delta y = L$ and thus facilitating the Fourier transform.

For the two measurements on the transversal spin instabilities, the right edge of the spectroscopy measurement is at $q_{\text{eff}} = 6\,\text{Hz}$ (see Fig. 6.2a for the spectroscopy). Before going into detail about the momentum dependence of the instabilities, we show the summed spectra as a function of evolution time for both the polar as well as the antiferromagnetic state in Fig. 7.4. All values are normalized to the initial value of the sum at $t = 0\,\text{s}$. The semi-logarithmic plots indicate exponential growth of the the summed spectra for short evolution times $t < 1\,\text{s}$ and a saturation behaviour for $t > 1\,\text{s}$.

Qualitatively, we find growth rates in the range of $\gamma/2\pi = nc_1$ with $nc_1 = 1.6\,\text{Hz}$ (grey line), which is expected from the Bogoliubov dispersion relation. The saturation behaviour results from the finite number of atoms that can scatter into the empty mode(s); the depletion of initially highly occupied modes leads to a breakdown of the Bogoliubov approximation. For comparing the experimental data with the Bogoliubov predictions in momentum space, we use times within the range of exponentiall growth.

Spin instabilities from the polar state

We now turn to a momentum resolved study of the unstable initial growth. First we analyze the time evolution for a fixed detuning in Fig. 7.5. As expected from Eq. (7.14), we find exponential growth peaked around the momentum $k_{\text{mu}} \approx 0.04\,\mu\text{m}^{-1}$ for times $< 1\,\text{s}$. The fast growth is followed by a redistribution over a broad range of momenta, where we still find occupations for evolution times $\sim 15\,\text{s}$.

To compare the momentum dependence of the dynamics with the homogeneous theory we record spectra for different q_{eff}. In Fig. 7.6 we show the spectra for $F_\perp$ at a fixed evolution time $t = 700\,\text{ms}$. We find a most unstable mode which depends on q, where for smaller q the spatial momentum k gets larger. Intuitively this can be understood by a simple energy argument: As q gets smaller the $m_F = 0$ state is shifted up in energy relative to the $m_F = \pm 1$ states. The accessible amount of energy for the spin-changing collision process becomes larger and thus it is possible to occupy higher momenta.

We compare the spectra in Fig. 7.6 (right panel) with the expectations from Bogoliubov theory for $nc_1 = 1.6\,\text{Hz}$ and find qualitative agreement for the most unstable mode (grey solid line) as well as the range of unstable momenta (dashed lines). Moreover, we find that $q_{\text{eff}} \approx 2.8\,\text{Hz}$ corresponds to the "real" $q = 0$.

Though the experimental results fit well with the predictions from Bogoliubov theory in general, there are some discrepancies that we are not yet able to explain and that are open questions for potential future investigations. First, Bogoliubov theory predicts constant growth rates for the most unstable modes for $q < |nc_1|$. Experimentally, however, we see that larger k's grow slower than expected. Second,

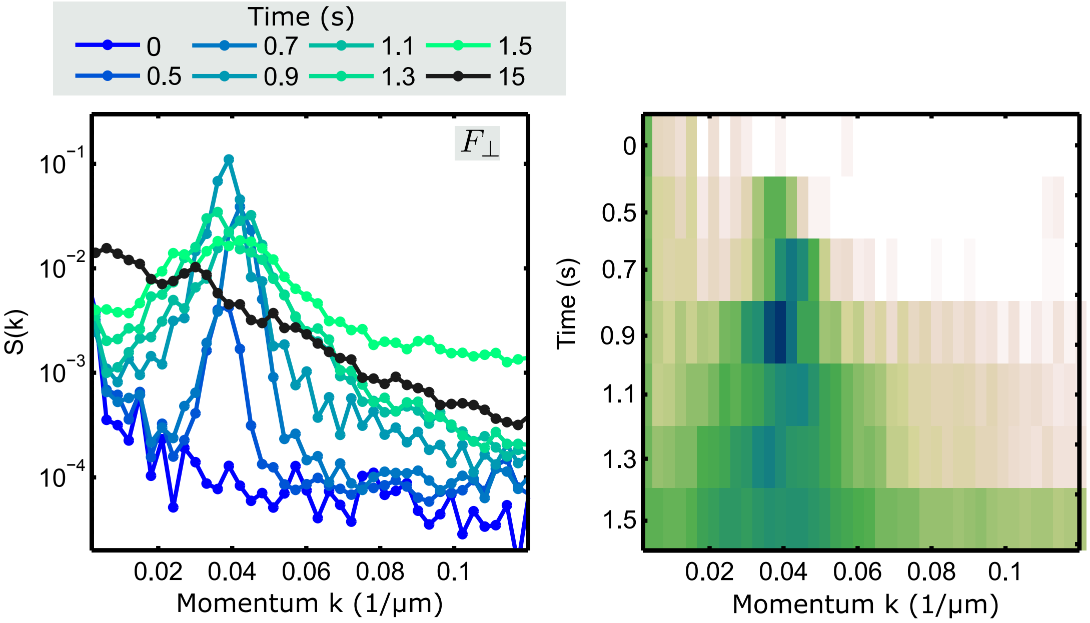

Figure 7.5: **Structure factor as a function of time for polar state.** Structure factor as a function of the momentum k for $q_{\text{eff}} = 0.5\,\text{Hz}$ and different evolution times for the observables $F_\perp$ (left panel). The right panel shows the same data as a function of time t and k with colour-coded logarithmic amplitude. We find an unstable growth peaked around $k_{\text{mu}} \approx 0.04\,\mu\text{m}^{-1}$ for times $< 1\,\text{s}$ followed by a redistribution and occupation of a broad range of momenta.

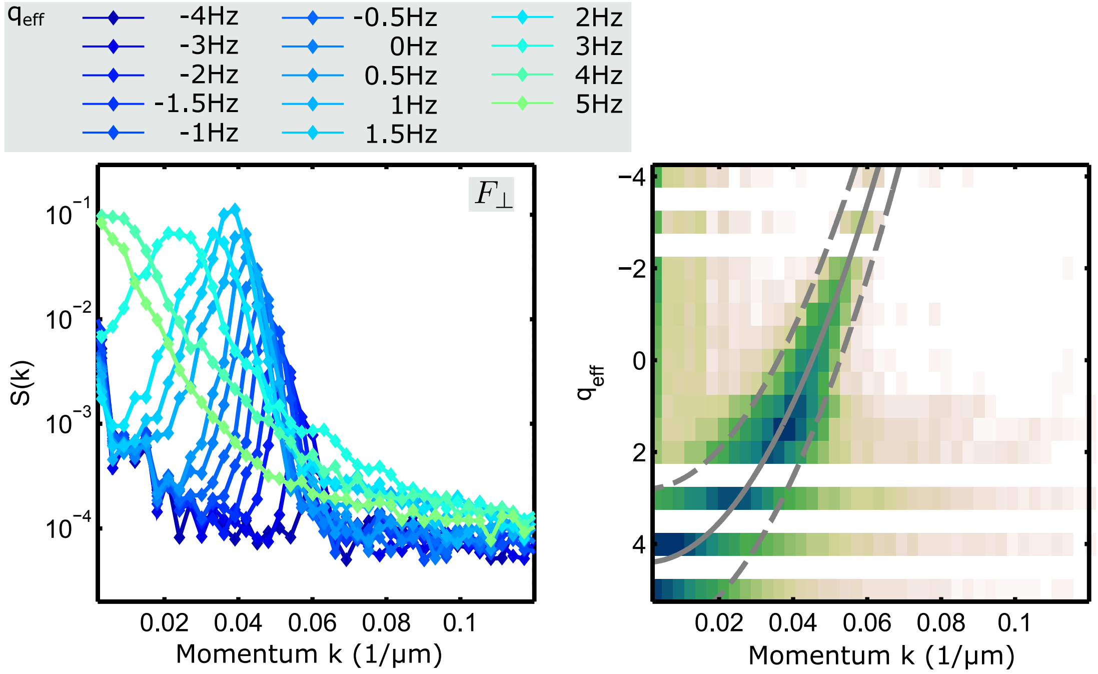

Figure 7.6: **Studying the q dependence of the instabilities.** For a fixed evolution time $t = 700\,\mathrm{ms}$ we show the spectra of $F_\perp$ as a function of the momentum k for different q_{eff}. We find a q dependent most unstable mode growing in the transversal spin direction. We compare the found spectra to the prediction from Eq. (7.12) where the solid line indicates the most unstable mode (right panel). The dashed lines indicate the minimal and maximal k which is unstable. We find qualitative agreement.

the range of $q_{\mathrm{eff}} < 0\,\mathrm{Hz}$ was just accessible after reducing the heating by lowering the waveguide power.

The shown spectra and their agreement with theoretical predictions highlight the experimental control over the momentum occupation numbers rendering the system versatile for studying non-equilibrium dynamics.

Spin instabilities from the antiferromagnetic state

In this setting, we additionally investigated the instability in the transversal spin with the antiferromagnetic initial state. In Fig. 7.7 we show the time evolution of the spectrum of $F_\perp$ at $q_{\mathrm{eff}} = 5\,\mathrm{Hz}$. We again find a pronounced peak at the momentum $k_{\mathrm{mu}} \approx 0.04\,\mu\mathrm{m}^{-1}$ and a broad range of occupied momenta beyond 1 s evolution time.

From Bogoliubov theory the spin instability is expected to be dependent on q and we indeed find that the momentum of the most unstable mode gets larger with larger q_{eff} (see Fig. 7.8); this is consistent with the argument from before when considering all atoms in the side modes. The comparison with the theoretical curve shows that the behaviour is qualitatively captured, however, there is an offset possibly coming from different mean field shifts.

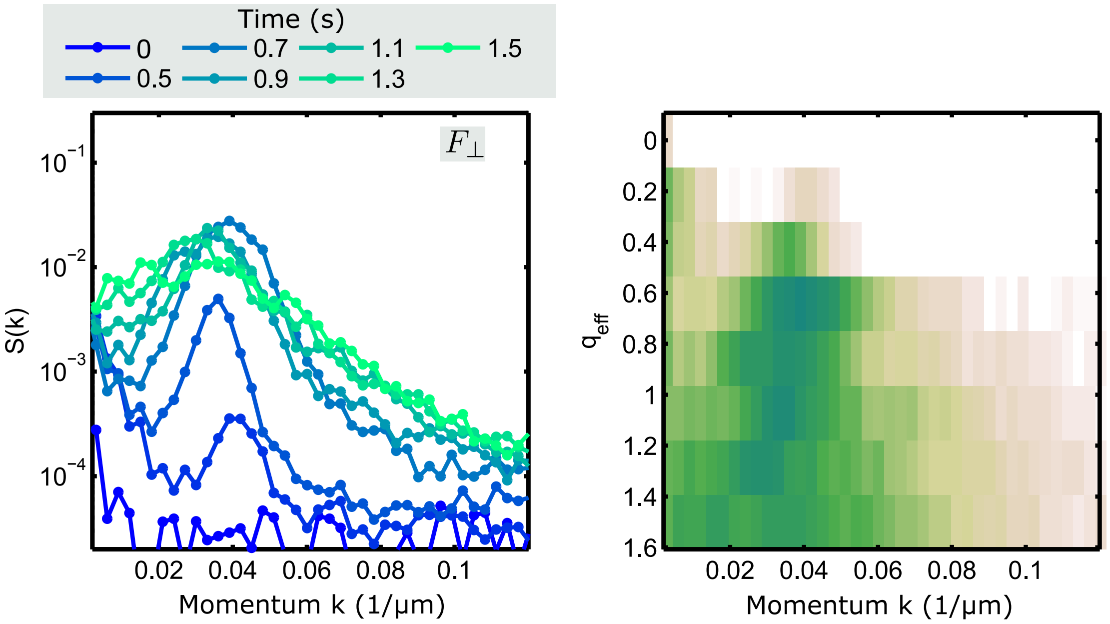

Figure 7.7: **Structure factor as a function of time for antiferromagnetic state.** At a fixed detuning $q_{\mathrm{eff}} = 5\,\mathrm{Hz}$ we observe the dynamics in the transversal spin for different times. We find a peaked growth around $k_{\mathrm{mu}} \approx 0.04\,\mu\mathrm{m}^{-1}$ for times $t < 1\,\mathrm{s}$. Left panel: Spectra in semi-logarithmic plot, times colour-coded Right panel: Colour-coded logarithm of amplitude.

It was shown in [70, 71] that the antiferromagnetic state can be an interesting initial condition producing larger F_z fluctuations and thus its control is a starting point for possible future studies of different phases.

Demixing instability from the antiferromagnetic state

We probe the demixing instability by measuring the F_z projection only. For separately analyzing the transversal spin instability we measure the F_x projection of the spin. Here, we use a higher waveguide power which allows for less q_{eff} featuring spin-changing collisions. The corresponding spectroscopy measurement can be seen in Fig. 7.9a.

We find that the F_z demixing instability is present for all q_{eff} employed in the experiment. The spectrum (shown in Fig. 7.9b) does not depend on q as demixing arises from scattering length differences. For comparison, we give in Fig. 7.9c the spectrum for the F_x component of the spin which highly depends on q_{eff} in the same manner as discussed in the previous section. Not only the most unstable mode changes as a function of the momentum, but so does the instability rate. With this measurement we show that the coupling of the two Bogoliubov modes used to describe the dynamics is negligible.

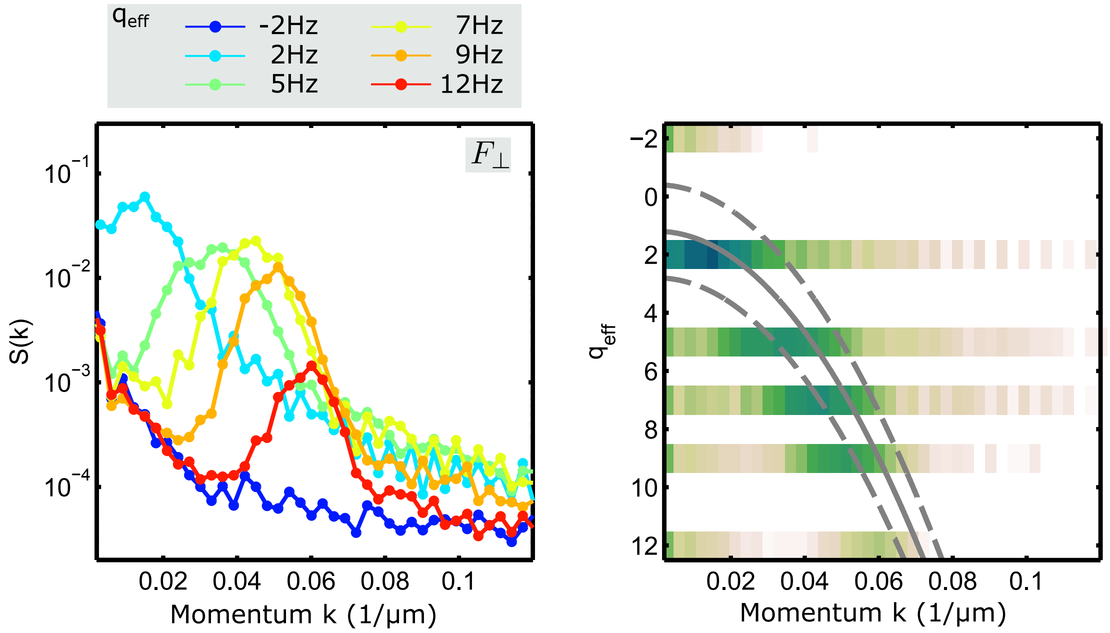

Figure 7.8: **Momentum dependence of instability from antiferromagnetic state.** Left panel: Semi-logarithmic plot of structure factor for fixed time $t = 700\,\mathrm{ms}$ and different q_{eff} (colour-coded). We find a q-dependent most unstable mode. Right panel: Same data as in the left panel but colour-coded amplitude. We compare to the most unstable mode (solid line) and the range of unstable momenta (dashed lines) obtained from Bogoliubov theory and find qualitative agreement.

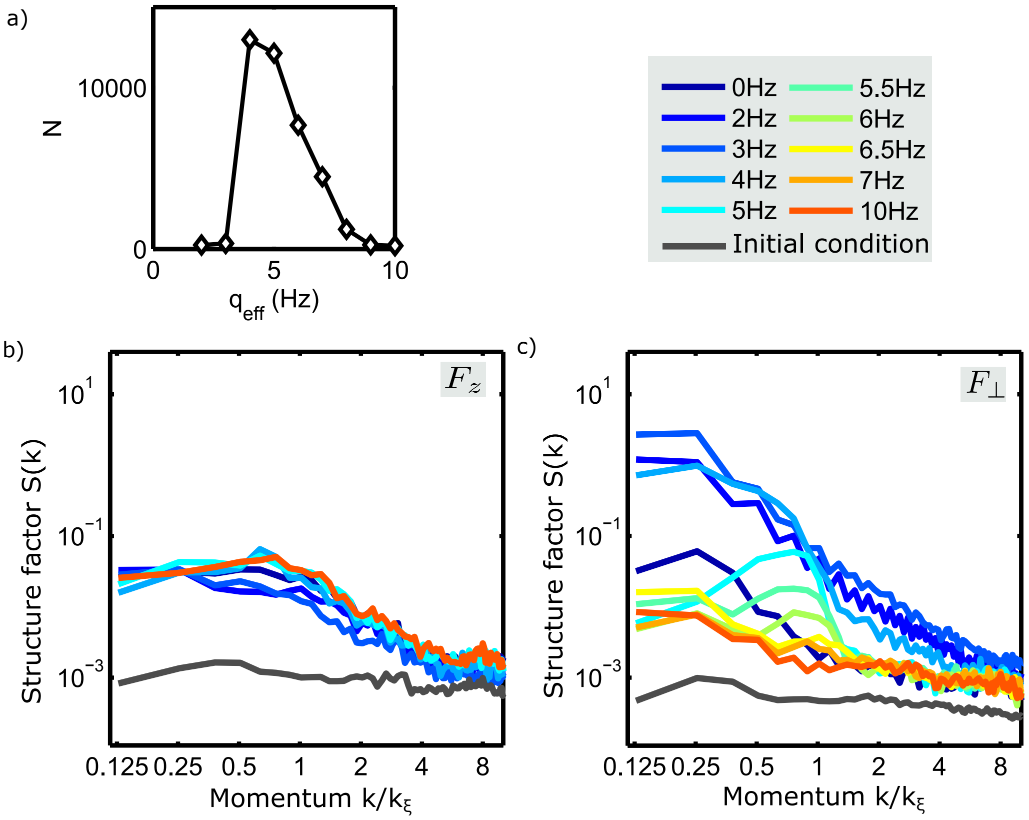

Figure 7.9: **Measurement of the demixing instability.** a) Spin-changing collision spectroscopy. b) F_z spectrum for 400 ms evolution time as a function of the spatial momentum normalized to the most unstable mode momentum k_ξ. We find a growth of momentum modes up to k_ξ which is independent of q_{eff} around $k/k_\xi = 1$. c) For comparison, we show the F_x spectrum whose momentum structure is strongly dependent on q_{eff} (compare to Fig. 7.8).

7.3 A different way to go extreme: Spin waves

Up to now, we employed instabilities to imprint excitations up to a certain length scale for preparing the system out of equilibrium. As we have seen, the minimal length scale of this process is limited, as the rate of the instabilities diminishes at some point (see Fig. 7.6). The experimental control allows us to prepare initial states with (nearly) arbitrary small length scales. One possible way, namely imprinting spin waves, is presented in this section.

For this, we prepare a fully elongated spin in the $F_x - F_y$-plane by applying a $\pi/2$ rf rotation to the atoms occupying $m_F = -1$ (fully elongated in $-z$-direction). Spin waves with a spatially modulated Larmor phase are generated by applying a weak magnetic field gradient for a fixed time. The spatially varying magnetic field leads to a linear dephasing of the spin in the $F_x - F_y$-plane. The wavelength is adjusted either by the employed time or the strength of the gradient. The atomic clouds of $(1, \pm 1)$ are also displaced with respect to each other because of the applied force and

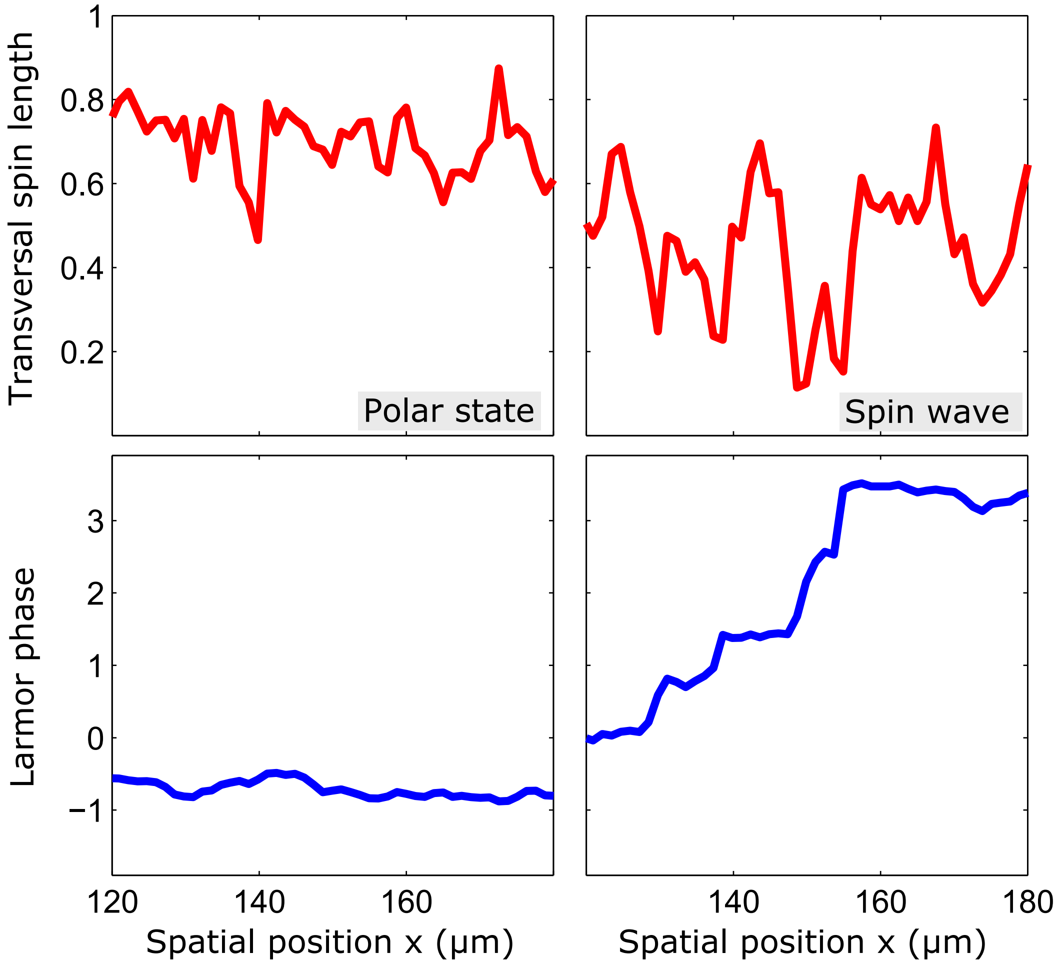

Figure 7.10: **Single shot comparison of polar state and spin wave.** Inferred from the transversal spin $F_\perp = |F_\perp e^{-i\phi_L}|$ we show the transversal spin length $|F_\perp(x)|$ (upper panel) and the Larmor phase ϕ_L for 24 s evolution time. The left and right panel compare the polar state and the spin wave, respectively. The polar state features a homogenous spin length and a smooth phase. In contrast, the spin wave features strong excitations in the spin length and associated jumps in the Larmor phase.

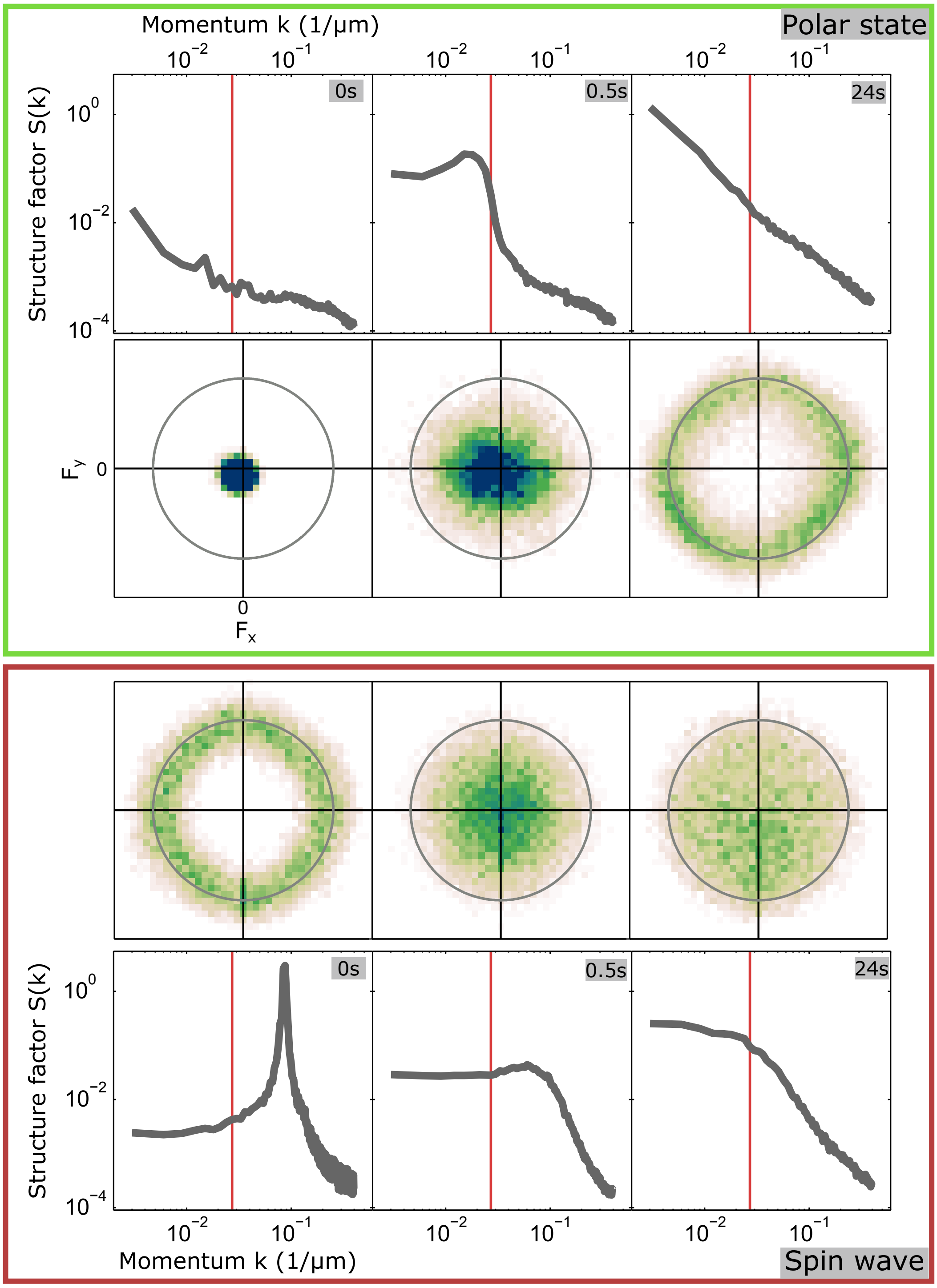

Figure 7.11: **Comparison of polar state and spin wave.** We show the structure factor $S(k)$ after different evolution times for the polar state (green box) and the spin wave (red box) as initial conditions. The red vertical line indicates the spin healing momentum k_ξ. The lower panel in the green box and the upper panel in the red box show the corresponding two-dimensional histograms of the transversal spin degree of freedom. Even though both histograms resemble a circular structure, we find at 24 s different spectra for the polar state and for the initial spin wave. We further see that the systems feature different types of spin excitations for long evolution times although the dynamics take place at the same q_{eff}.

thus the gradient should only be made reasonable large. We furthermore switch off the gradient slowly such that we observe no sloshing of the $m_F = \pm 1$ components.

Experimentally, the smallest structure size accessible by the instabilities is on the order of $1/k_\xi$. With the gradient method we can go beyond this limit and produce large phase gradients. The interaction dynamically leads to even larger gradients which break up at a critical value and produce non-linear excitations in the transversal spin degree of freedom. In Fig. 7.10 we show for a representative single shot at 24 s evolution time the transversal spin length and the phase spatially resolved (right panel). For comparison, we show one single shot for the polar state (left panel) as initial condition. In contrast to the polar state, the spin wave features non-linear excitations which are characterized by a dip in the spin length and a jump of the Larmor phase.

We find that for wavelengths that are initially small enough, many of these excitations are produced by the dynamics and they stay in the system even for evolution times beyond 40 s. Together with the Bogoliubov dispersion relation discussed in section 7.1.1 the excitations of the complex valued order parameter $F_\perp$ are suggestively similar to solitons [131]. However, the spin-1 system features more degrees of freedom and one has to find the limits of this comparison, e.g. , experimentally by measuring the properties of single excitations and comparing them to the expectations known for the one-component Bose gas.

In Fig. 7.11 we compare the two-dimensional histograms of the transversal spin for the polar state (lower panel in green box) and the spin wave (upper panel in red box) as initial conditions for the same q_{eff}, which is again adjusted such that $q \approx |nc_1|$. For the polar state, initially only having coherent state fluctuations around zero spin, we observe the already discussed ring structure which results from a nearly homogeneous spin length after 24 s evolution time. The initial histogram for the spin wave resembles this structure but features different correlations. Further, we find that already after short times ($\sim 500\,\text{ms}$) the system features all kinds of spin lengths resulting from defects in the transversal spin degree of freedom.

The corresponding spectra in Fig. 7.11 (upper panel in green box and lower panel in red box) show that the correlations can not be inferred from the histogram. Even though the histograms for the spin wave at 0 s and of the polar state at 24 s essentially feature the same structure, the spectra are qualitatively different. We find one single length scale, the wave length, dominating the spectra of the spin wave, whereas we have a broad range of momenta occupied for the polar state.

In a numerical study [132], we found that the defects can lead to new scaling phenomena not yet observed in the experiment. This type of preparation provides a starting point for studying such dynamics and, combined with the different readout schemes, allows for a detailed experimental examination of the internal structure of these defects.

Chapter 8

Observation of universal dynamics in a spinor Bose gas far from equilibrium

In the following chapter we are going to describe a series of experiments reporting on the first experimental observation of universal dynamics far from equilibrium [18]. We detail the experimental parameters and the method for extracting the angular orientation of the transversal spin from a measurement of a single spin projection. We give a definition of universality far from equilibrium and with that identify the scaling regime from the structure factor of the angular orientation. The experimental control allows us to directly verify the robustness of the results to changes in the initial condition. This chapter is based on [18], with some parts having substantial overlap, others being borrowed verbatim.

The experimental observation of scaling entails direct applications. First, we introduce a new experimental tool to classify systems far out of equilibrium. This may lead in the future to the classification into universality classes. It is conjectured that they may be not connected to universality classes already known [50] and can even be qualitatively different. We will associate universal dynamics far from equilibrium with the existence of a non-thermal fixed point. One system can feature multiple non-thermal fixed points, which comes from the fact that out of equilibrium new symmetries can dynamically emerge. Universal dynamics can give the means to identify that two systems feature the same type of dynamics. This would allow the implementation of quantum simulation in the system which is easier to control.

A different aspect is that universal dynamics is a scenario that quantum systems can feature on the way towards thermal equilibrium. The general idea of that scenario is schematically depicted in Fig. 8.1a. A system is initialized far out of equilibrium and eventually may reach some (thermal) equilibrium or quasi-stationary state. Transiently, it features universal dynamics indicating the emergence of a non-thermal fixed point. In this regime the dynamics is critically slowed down as, e.g. , the typical length scale shows a power law dependence on time. Furthermore, the dynamics are insensitive to details of the initial condition, which is indicated by the merging trajectories.

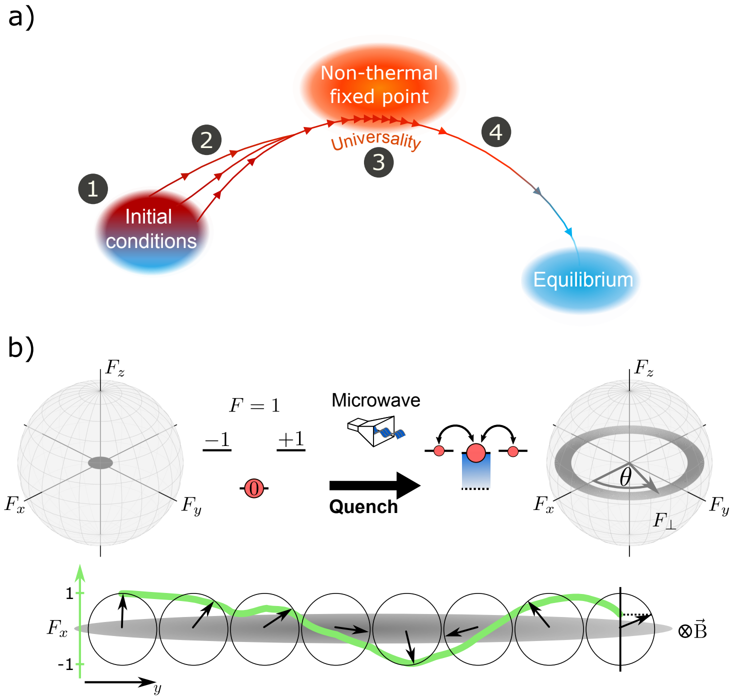

Figure 8.1: **The scenario of universal dynamics and the experimental procedure**. a) A quantum system with a far-from-equilibrium initial condition evolves dynamically in time. High occupation numbers can lead to universal dynamics independent of the initial condition (merging of lines). This indicates the emergence of a non-thermal fixed point. The dynamics is critically slowed down (power law dependence on time) before the system eventually reaches a (thermal) equilibrium or quasi-stationary state. Experimentally the system is probed at different stages of this evolution (1-4). b) We prepare a polar condensate in $(1, 0)$ having coherent state fluctuations in the $F_x - F_y$-plane (left spin sphere). Microwave dressing tunes spin-changing collisions in resonance leading to excitations in the transversal spin plane (right sphere). This leads to spatial structures of the angular orientation of the transversal spin. Figure taken and adapted from [18].

8.1 Experimental setup

In Fig. 8.1b we show the general scheme of the experiment. We prepare the initial condition, here exemplarily the polar state. It is represented in the $F_x - F_y - F_z$ spin-sphere by a disc indicating the coherent state fluctuations in the $F_x - F_y$-plane. We quench the detuning q_{eff} by applying microwave dressing which allows for spin-changing collisions populating the side modes. For short times, this leads to excitations in the transversal spin plane and eventually to an elongated spin with well defined spin length and highly excited phase degree of freedom (ring in right sphere). In each experimental realization we acquire a spatially resolved snapshot of one transversal spin projection (schematic green line). After many experimental runs we analyse the data in terms of correlation functions. In this way we track the dynamics over different evolution times.

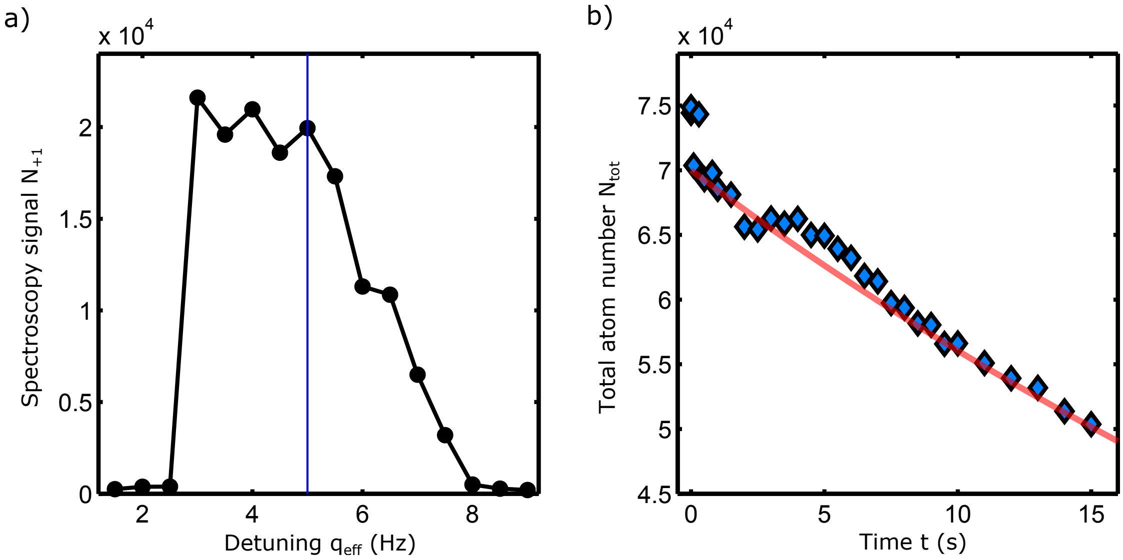

Figure 8.2: **Spectroscopy and total atom number.** a) Exemplary spin-changing collision spectroscopy for the measurement settings employed. We adjust the detuning to $q_{\text{eff}} = 5\,\text{Hz}$ (blue vertical line) after the quench. This ensures the system to be in the easy-plane ferromagnetic phase for all evolution times. b) Total atom number (blue diamonds) as a function of evolution time. The red line indicates an exponential decay with a $1/e$ time of 45 s.

Let us give a short overview of the experimental parameters used in this chapter. We initially prepare an elongated condensate of $\sim$ 70.000 atoms which results in an interaction energy $n|c_1| \approx 2\,\text{Hz}$. We use the trapping configuration with $U_{\text{WG}} = -2.9\,\text{V}$ leading to $(\omega_\parallel, \omega_\perp) \approx 2\pi \times (2.1, 220)\,\text{Hz}$. In Fig. 8.2a we show the spectroscopy measurement for the employed settings. For dressing we use off-resonant microwave radiation with resonant Rabi frequency $\Omega \approx 2\pi \times 5.3\,\text{kHz}$ and detuning $\delta \approx 2\pi \times 137\,\text{kHz}$; it is blue detuned with respect to the $(1,0) \leftrightarrow (2,0)$ transition. The vertical line marks the used value of $q_{\text{eff}} = 5\,\text{Hz}$ which is chosen such that $q \approx |nc_1|$. We quench the system into the easy-plane ferromagnetic phase and let it evolve up to an evolution time t_{evo}.

We probe the system for evolution times up to 15 s. The long evolution times unavoidably lead to atom loss which we quantify in Fig. 8.2b. With an exponential fit (red line) we estimate the 1/e-lifetime of the atom number to be approximate 45 s such that after 10 s about 20% of the atoms are lost from the trap. In principle this also leads to a shift of the phase boundary between polar and easy-plane phase where the shift is proportional to $\propto N^{2/5}$ within the Tomas-Fermi approximation [115]. The adjustment to $q \approx n|c_1|$ ensures that the system stays in the easy-plane ferromagnetic phase for all evolution times. The atom number would have to change by a factor of ~ 4 before the system leaves the easy-plane ferromagnetic phase.

After the quench we find unstable momentum modes as described in the previous chapter. We characterize them by looking at the structure factor of the x-projection of the spin. In Fig. 8.3 we see that the structure factor is initially flat (black line) but a fast-build up by more than two orders of magnitude of populations is found in

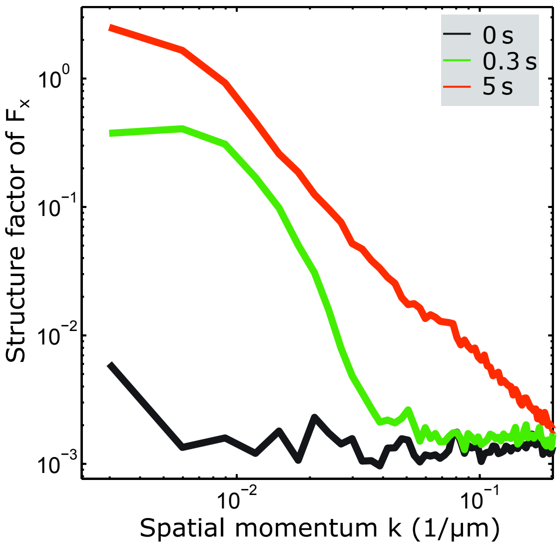

Figure 8.3: **Transversal spin structure factor.** The transversal spin structure factor for three different evolution times versus the spatial momentum in a double-logarithmic plot. Initially the spectrum is flat. We find an exponentially fast occupation of unstable momentum modes. Redistribution leads to an occupation over a broad range of momenta even for evolution times beyond 5 s. Figure taken and adapted from [18].

the first 500 ms. The growth features a most unstable mode slightly above $k = 0$ indicating the right choice of parameters ($q \approx n|c_1|$; cf. Fig. 7.3). For long evolution times we find redistribution of the excitations among a broad range of momenta. This redistribution is also visible in the obtained real-space snapshots. A representative realization in each regime of the evolution is shown in Fig. 8.4.

8.2 Inferring the spin orientation

For this study we employ standard absorption imaging in the $F = 1$ manifold. A $\pi/2$ spin rotation maps the observable F_x onto the spatially resolved atomic densities i.e.

$$F_x(y) = \frac{N_{+1}(y) - N_{-1}(y)}{N_{+1}(y) + N_0(y) + N_{-1}(y)} \,. \tag{8.1}$$

We probe the system at different evolution times and acquire $\sim 80-160$ experimental realizations for each time [1]. Exemplary atomic densities (grey shading) together with corresponding spin profiles (green lines) in the different regimes 1-4 (see Fig. 8.1) are shown in Fig. 8.4. From all experimental realizations and all spatial points[2] we infer the ensemble averaged probability distribution of the spin projection for a given time (green histograms). We initially (1) find a narrow Gaussian distribution corresponding to the prepared coherent spin state. The instability (2) produces

---

[1] We concentrated on some evolution times (integer times) for obtaining higher statistics.

[2] To account for the imaging resolution we bin three adjacent pixels.

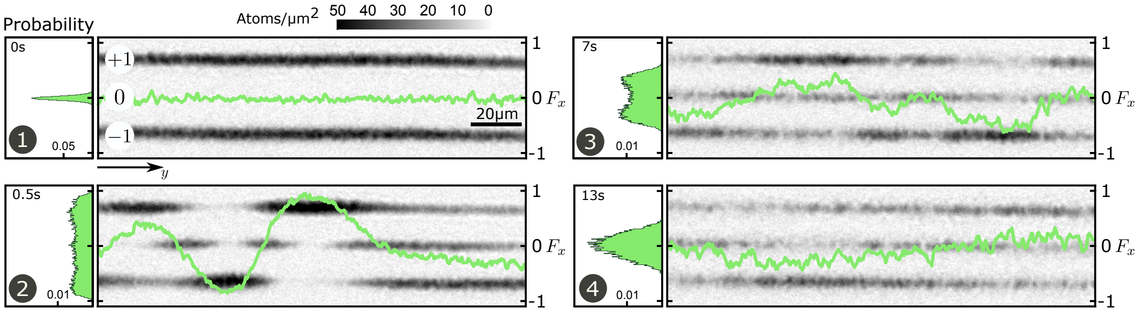

Figure 8.4: **Characterization of transversal spin degree of freedom.** After a $\pi/2$ rf rotation we detect the three atomic densities $(1, 0, \pm 1)$ (grey shading) and infer the transversal spin projection $F_x(y)$ spatially resolved (green lines). To characterize the dynamics we probe the system for different evolution times. Here, we show four different times associated with the regimes in Fig. 8.1a. The histograms (green) show the distribution of the spin projection. We take into account ~ 160 realizations and all space points. Figure taken and adapted from [18].

all kinds of spin lengths featuring a spatial wave-like structure and a broadened histogram. For regime (3) we find a double-peaked histogram resulting from a spatially modulated signal on all length scales. A broad Gaussian peak around zero spin is found for long times (4).

In the mexican hat picture this can be understood as preparing a wave packet at the unstable fixed point. The negative curvature gives access to instabilities leading to a spreading of the wave towards the bottom of the potential; it "rolls" down from the hill to the valley. Finally, it settles on the rim with a well defined length and large phase fluctuations since phase excitations do not cost any energy. This aspect is further discussed and differently visualized in the next chapter employing a different readout.

We associate the double-peaked histogram with a transversal spin which has a length $\langle |F_\perp| \rangle$ with small fluctuations σ^2 and is (in the ensemble average) randomly orientated. An exemplary distribution generated by hand is shown in the left panel of Fig. 8.5. The projection (black dots right panel) resembles the double-peaked structure found in the experiment. A fit (red line) allows us to infer the spin length and its fluctuations. For this we use a probability distribution of the form $p(F_x) \propto \sqrt{1/\left(F_x/\langle |F_\perp| \rangle\right)^2}$ and convolute it with a Gaussian with width σ. In this example we plot for illustration the function with the spin length and the width used to generate the two-dimensional distribution.

In Fig. 8.6a we show the histograms and the corresponding fits for all experimentally measured evolution times. In all cases the fit resembles the experimental data. We find a double-peaked structure for times between 1 s and 10 s. The extracted spin length (Fig. 8.6b) shows a decay and after ~ 12 s cannot be extracted reliably any more. The fluctuations of the length show an increase for short times and settle around a constant value. For large times the Gaussian peak shows larger fluctuations than the initial condition. We associate the decay of the spin length with reduced

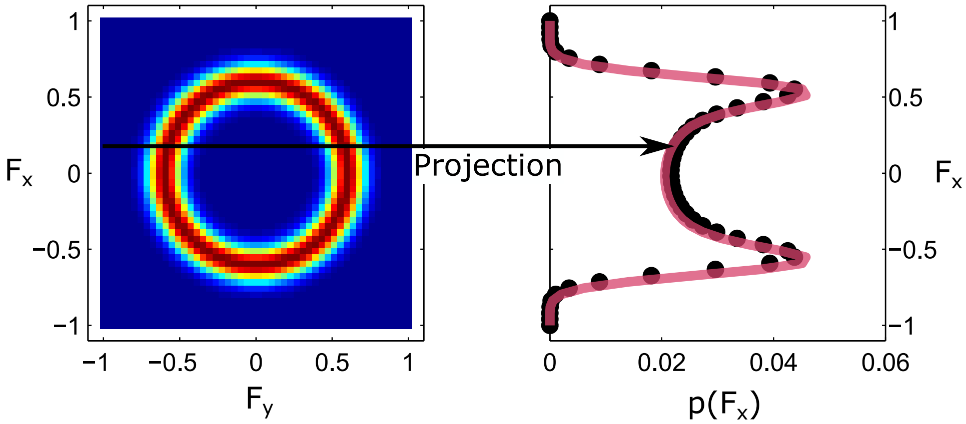

Figure 8.5: **Inferring the spin length from one projection.** For a circular shaped distribution (colour-coded in left panel) in the transversal spin plane the measurement of one projection results in a double-peaked structure of the probability distribution of F_x (black markers right panel). The finite width of the peaks comes from the fluctuations in radial direction. The length $\langle |F_\perp| \rangle$ and its fluctuations σ^2 can still be estimated from a fit (red line) with a probability distribution $p(F_x) \propto \sqrt{1/\left(F_x/\langle |F_\perp| \rangle\right)^2}$ convoluted with a Gaussian with width σ.

coherence properties of the spinor BEC due to heating of the atomic densities after long evolution times.

The observation of reduced spin length fluctuations and highly excited phase degree of freedom lead us to the conclusion that the angular orientation θ becomes the relevant degree of freedom during the dynamics. Assuming a spatially homogeneous spin length we extract $\theta(y,t)$ from the spin profiles and the employed fit as

$$\theta(y,t) = \arcsin(F_x(y)/\langle |F_\perp| \rangle)\,. \tag{8.2}$$

Because of the finite spin length fluctuations, the measured spin projection $|F_x(y)|$ can become locally larger than $\langle |F_\perp| \rangle$ which leads to $|F_x(y)|/\langle |F_\perp| \rangle > 1$. As the domain of $\arcsin(x)$ is $(-1,1)$, we use the maximal amplitude of F_x in the single realization in case it is larger than $\langle |F_\perp| \rangle - \sigma$.

The time evolution of the fluctuations of the spin orientation is described in terms of correlation functions of the scalar field $\theta(y,t)$. We evaluate the fluctuations calculating the two-point correlation function $C(y,y';t) = \langle \theta(y,t)\theta(y',t) \rangle$ which is the connected correlator as we find $\langle \theta(y,t) \rangle \approx 0$. A momentum-resolved picture of the dynamics allows us to distinguish the role of different length scales. Hence we evaluate the structure factor, which is the Fourier transform of $C(y,y';t)$

$$f_\theta(k,t) = \iint \mathrm{d}y\,\mathrm{d}\bar{y}\, C(y, y+\bar{y}; t)\, \exp(-i\,2\pi k \bar{y})\,. \tag{8.3}$$

The Fourier transform is performed with respect to the relative coordinate $\bar{y} = y' - y$ and averaged over y.

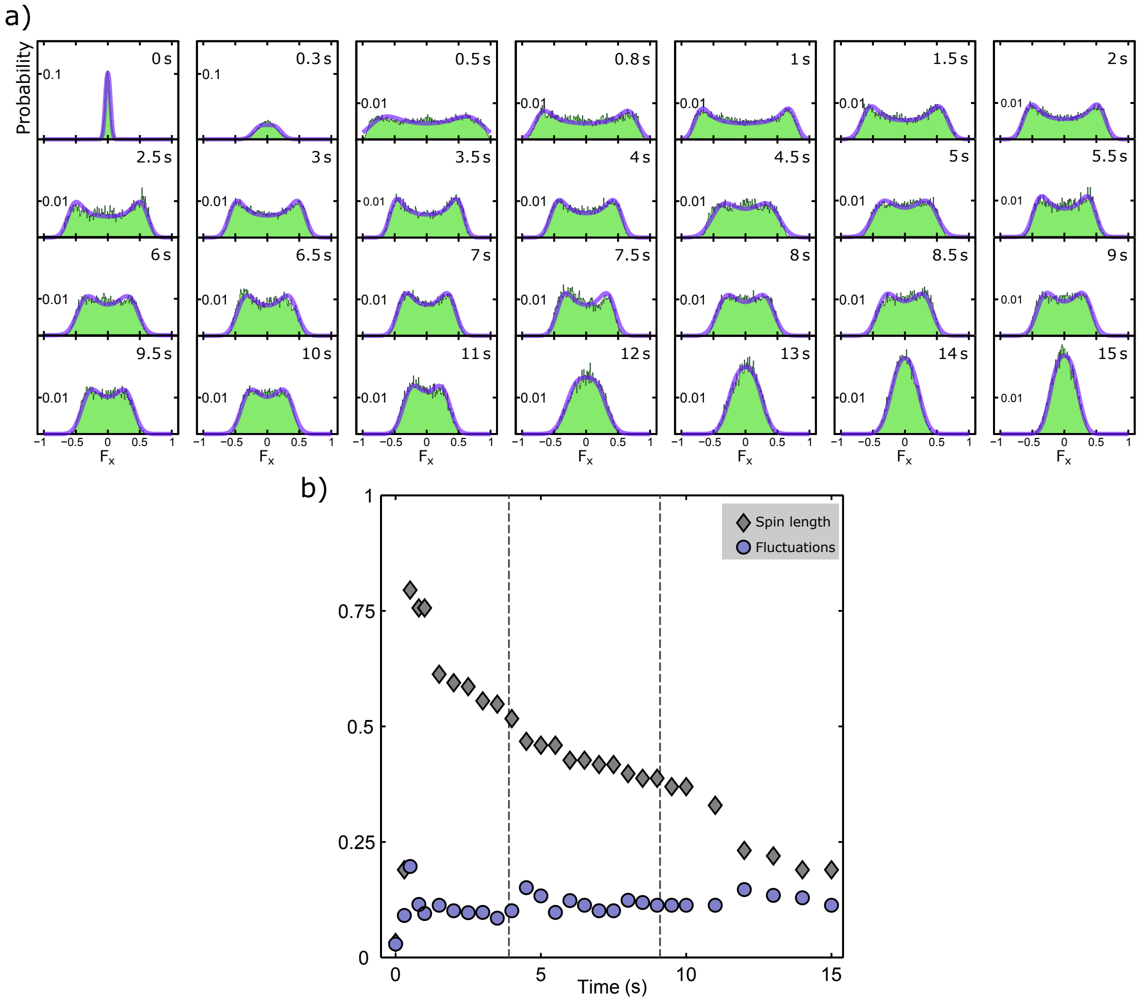

Figure 8.6: **Spin distributions for all evolution times.** a) Transversal spin distributions for all spatial points and ∼ 80−160 experimental realizations for different evolution times. The initially found narrow Gaussian distribution corresponds to the prepared coherent spin state. The double-peaked distribution within the interval of 2 s to 10 s results from excitations developing in the transversal spin. For long evolution times, $t > 12$ s we again find a Gaussian distribution which is, however, much broader than the initial condition. b) We extract the spin length and its rms fluctuation as a function of evolution time by a fit and find a slow decay of the spin length and nearly constant rms fluctuations. Figure taken and adapted from [18].

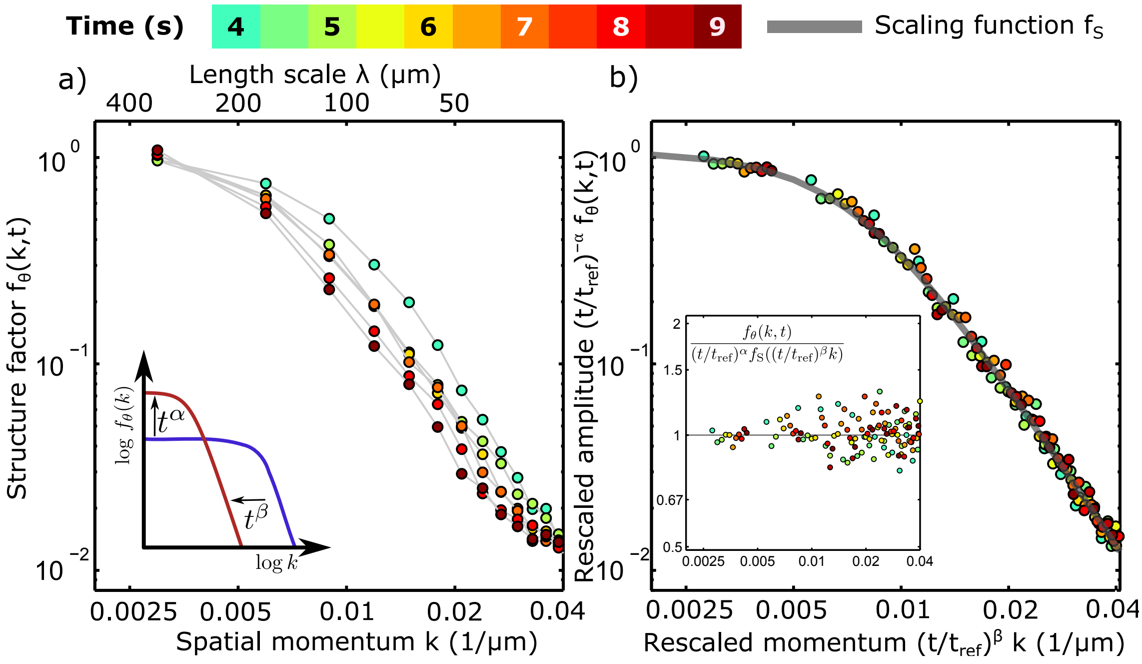

Figure 8.7: **Rescaling in time and space.** a) The angular structure factor $f_\theta(k,t)$ for different times (colour-coded circles) in the scaling regime between 4 s and 9 s as a function of the spatial momentum $k = 1/\lambda$ (only the infrared momenta are shown; see Appendix B for all momenta) . Universal dynamics at a non-thermal fixed point is indicated by a constant functional form and a shift to lower momenta with t^β and higher amplitudes with t^α (see inset). b) Rescaling with $t_{\mathrm{ref}} = 4.5\,\mathrm{s}$ according to Eq. (8.4) with $\alpha = 0.33$ and $\beta = 0.54$ leads to a collapse of the data onto a universal function. The grey line indicates a fit with the empiric scaling function (see main text) with $\zeta \approx 2.6$ and $k_s \approx 1/133\,\mu\mathrm{m}^{-1}$. The inset shows the rescaled data divided by the fit. The symmetric scatter reveals the quality of the rescaling. Figure taken and adapted from [18].

8.3 Observation of scaling

Far from equilibrium, the structure factor f_θ is in general a time-evolving quantity depending on the spatial momentum k. If the system is isolated, the unitary dynamics is in principle fully determined by the system parameters and the initial condition. However, at a non-thermal fixed point the dynamics of some macroscopic observables can get independent of details and one finds universal dynamics according to the scaling hypothesis

$$f_\theta(k,t) = t^\alpha f_{\mathrm{S}}\big(t^\beta k\big)\,, \tag{8.4}$$

with universal scaling exponents α, β and scaling function f_S. Instead of separately depending on time and momentum, the structure factor becomes a function of the product $t^\beta k$ only.

Fig. 8.7a shows f_θ in the scaling regime between 4 s and 9 s (times colour-coded) on a double-logarithmic scale. We observe a characteristic shift of the typical length scale (bending point) towards lower momenta and an increase of the amplitude. This behaviour, schematically shown in the inset, is expected at a non-thermal fixed point. After rescaling of the different times according to Eq. (8.4) with the amplitude scaling exponent

$$\alpha = 0.33 \pm 0.08$$

and the momentum scaling exponent

$$\beta = 0.54 \pm 0.06$$

we find a collapse of the data onto a universal curve; for this we plot the rescaled distribution $t^{-\alpha} f_\theta$ as a function of $t^\beta k$. Fig. 8.7b shows the same data points as in Fig. 8.7a with times normalized to the reference time $t_{\mathrm{ref}} = 4.5\,\mathrm{s}$. We fit the rescaled data to an empirical scaling function $f_S(k) \propto 1/\left(1 + (k/k_s)^\zeta\right)$ [96] and find $\zeta \approx 2.6$ and $k_s \approx 1/133\,\mu\mathrm{m}^{-1}$. Usually scaling solutions are pure power laws having no characteristic length scale. However, in systems with finite size at least one length scale is always present. We see that we can reduce the non-equilibrium dynamics of certain correlation functions in the scaling regime to a time-independent, so-called fixed point distribution $f_S(k)$ and associated scaling exponents. It is this type of rescaling which signals universal behaviour far out of equilibrium.

For finding the optimal values of α and β the summed squared relative distances between all data points are minimized. We interpolate the rescaled results with cubic splines to obtain a common k-grid for all evolution times. The 1 standard deviation (1 s.d.) error is estimated by employing a jackknife resampling analysis [133]. If the scaling function is just a power law, the rescaling analysis cannot differentiate between α and β. For the experimental data the plateau regime is small and thus the rescaling analysis is much less constraining on α than on β. Thus we expect the systematic uncertainty for α to be larger. The error on the structure factor is also estimated by employing jackknife resampling and is on the order or below the size of the data points in Fig. 8.7.

The positive sign of β indicates redistribution of excitations towards the infrared. We find a conserved quantity ($\alpha \approx \beta$) and thus we interpret this redistribution as a transport phenomenon. It is the defining feature of a non-thermal fixed point [134, 135] and is in contrast to the transport into the ultraviolet in turbulent cascades [17]. In Appendix B we show the same data as in Fig. 8.7 but for the whole momentum range and find no rescaling for momenta larger than ~ $0.04\,\mu\mathrm{m}$. This is in accordance with the theoretical expectation that this type of transport is an infrared phenomenon [68]. In principle one can find different dynamics, e.g. , a direct cascade also featuring rescaling in the ultraviolet [132].

Characterization of the dynamics allows for comparison with analytical as well as numerical expectations. If the concept of universality proves to be successful it may allow for the definition of universality classes far from equilibrium. Numerical simulations of the experimental system prove to be a hard, if not an unfeasible task. The most promising ansatz are semi-classical methods based on the truncated Wigner approximation (TWA) [88]. These, however, feature cut-off dependencies when implemented with the experimentally employed cigar shaped trap geometry. This is due to the rather low atom number compared to the number of spatial modes needed for a description of the dynamics. We used a simplified simulation with a strict one-dimensional homogenous setup and find indeed universal dynamics [132], however, with different universal exponents and qualitatively different characteristics. The system features non-linear excitations in the spin degree of freedom, similar to solitonic excitations in a one-component Bose gas. This leads to a different universal phenomenon which, together with the experimental findings [18, 19], sheds new light on the concept of universality classes far from equilibrium as it was not expected to find universal dynamics in one spatial dimension.

We therefore want to compare to expectations for systems which may lie in the conjectured universality classes defined by the scaling function f_S and $\alpha = d\beta$ for given spatial dimension d. For the already discussed $O(N)$-model (see section 3.6) a universal value of $\beta \approx 0.5$ has been predicted. It was found to be insensitive to the spatial dimension for $d \geq 2$ [68, 136]. A recent numerical study revealed that the dynamics describe the self-similar transport of excitations of the relative phases between the components to lower wave numbers [97]. The scaling function f_S is known to depend on dimensionality [136] and has not yet been theoretically estimated for $d = 1$. For $d > 1$ one finds $\zeta = d + 1$ for the power law exponent. Our setup may be interpreted as the first realization of an effective $O(N)$-model examining the phenomenon of non-thermal fixed points in a quasi one-dimensional situation. The effective N realized in the experiment may be studied with the help of unequal-time correlation functions [137].

Assuming that universality classes, for a given spatial dimension d, are defined by the scaling function f_S and $\alpha = d\beta$, the presented experimental observation may be seen as a quantum simulation of universal dynamics far from equilibrium. The high degree of control allows for testing the conjectured insensitivity. The simulation is verified by the comparison of the scaling exponents. This opens the way for a precise characterization and quantum computations in this regime hard to access theoretically.

8.4 Identifying the scaling regime

Up to now we did not further specify how we identified the scaling regime being between 4 s and 9 s. To do so, we fit the scaling function f_S to the structure factor f_θ for each time individually and extract the power-law exponent ζ. In Fig. 8.8a we show the correlation function and the fit for 6 s of evolution time. A necessary condition for being in the scaling regime is the emergence of a scaling function with, in our case, a constant value of ζ. Plotting the fit results versus the evolution time (Fig. 8.8b) we find a settling of ζ around ≈ 2.6 after 4 s, which indicates the beginning of the scaling regime.

As a consistency check we analyze the typical length scale $1/k_s$. For reliably extracting the typical length scale we fix the exponent ζ to 2.6 and refit the data. The obtained results are shown in Fig. 8.8c as a function of evolution time. Up to ~ 9 s we find a growing length scale which saturates around 200 μm for longer times. In the scaling regime (grey shaded area) one expects the typical length scale to change as a function of evolution time as $\propto t^\beta$. We find reasonable agreement with the result obtained from the rescaling analysis; a power law $t^{0.54}$ is indicated by the grey solid line in Fig. 8.8c.

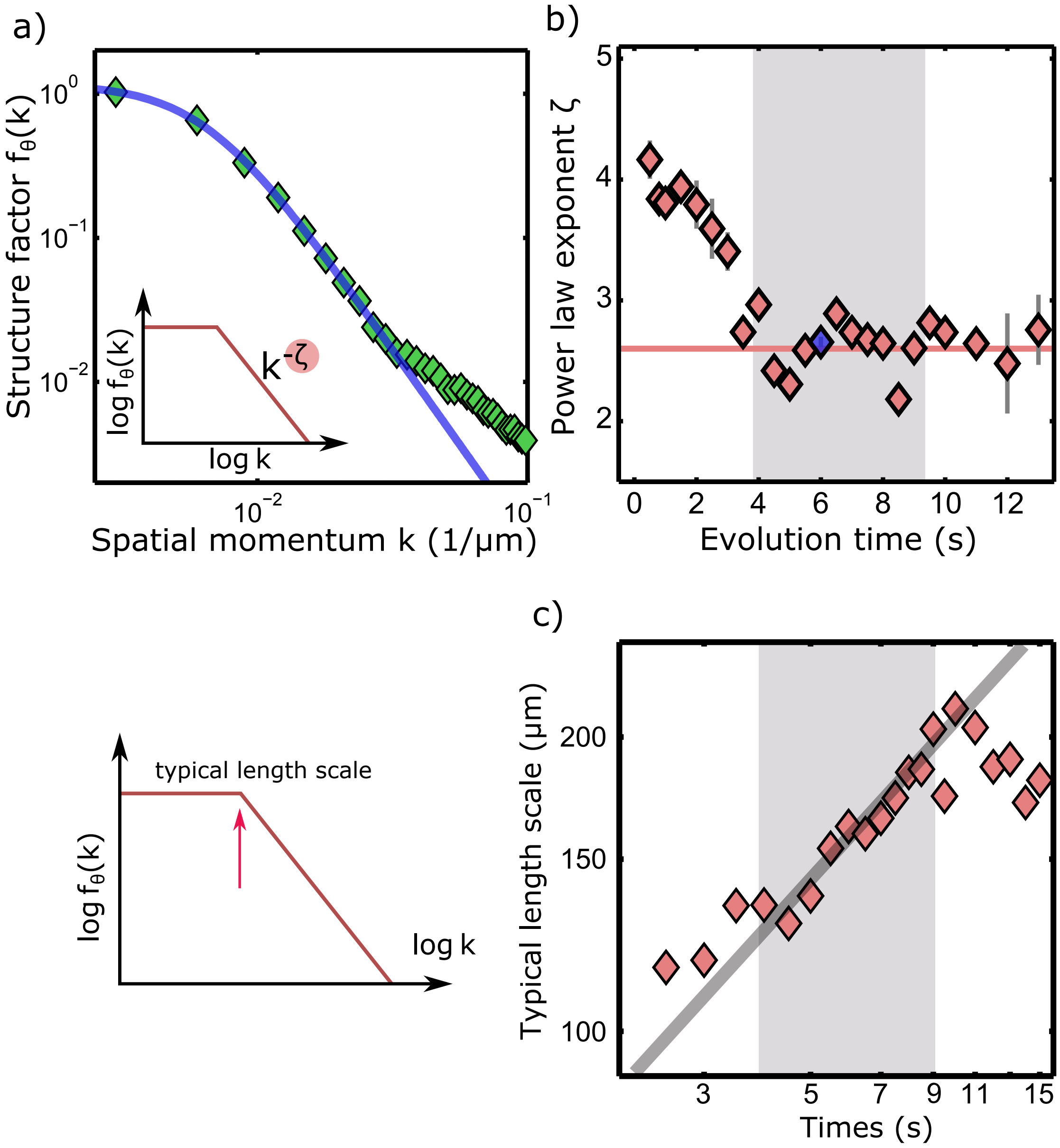

Figure 8.8: **Extraction of the scaling function.** a) Exemplary structure factor $f_\theta(k,t)$ for 6 s evolution time (green diamonds). We fit the scaling function $f_S(k) \propto 1/\left(1+(k/k_s)^\zeta\right)$ (blue line) and extract with that the power-law exponent ζ in the infrared up to momenta $\sim 0.03\,\mu\mathrm{m}^{-1}$. b) We plot the exponent ζ as a function of evolution time and find a settling to a constant value of $\zeta \approx 2.6$. Blue diamond indicates the result from a). The beginning of the scaling regime (grey shading) is defined by the emergence of a constant value of ζ. The error bar is 1 s.d. of the employed fit. c) Fixing the exponent ζ to 2.6 for refitting the data we extract the length scale $1/k_s$ as a function of time. The grey line indicates the expected behaviour $\propto t^\beta$ with $\beta = 0.54$. Panel b) is taken and adapted from [18].

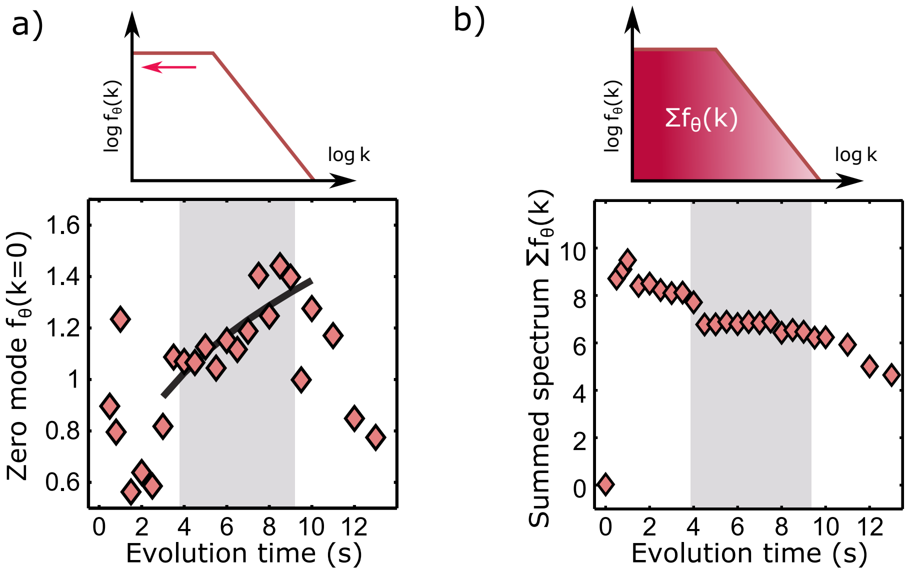

Figure 8.9: **Identification of the scaling regime.** a) Occupation of zero mode ($k = 0$) as a function of evolution time which is not visible in Fig. 8.7. We find an increase of the occupation between 4 s and 9 s. The fast decrease after 9 s indicates the end of the scaling regime. The evolution is found to be consistent with the extracted amplitude scaling exponent $\alpha = 0.33$ (black line). b) Summed structure factor for all evolution times. The scaling phenomenon is explained by the emergence of a conserved quantity and we indeed find an approximate conservation of $\sum_k f_\theta(k,t)$ in the scaling regime. Figure taken and adapted from [18].

Following Eq. (8.4) we expect that $f_\theta(k = 0, t) \propto t^\alpha$, i.e. a growth of the zero mode occupation in time. Between 4 s and 9 s we find this behaviour consistent with $\alpha = 0.33$ found from the rescaling analysis of the whole function (see Fig. 8.9a). The corresponding power law growth is indicated by the black solid line. As explained, we expect the emergence of a conserved quantity at the non-thermal fixed point. In our case we find $\sum_k f_\theta(k,t)$, plotted in Fig. 8.9b, to be the conserved quantity. In accordance with the zero mode we also find a decrease of the summed spectrum after 9 s.

The phenomenon of scaling at a non-thermal fixed point is associated with the transport of a conserved quantity implying $\alpha = \beta$. In Fig. 8.9b we plot the summed spectrum $\sum_k f_\theta(k,t)$. In the scaling regime we find an approximate conservation, the found values of α and β differ within the statistical error bar. A possible source of error is the inference of the angular orientation. For the inference we assume that the spin length is constant over the cloud and all experimental realizations. We know, however, that the spin length has finite fluctuations.

8.5 Robustness – changing the initial conditions

The observed phenomena do not rely on fine tuning of parameters or initial conditions. It is this robustness that gives the large potential of universal dynamics with regard

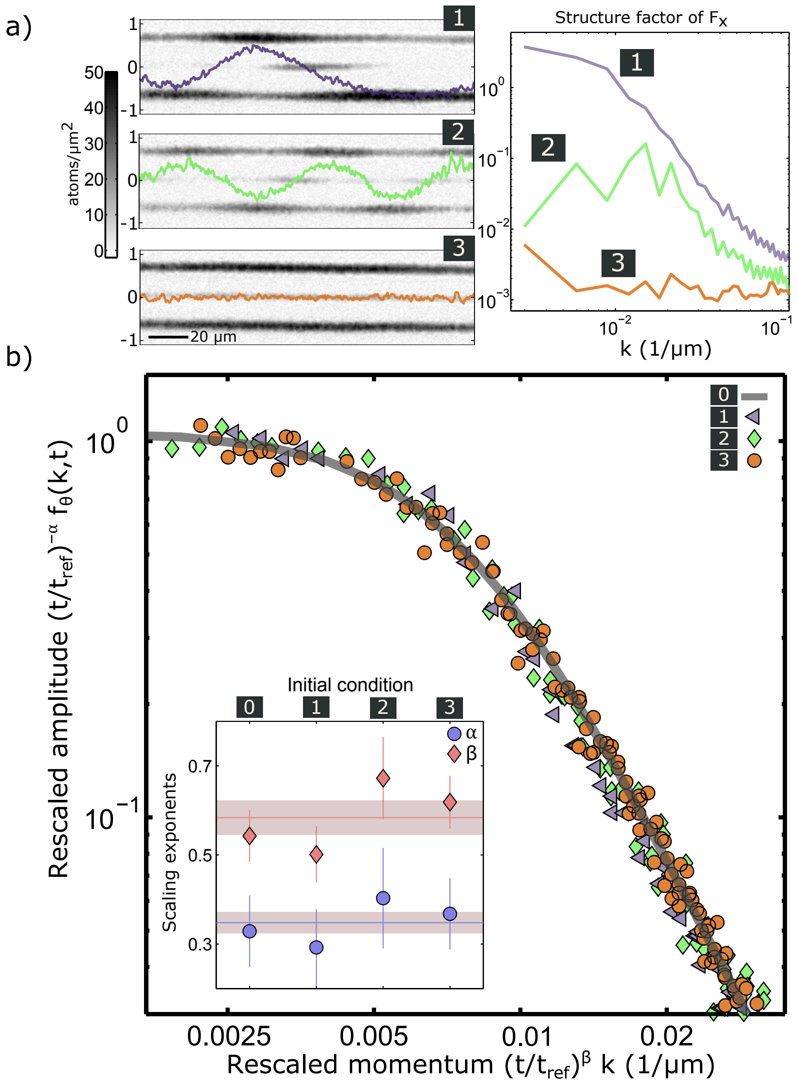

Figure 8.10: **Robustness of universal dynamics at a non-thermal fixed point.** a) We prepare three different initial conditions 1-3 (see main text for details of the preparation). 1 and 2 feature spatial structure on different length scales. Left panel: Exemplary experimental realization of the three densities $(1; 0, \pm 1)$ after $\pi/2$ rf-rotation and the inferred transversal spin $F_x(y)$ (coloured lines). Right panel: Structure factor of $F_x(y)$ showing different momentum dependences. b) Structure factor of angular orientation $f_\theta(k,t)$ for the three initial conditions 1-3 (triangles, diamonds and circles) and the fit of the polar case (grey line). For rescaling we use the mean of the results from the four initial conditions (vertical lines inset). The inset shows the result of the rescaling routine. Figure taken and adapted from [18].

to quantum simulation. In this section we show how we can probe this feature experimentally employing the high control over the system.

In Fig. 8.10a we show the atomic densities after a $\pi/2$ rf rotation and the structure factor of the transversal spin F_x for three different initial conditions labelled by 1-3. Initial condition 3 shows no spatial structure but already has a small population in the side modes $(1, \pm 1)$ ($\approx 10\%$) which is created by a short rf-pulse. This also leads to a flat curve in momentum space (cf. black line in Fig. 8.3). We create initial conditions with spatial modulations in two different ways. For initial condition 1 we first set the control parameter to $q \approx |nc_1| + 1\,\mathrm{Hz}$. After 500 ms we quench q_{eff} to its final value $q \approx |nc_1|$. From Bogoliubov theory we know that the first quench gives rise to a slightly smaller most unstable momentum mode which leads to higher occupations of smaller modes. The external control allows us to produce initial condition 2 similar to the spin waves. However, here we employ a $\pi/5$ rf rotation of the polar state to populate the side modes. We apply a magnetic field gradient of $\approx 0.2\,\mu\mathrm{G}/\mu\mathrm{m}$ for 100 ms before a second rf rotation is employed. The inhomogeneous magnetic field leads to a spin wave with wavelength $\lambda \approx 80\,\mu\mathrm{m}$ and a finite spin length which is not expected starting from a rotated polar state. However, the spinor phase (phase of $m_F = 0$) evolves with the second-order Zeeman shift with $q = 56\,\mathrm{Hz}$ leading to a spin in the transversal plane.

In Appendix B we show the time evolution in the scaling regime for all three initial conditions. We find universal dynamics for all of them with comparable exponents (see Fig. 8.10b inset). In principle, universal dynamics allows the comparison of dynamical phenomena on vastly different scales. To obtain the compatibility of different systems with, e.g. , different length scales, one has to introduce an overall time-independent scaling factor; this introduces no loss of generality [138]. Fig. 8.10b shows data for all three initial conditions rescaled with the same scaling exponents, which are the means over all initial conditions (vertical lines inset). With the additional overall scaling factor we find that all initial conditions collapse to the same universal curve represented by the fit of the scaling function to the data from the polar state. This is the experimental manifestation of the robustness of the employed dynamics.

8.6 Different experiments on universal dynamics

The experimental observation of universal dynamics has also been accomplished recently in the group of Jörg Schmiedmayer in Vienna [19]. For their studies they employ a one-dimensional single component BEC of ^{87}Rb confined with magnetic potentials on an atomchip. They quench a not yet condensed gas by a sudden removal of the high energy part of the thermal distribution and thus, implement a cooling quench. In the experiments the momentum distribution is directly measured by a time-of-flight technique. They observe in an intermediate regime of the time evolution universal dynamics of the momentum distribution and find exponents of $\alpha \approx \beta \approx 0.1$. The distinct values of the scaling exponents indicate the existence of different universality classes far from equilibrium. Further the observation is qualitatively different in a sense that they observe solitonic defects.

Prior to these results, long term dynamics of ferromagnetic BECs have been studied in a two-dimensional setting in the group of Dan Stamper-Kurn in Berkeley. After employing a similar quench as shown in this thesis they observed polar-core vortices [26]. For long evolution times the system featured coarsening of transversal spin domains but the system size was not large enough to resolve universal dynamics reliably for long evolution times [125].

In the group of Chandra Raman in Atlanta, they employed quenches for a sodium BEC with antiferromagnetic interactions and also expected to see coarsening dynamics [139, 140]. However, as revealed by Fujimoto [141], the quench was not "deep" enough and they did not observe the right order parameter.

This variety of experimental approaches and systems highlights the future possibilities for studying universal dynamics for different universality classes. Especially two-dimensional systems may be a fruitful platform for studying defect-driven dynamics since different kinds of topological stable excitations are possible [69, 129, 142].

Chapter 9

Towards Bose condensation far from equilibrium

In this chapter, we present a combination of an optimized experimental setting and a new view on the observed universal dynamics. First, we show that the reduction of the trapping frequencies of the one-dimensional trap leads to spin coherence time up to 50 s. Second, we use these long coherence times together with the new spin readout to study the universal dynamics of the complex valued transversal spin field $F_\perp$. Its correspondence with a one-component Bose gas may allow to simulate Bose condensation far from equilibrium with the employed spin-1 system.

9.1 Enhanced coherence times

The ground state in the easy-plane ferromagnetic phase is a spin in the transversal plane. However, we found in the preceding chapter that the transversal spin length decays for long evolution times following a quench to $q \approx |nc_1|$. Following [124] one can deduce that the length of the ground state transversal spin is temperature dependent and that the easy-plane ferromagnetic phase is absent for too high temperatures. There are two possible sources of a non-zero spin temperature for long evolution times. First, by the quench we inject energy into the system which is in our case on the order of $n|c_1| \approx 2\,\mathrm{Hz}$. Assuming a critical density condensation temperature of 50 nK, a lower bound on the critical temperature for a vanishing easy-plane ferromagnetic phase would be $\sim 5\,\mathrm{nK}$ corresponding to $\sim 100\,\mathrm{Hz}$ which is much larger than the quench energy[1]. Thus it cannot explain the loss of coherence in the experiment. Secondly, there is heating of the atomic densities due to off-resonant scattering of photons from the trapping light. Looking at the atomic densities for long times, we find non-negligible thermal parts in accordance with the anticipated heating. Motivated by this we reduce the light power of the trapping potential leading to less scattering events and lower trapping frequencies. Here and in the next chapter, we use a laser power corresponding to trapping frequencies of $(\omega_\parallel, \omega_\perp) \approx 2\pi \times (1.6, 167)\,\mathrm{Hz}$.

---

[1] important number: 20 Hz/nK

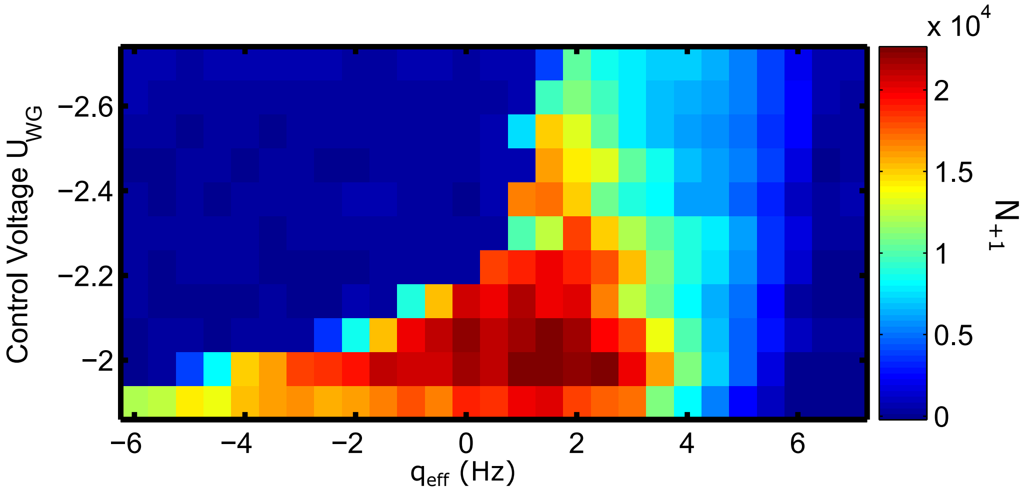

Figure 9.1: **Influence of trapping potential on spin-changing collisions.** Spin-changing collision spectroscopy for different waveguide control voltages. The side mode population N_{+1} is colour-coded. We find a constant value for the right edge of the spectroscopy. The left edge is shifting with decreasing laser power to lower values, giving access to dynamics deep in the easy-axis ferromagnet regime.

Change of spectroscopic measurement

We find that the intensity of the trapping light has a significant impact on the spin-changing collision spectroscopy signal. Increasing the light intensity decreases the range of negative q's (left edge of the spectroscopic measurement) where we observe dynamics. In Fig. 9.1 we plot the spectroscopic measurement for different waveguide powers. We find a constant value for the right edge of the spectroscopy. The left edge is shifting with decreasing laser power to lower values, giving access to q_{eff} deep in the easy-axis ferromagnet regime. In chapter 7, we already made use of this fact to characterize the Bogoliubov excitations.

Transversal spin lifetime

A second result of varying the trapping potential is an increase of the transversal spin life time. For studying the life time of the transversal spin we initialize the polar state and quench the detuning to $q \approx |nc_1|$. In Fig. 9.2 we show the histograms of the transversal spin degree of freedom. We find a spin length $|F_\perp| \sim 0.7$ up to times $\approx 40\,\text{s}$ (see Fig. 9.3) which is much longer than compared to the previous results. The enhanced coherence times are directly correlated with the reduced intensities. Fitting an exponential decay to the transversal spin length $|F_\perp|$ we find a life time of $\approx 60\,\text{s}$ (see also [143] for detailed study).

To visualize the increased life time of the spin length we evaluate the spin distribution functions. In contrast to the histograms shown earlier, we subtract from every experimental realization the phase at the centre of the sample. This results in histograms being centred around one point such that the extension of the phase along the circle in a single realization can be directly read off. We observe that the extension gets smaller as a function of time which is explained by the phase

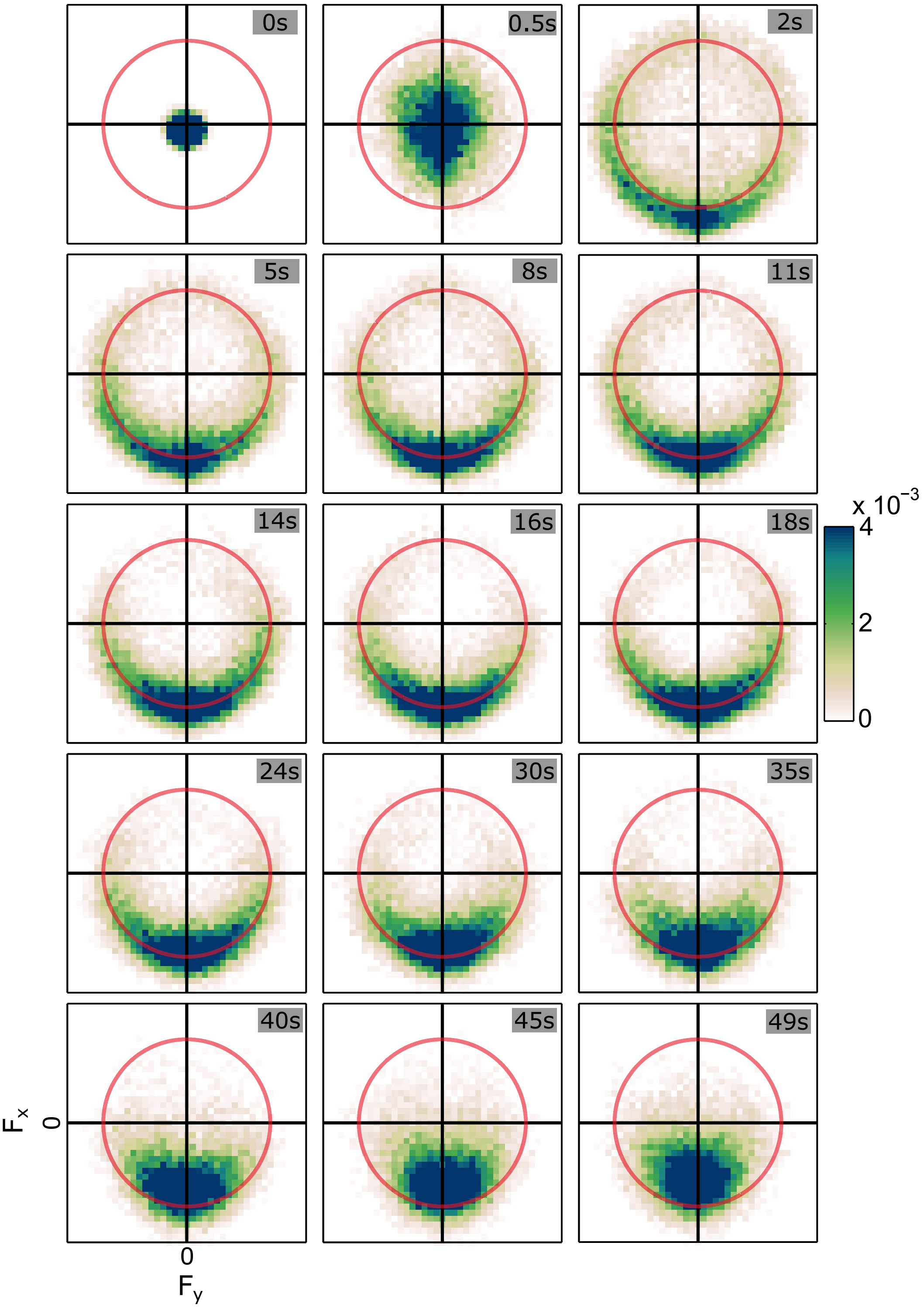

Figure 9.2: **Coherent spinor Bose gas beyond 30 s evolution time.** Histograms of the transversal spin degree of freedom for different evolution times. The probability $p(F_\perp)$ is colour-coded. From every experimental realization we subtract the phase in the middle of the cloud. The red ring indicates a spin with length $|F_\perp| = 0.7$. The initial polar state features small fluctuations around zero spin. Instabilities produce all kinds of spin lengths for short times ($< 2\,\mathrm{s}$). After 5 s the spin length settles around $|F_\perp| \sim 0.7$.

getting more homogeneous over the system. The structure factors of the angular orientation already showed this effect indicated by the transport of excitations towards lower momenta, i.e. by the positive sign of β. The dynamics resembles a type of condensation phenomena far from equilibrium of a complex valued field like that of a one-component Bose gas [134].

9.2 Transversal spin as complex valued field

In the last chapter we compared the universal dynamics of the angular orientation to the dynamics of an $O(N)$-model [68]. We conclude that the $O(N)$-model presumably is in the same universality class as the spin-1 system initialized in the polar state and quenched into the easy-plane ferromagnetic phase. For the $O(N)$-model, one usually looks at the occupation number $n(k) = \hat{\psi}^{\dagger}(k)\hat{\psi}(k)$, where $\hat{\psi}^{\dagger}(k)$ is the bosonic creation operator for a particle in mode k. To make the analogy between the spin system and $O(N)$-model more concrete, we consider an $O(1)$-model which is, in the non-relativistic case, a one-component Bose gas described by the operators $\hat{\psi}^{\dagger}$ and $\hat{\psi}$ and we assume an interaction strength g (see also discussion in section 3.4).

In the following we will argue on a mean field level, i.e. the operators $\hat{\psi}^{(\dagger)}$ get substituted by complex numbers $\psi^{(*)} = \sqrt{N}\exp(\mp i\varphi)$ with N being the atom number [144]. The mean field energy potential for a condensed Bose gas is a mexican hat potential with its radial minimum being at $\sqrt{N}$ (cf. Fig. 7.1). The excitations in the radial direction have an energy gap $\mu = ng$, with density n and interaction strength g; the chemical potential μ is the energy cost for adding a particle to the condensate. Thinking in terms of an experiment, the phase φ of the condensate would be random in each experimental realization. Measuring the amplitude and the phase of the condensate, in analogy to our measurements of $F_{\perp}$, would result in a ring shaped probability distribution similar to Fig. 9.2. The Goldstone mode is gapless and describes phase excitations along the bottom of the mexican hat potential. With Bogoliubov theory, one finds sound excitations with linear dispersion relation for momenta smaller than the healing momentum $k_{\xi} = \sqrt{2mhng}/h$, where m is the atomic mass. One can show that for the Bose gas the low momentum excitations are squeezed in the density direction and enhanced in the phase degree of freedom. The dispersion relation as well as mode functions (u_k and v_k) of the Bose gas Bogoliubov excitations are similar to those for the spin-1 system when considering the Larmor phase degree of freedom (cf. section 7.1.1); for identifying the two one has to replace c_1 by g.

Indeed, the spin-1 system features more degrees of freedom: it is in principle possible to reduce the spin length without reducing coherence, but exciting for example quadrupoles [145]. Our comparisons are based on the experimental observation that a constant spin transversal spin length is build-up dynamically. This is only possible if the fluctuations in all other degrees of freedom (e.g. densities) get reduced. In the quench scenario and the experimental configuration employed here the transversal spin is the emergent relevant degree of freedom. We have already seen that we can hinder this scenario by employing a different initial condition as for example the spin wave in section 7.3.

9.3 Universal dynamics of the transversal spin

Spatially resolved snapshots of the complex valued field $F_\perp$ [119] allow for the extraction of correlation functions. Here, in analogy to $n(k)$ of the $O(N)$-model dynamics, we calculate the structure factor of $F_\perp$. Following the Wiener-Khinchin theorem [146], the structure factor is equivalent to the absolute value squared of the Fourier transform of the field, i.e. ,

$$S(k) \equiv F_\perp^*(k) F_\perp(k) \ (\hat{=}\, n(k)) \ . \tag{9.1}$$

For defining the scaling regime we analyse the mean spin length $\langle F_\perp \rangle$ as a function of evolution times (see Fig. 9.3a). The length is found to be around ~ 0.7 for evolution times between $5\,s$ and $40\,s$; after these times we find a decaying spin length as already indicated in Fig. 9.2. We extract the scaling function as described in the preceding chapter and show the fit results for ζ in 9.3b. We find that it settles to $\zeta \approx 2$ for evolution times beyond 4 s. Together with the spin length this leads us to determine the scaling regime being between 5 s and 35 s. Interestingly the exponent ζ changed from 2.6 close to 2 which would be in accordance with the expectations for the $O(N)$-model. This is not a feature of the transversal spin but correlates with the change of the trapping potential and the reduced heating.

In Fig. 9.3c we show this structure factor for different evolution times, also going beyond the scaling regime. We observe the characteristic shift towards lower momenta ($\beta > 0$) as time evolves. The new trapping configuration allows us to extend the observation time beyond 40 s. We find that after 40 s the system leaves the scaling regime and loses its correspondence with the one-component Bose gas. This is most-likely due to the still present but small decay of coherence and the finite system size.

In this regime the usual rescaling analysis cannot reliably extract β as well as α since there is no plateau in the distribution for times beyond 10 s. We therefore restrict the analysis to $\alpha = \beta$ assuming the transport of a conserved quantity as the underlying phenomenon. This analysis results in $\alpha = \beta = 0.45 \pm 0.05$ which is close to the expected value of $\beta = 1/2$ [68]. Rescaling the data according to the scaling hypothesis we find a reasonable collapse onto the universal scaling function (green solid line; see Fig. 9.3d)). Later times (not shown in d) do not collapse as the dynamics towards the infrared seems to stop possibly due to the finite size of the system. Again we find no scaling for ultraviolet momenta with $k > 0.06\,\mu\mathrm{m}^{-1}$ which is expected from numerical simulations of the $O(N)$-model [68]. The predicted direct cascade transporting energy to the UV cannot be observed yet [68, 134, 135].

For testing a condensation of the spin degree of freedom, it would be necessary to show the phenomenon for different system sizes [104]. We already implemented a setup for local control with which we can create a box-like potential by shining in two blue detuned walls. This opens the perspective of studying the system size dependence by employing differently sized boxes.

The extended range of evolution times gives the possibility to check for prescaling which is indicated by time-evolving scaling functions as well as exponents [129, 147]. Engineered initial conditions tailored such that the dynamics later get into the finite size limit together with a finer time sampling could give access to time varying

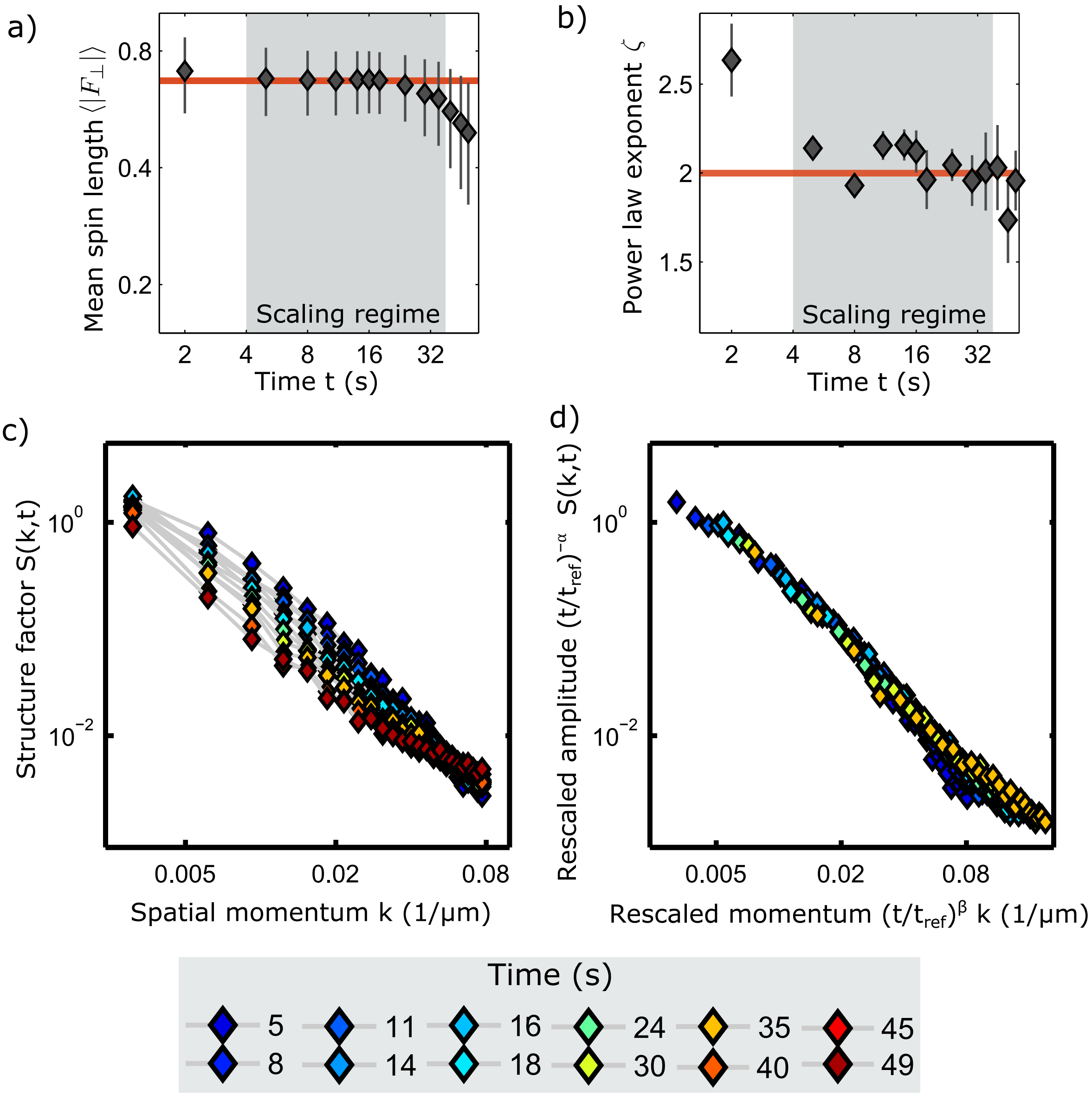

Figure 9.3: **Universal dynamics of $F_\perp$.** a) The mean spin length $\langle|F_\perp|\rangle$ extracted from the histograms in Fig. 9.2. We find a constant spin length of ~ 0.7 (red line) up to ~ 40 s defining the end of the scaling regime. The error bar is given by the standard deviation of the spin length distribution. b) Fitted power law exponent of the scaling function f_S (error bar is 1 s.d. of the fit). After ~ 5 s evolution time we find a nearly constant value of ~ 2. Red line indicates $\zeta = 2$. c) We show the structure factor of the complex valued transversal spin $F_\perp$ on a double-logarithmic scale for different evolution times up to 49 s. We observe the characteristic shift towards lower momenta. For the longest times the shift towards the infrared stops. Together with a) and b) this defines the range of the scaling regime. d) Data in the scaling regime rescaled with $\alpha = \beta = 0.45$; the analysis leads to a collapse of the data onto the universal scaling function in the infrared up to a momentum scale of $\approx 0.04\,\mu\text{m}^{-1}$.

exponents. Further, the long evolution times allow to study a possible thermalization of the spin degree of freedom. It is still not clear what sets the timescales for this process [125] and if it is experimental feasible to observe thermalization starting far from equilibrium.

Finally, we want to emphasize that universal dynamics is a transient phenomenon. Only as long as the fluctuations in all different degrees of freedom are suppressed and the spin length stays constant, we can make the analogy to the one-component Bose gas. It is a dynamical phenomenon which is possible far out of equilibrium, where new symmetries and relevant degrees of freedom may emerge. In the next chapter we will exactly detail this by extracting the quantum effective action and by uncovering the conjectured running coupling in the highly occupied regime [15].

Chapter 10

Extraction of the effective action

In this chapter we report on the experimental extraction of the quantum effective action for a non-equilibrium many-body system. We employ a formalism of quantum field theory based on equal-time correlation functions. It is this formalism that gives us direct experimental access to the one-particle irreducible correlation functions [83] which are the building blocks of a description of the non-equilibrium dynamics based on the quantum effective action. Since estimators for higher order correlation functions will always show non-vanishing amplitudes for a finite sample size, we present a method to test statistical significance. We identify the complex valued field $F_\perp$ as the emerging relevant degree of freedom. We present an expansion of the quantum effective action in the macroscopic field around the expectation value of $F_\perp$. The expansion coefficients in this formulation are the 1PI correlators. Extraction of the 1PI correlators up to fourth order allows for the identification of a dynamically generated weak coupling for low spatial momenta. This is in accordance with expectations in the highly occupied regime already discussed in the context of early-universe cosmology [15]. This chapter is based on [86], with some parts having substantial overlap, others being borrowed verbatim.

10.1 Experimental concept

Before presenting the experimental results we first give an overview of the experimental concept and parameters. For this experiment we again use the $F = 1$ hyperfine manifold to employ spin dynamics and combine it with the quasi one-dimensional trapping potential with trapping frequencies of $(\omega_\parallel, \omega_\perp) \approx 2\pi \times (1.6, 167)\,\mathrm{Hz}$. This leads to coherence times up to $\sim 50\,\mathrm{s}$ and allows us to study the transversal spin up to $18\,\mathrm{s}$ with minimal loss of spin length due to decoherence.

Initially, we prepare the polar state with $\sim 100{,}000$ atoms and quench the detuning to $q \approx |nc_1|$. We observe the dynamics using the $F_x - F_y$ readout (see section 5.5.2) giving us access to spatially resolved snapshots of the complex valued transversal spin $F_\perp(y)$ which we infer from the spin components F_x and F_y measured in $F = 2$ and $F = 1$, respectively (see Fig. 10.1). Combining all spatial points and many realizations (up to ~ 550) we obtain an ensemble averaged distribution function of the transversal spin (right panel in Fig. 10.1) which indicates a nearly constant spin length $|F_\perp|$ for $18\,\mathrm{s}$ of evolution time. Using the spatial information,

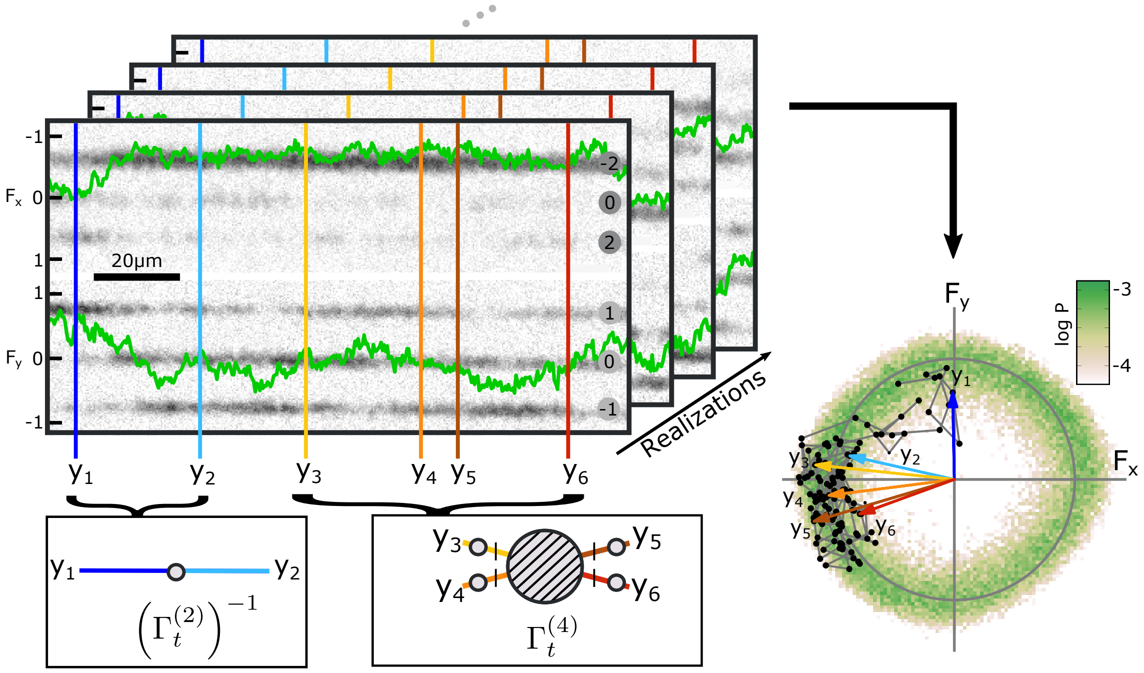

Figure 10.1: **Experimental concept for extracting equal time correlations.** The dynamics in the $F = 1$ hyperfine manifold is observed with the $F_x - F_y$ readout. From the six measured atomic densities (grey shading) we infer the transversal spin components $F_x(y)$ and $F_y(y)$ spatially resolved. The ensemble averaged probability distribution for 18 s resembles a circular form indicating the emergence of a constant spin length. A single experimental realization (black dots, neighbouring points connected by lines) at this time covers a phase range of approximately π. The coloured arrows indicate the transversal spin $F_\perp(y)$ at the positions $y_1, \ldots, y_n$. Many experimental realizations together with the spatial resolution allow us to calculate estimators of higher order correlation functions. Two- and four-point correlation functions are schematically shown. Figure taken and adapted from [86].

we show a representative single realization in this regime (black dots). Spatially neighbouring points are connected by a line and the coloured arrows indicate the transversal spin inferred at the points $y_1, \ldots, y_6$. From this we conclude that the phase degree of freedom is still highly excited in a sense that a single realization spreads over up to half of the circle.

10.2 Emergence of relevant degree of freedom

Analyzing the probability distribution for all evolution times (see Fig. 10.2) we observe that the system dynamically evolves towards a state with constant spin length. Indeed, we find three distinct regimes: For short time < 1 s we find the unstable growth of all spin lengths in any direction (red regime). The time evolution resembles nicely the intuitive picture obtained from the mexican hat analogy in chapter 7. This is followed by an intermediate regime (yellow regime) where the spin excitations are redistributed. Compared to the fast initial dynamics, this is a slow

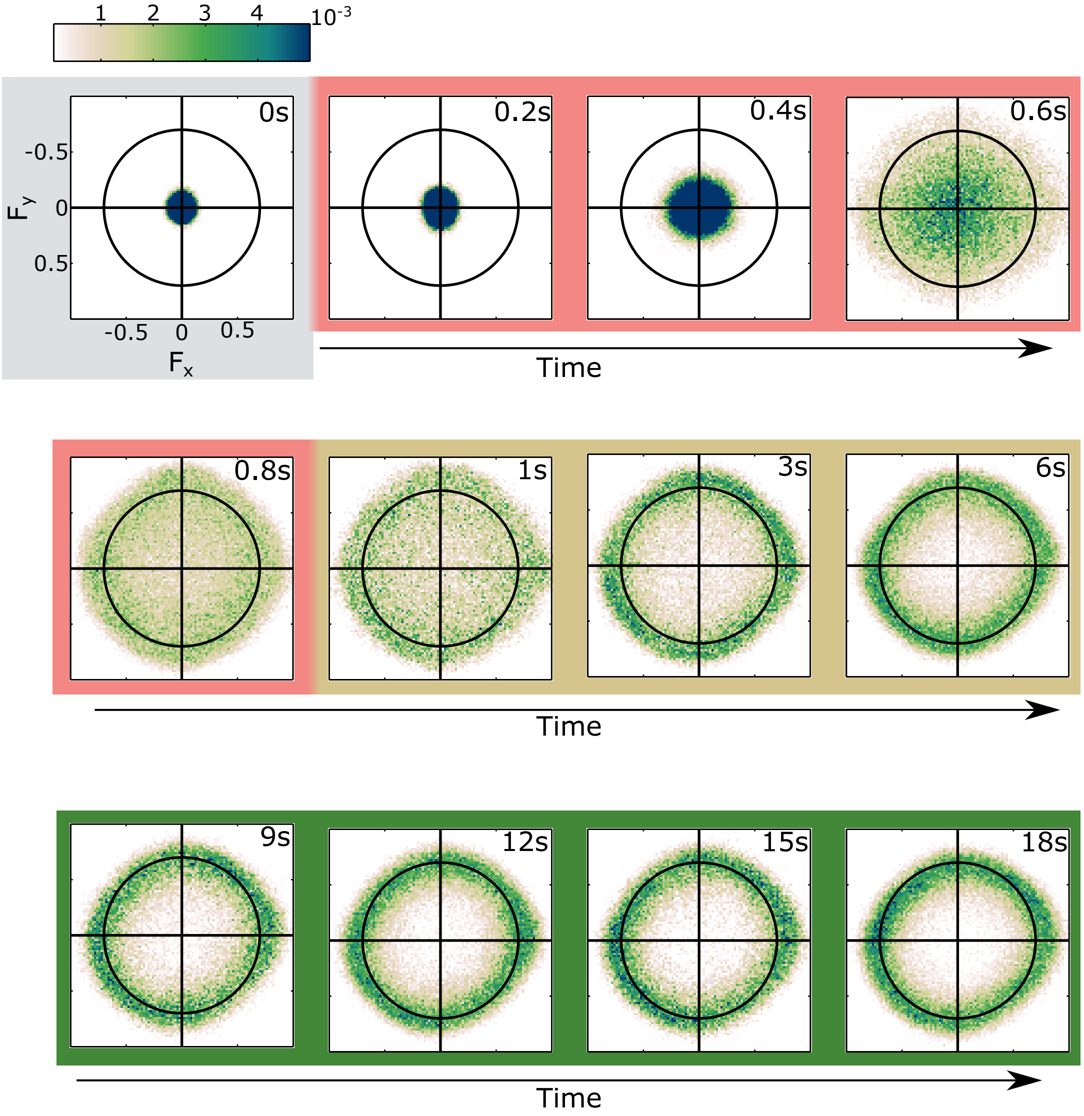

Figure 10.2: **Identification of the emergent degree of freedom.** We show the probability distribution for all evolution times. The circle indicates $|F_\perp| = 0.7$. In the initial unstable regime (red) we find a growth of all spin lengths. The slower intermediate regime (yellow) involves redistribution of spin excitations finally leading to a distribution with nearly constant spin length and phase fluctuations (green).

process . Finally after $\sim 9\,\mathrm{s}$ the system settles in the regime with nearly constant spin length and highly excited phase degree of freedom (green regime). With this we in fact find that the transversal spin field $F_\perp$ is the emergent relevant degree of freedom for the late time dynamics. It is the emergence of a nearly constant spin length with small fluctuations which establishes a correspondence to the one-component Bose gas.

10.3 Low energy effective theory

Here, we give an intuitive picture of the observed phenomenon in the context of spontaneous symmetry breaking (SSB). SSB leads to the emergence of gapless modes which have linear dispersion relation for small momenta. In the low energy regime it is plausible that these degrees of freedom are relevant, in a sense that it is predominantly possible to excite these modes.

At the employed value of q, the ground state is an elongated spin in the transversal plane, breaking the rotational symmetry around the z-axis. In chapter 7 we already identified the Larmor phase excitations of the transversal spin as being gapless, which is exactly associated with this broken symmetry. Based on this fact, one can write down a low energy effective field theory for this gapless degrees of freedom. For this one integrates out the degrees of freedom with a gap. Indeed the density excitations are gapless as well, however, the speed of sound, giving the linear slope, is $\sqrt{c_0/c_1} \sim \sqrt{200}$ times larger than for the Larmor phase excitations. The energy put into the system by the quench is on the order of nc_1 and thus the excitations in this degree of freedom are suppressed.

In this respect the qualitatively different results found for the spin-wave initial condition can be understood as injecting more energy into the system. This facilitates excitations of other degrees of freedom, leading to different dynamical phenomena. This can be visualized with the mexican hat potential. The energy of the local minimum (the unstable fixed point) sets a scale for excitations of the spin length. Thus, spin length excitations are possible for higher energy input.

Experimentally, the spatially resolved measurement together with many realizations allow for the extraction of correlation functions. From those we infer information about the quantum effective action which is formulated in terms of 1PI correlators. The measurement of the quantum effective action may be seen as a way to access the low energy effective theory of the system in the employed far-from-equilibrium situation.

10.4 Experimental extraction of higher order correlation functions

Having identified $F_\perp$ as the effective field relevant for the dynamics we now turn to the extraction of its correlation functions. For an operator $\mathcal{O}_a$ the n-th order equal time correlation function is defined as

$$\langle \mathcal{O}_{a_1} \cdots \mathcal{O}_{a_n} \rangle_t = \mathrm{tr}\left\{ \hat{\rho}_t \mathcal{O}_{a_1} \cdots \mathcal{O}_{a_n} \right\} . \tag{10.1}$$

Evolution Time (s)	**Number of realizations**
9	294
12	511
15	316
18	559

Table 10.1: Number of experimental realizations for the different evolution times.

The average is taken with respect to the density matrix $\hat{\rho}_t$ at a given time t. The collective index a will be specified in the following, but may stand for, e.g. , space coordinates. In fact we calculate estimators for these quantities which in the limit of infinitely many realizations equal the correlations functions. Explicitly, from N measurements we obtain a set of results $\left\{O_a^{(i)} | i = 1 \dots N\right\}$ from which we calculate the estimator

$$\langle \mathcal{O}_{a_1} \cdots \mathcal{O}_{a_n} \rangle_{t,\mathrm{est}} \approx \frac{1}{N} \sum_{i=1}^{N} O_{a_1}^{(i)} \cdot \ldots \cdot O_{a_n}^{(i)}. \tag{10.2}$$

From now on we use for ease of notation $\langle \cdot \rangle_t$ instead of $\langle \cdot \rangle_{t,\mathrm{est}}$ as all shown data points are obtained experimentally. In table 10.1 we give the number of realizations used for the different evolution times to calculate the estimators.

One particle irreducible correlation functions

Let us motivate why we want to obtain one-particle irreducible correlation functions from the estimated full correlators. Correlation functions are a way of extracting and sorting the information obtained about a many-body quantum system. All types of correlation functions bear the same amount of information and it depends on the application which type should be used. Here, we access 1PI correlation functions since they give us access to the quantum effective action.

As discussed, the quantum effective action is a functional depending on some macroscopic field $\Phi^1(y)$ and its complex conjugated field $\Phi^2(y) = (\Phi^1(y))^*$. The full quantum effective action can then be written as

$$\Gamma_t[\Phi] = \sum_{n=1}^{\infty} \frac{1}{n!} \Gamma_t^{\alpha_1,\ldots,\alpha_n}(y_1, \ldots, y_n) \, \Phi^{\alpha_1}(y_1) \cdots \Phi^{\alpha_n}(y_n), \tag{10.3}$$

where we implicitly sum over repeated indices, $\alpha_j = 1, 2$ and integrate over all coordinates y_j with $j = 1, \ldots, n$. The macroscopic field $\Phi(y)$ is connected to the expectation value of the transversal field $\langle F_\perp(y) \rangle$. Indeed, $\Gamma_t[\Phi]$ gives an equation for $\langle F_\perp(y) \rangle$ by

$$\left. \frac{\delta \Gamma_t[\Phi]}{\delta \Phi(y)} \right|_{\Phi(y) = \langle F_\perp(y) \rangle} = 0\,, \tag{10.4}$$

i.e. at the minimum of Γ_t the macroscopic field Φ equals $\langle F_\perp \rangle$. Thus Eq. (10.3) can be seen as an expansion around $\langle F_\perp(y) \rangle = 0$ in our case and Φ captures the behaviour of Γ_t away from the minimum.

Let us now shortly recap the steps which we take for obtaining the 1PI correlators $\Gamma_t^{\alpha_1,\ldots,\alpha_n}(y_1,\ldots,y_n)$ from the measured full correlation functions such as $\langle F_\perp(y_1)F_\perp^*(y_2)\rangle_t$ or $\langle F_\perp^*(y_1)F_\perp^*(y_2)F_\perp(y_3)F_\perp(y_4)\rangle_t$ (see Fig. 10.1). Following the procedure outlined in section 3.3 we subtract the disconnected parts from the full correlators [76] to obtain the connected correlation functions

$$\begin{aligned} C_t^{(2)}(y_1,y_2) &= \langle F_\perp(y_1)F_\perp^*(y_2)\rangle_{t,\mathrm{c}} \\ &= \langle F_\perp(y_1)F_\perp^*(y_2)\rangle_t - \langle F_\perp(y_1)\rangle_t \langle F_\perp^*(y_2)\rangle_t \end{aligned} \tag{10.5}$$

and

$$C_t^{(4)}(y_1,y_2,y_3,y_4) = \langle F_\perp^*(y_1)F_\perp^*(y_2)F_\perp(y_3)F_\perp(y_4)\rangle_{t,\mathrm{c}} \tag{10.6}$$

$$\begin{aligned} &= \langle F_\perp^*(y_1)F_\perp^*(y_2)F_\perp(y_3)F_\perp(y_4)\rangle_t \\ &- \langle F_\perp^*(y_1)F_\perp^*(y_2)F_\perp(y_3)F_\perp(y_4)\rangle_{t,\mathrm{disconnected}} \,. \end{aligned} \tag{10.7}$$

See section 3.3 for all terms contained in the disconnected part. The subtracted disconnected part just includes information from lower order correlation functions. We calculate the connected correlation functions in position space. The scale dependence of couplings in a renormalization group treatment is usually studied in momentum space. This allows for a better separation of the role of different length scales. The observation of translation invariance (see Fig. 10.4) facilitates performing a discrete Fourier transform

$$C_t^{(n)}(p_1,\ldots,p_n) = \underset{y_j\to p_j}{\mathrm{DFT}}\left[C_t^{(n)}(y_1,\ldots,y_n)\right] \tag{10.8}$$

$$\equiv \sum_{y_1=1}^{N}\cdots\sum_{y_n=1}^{N} \mathrm{e}^{-i2\pi y_1p_1}\cdots\mathrm{e}^{-i2\pi y_np_n} C_t^{(n)}(y_1,\ldots,y_n), \tag{10.9}$$

where $p_i \in [p_L, 2p_L, \ldots, Np_L]$, with $p_L = 1/L$ and L the size of the evaluation region. This yields $|C_t^{(n)}(p_1,\ldots,p_n)|$ with momenta p_j $(j = 1,\ldots,n)$. We evaluate the absolute values here because a discrete Fourier transform always suffers from problems defining a phase. This is only a numerical issue as the measurement of the complex valued field in principle also incorporates the phase information. We discuss the possible need for extracting the phase later when we elaborate on the full quantum evolution equation. Within the momentum resolved picture, the macroscopic long wavelength behaviour of the quantum system is encoded in the low-momentum or "infrared" properties of the 1PI correlation functions.

Given a $U(1)$-symmetry, the only independent vertices are

$$\Gamma_t^{1\ldots12\ldots2}(y_1,\ldots,y_n) \equiv \Gamma_t^{(n)}(y_1,\ldots,y_n)$$

with n even and equally many field and conjugate field components. The transversal spin resembles this symmetry because a global change of the Larmor phase, i.e. $F_\perp(y) \to F_\perp(y)\mathrm{e}^{i\varphi'}$, does not change the Hamiltonian (5.11). Besides the $U(1)$-symmetry, magnetic field fluctuations render correlation functions zero for n uneven. The phase is initially undefined (starting in the polar state) and becomes randomized during the course of the evolution time.

The connected correlators are decomposed into their irreducible parts representing the proper vertices. More precisely, we extract

$$\Gamma_t^{(2)}(p,-p) \equiv \Gamma_t^{(2)}(p) = \left(C_t^{(2)}\right)^{-1}(p) \tag{10.10}$$

from the inverse of the connected two-point correlator. The 1PI four-point correlation function for our $U(1)$-symmetric case is given by

$$\Gamma_t^{(4)}(p_1,p_2,p_3,p_4) = -\Gamma_t^{(2)}(p_1)\,\Gamma_t^{(2)}(p_2)\,\Gamma_t^{(2)}(p_3)\,\Gamma_t^{(2)}(p_4)\,C_t^{(4)}(p_1,p_2,p_3,p_4)\,. \tag{10.11}$$

From the pictorial representation of the correlation functions we can infer that acting with the inverse two-point correlators on the connected four-point function corresponds to removing the ‘external legs’ of the diagram (see Fig. 3.1 and Fig. 10.1).

Higher order correlators as multivariate cumulants

Calculating higher order correlation functions requires a careful data analysis. Formulated differently, we are facing the problem of calculating an estimator for a multivariate cumulant for a sample with finite statistics. The multivariate random variable in our case is the measured macroscopic field $F_\perp^{(*)}(y)$, where multivariate indicates the dimension > 1 of the random variable vector; in our case it is the number of spatial points. We identify two major challenges which are detailed in this section.

First, the calculation and the storage of higher order multivariate cumulants is computationally expensive, because the size of the tensor grows as N^n where N is the length of the random variable vector and n is the order of the correlation function. As we are interested in the infrared modes in this thesis we bin nine adjacent pixels of the recorded image before inferring the transversal spin. This reduces the number of points to ~ 20 and makes the computation up to $n = 4$ feasible on a conventional computer in reasonable time. For the calculation we use the julia package *Cumulants.jl* which is a very efficient implementation of an algorithm based on tensor operations [148].

The second issue is that even in the case of multivariate Gaussian random variables, estimators of higher order correlators ($n > 2$) will show non-vanishing signals. Thus it is important to quantify the statistical significance of the experimental data. First we calculate a statistical error by employing a *bootstrapping method* [149]. Similar to the jackknife method, bootstrapping circumvents the problem of implementing error propagation when mathematically complicated estimators (here the cumulants) are used. This is achieved by a definition which relies on repeating the calculation of the estimators for a new set of samples. Explicitly, for a measured sample $\left\{O_a^{(i)} | i = 1, \ldots, N\right\}$, one draws new samples, the bootstrap samples, $\left\{O_a^{(i^*)} | i^* \in \{1, \ldots, N\}\right\}$, where the * indicates the resampled set. The subtlety is that the resampled set is drawn with replacement, i.e. , the index i^* may take the same number twice or even multiple times. From this generated sample we can now calculate a result $\theta^*(b)$ for the given estimator. Repeating this procedure

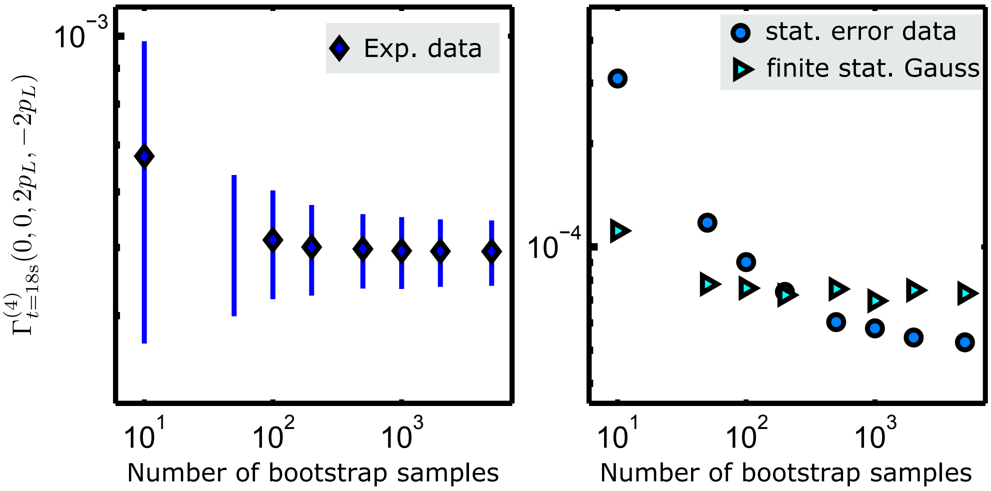

Figure 10.3: **Bootstrap resampling.** a) Experimentally extracted 1PI four-vertex $\Gamma^{(4)}_{t=18\,\mathrm{s}}(0,0,p,-p)$ for $p = 2p_L$ as a function of the bootstrap samples. The error bar is the statistical error inferred from bootstrapping. b) Statistical error of the experimental data (circles) as a function of bootstrap samples. The error reduces with the number of samples and slowly converges for sample size larger $\sim$ 5000. The diamonds show the finite statistics bias of the drawn Gaussian data.

B times, called bootstrap samples, we infer the standard error $\hat{\mathrm{se}}_B$ of the mean $\bar{\theta}^* = 1/B\sum_{b=1}^{B}\theta^*(b)$ by calculating

$$\hat{\mathrm{se}}_B^2 = \frac{1}{(B-1)}\sum_{b=1}^{B}\left[\theta^*(b) - \bar{\theta}^*\right]^2 . \tag{10.12}$$

The appropriate number of bootstrap samples B has to be checked from case to case. In Fig. 10.3 we plot the expectation values as well as the statistical error as a function of the bootstrapping samples. We find that $\sim$ 1000 bootstrap samples give a reasonable result. As the needed computational time is linear in the number of bootstrap samples, the described amount of samples is indeed a limiting factor.

In principle, the observed fluctuations could just result from Gaussian fluctuations since we use a set with finite statistics. Therefore we want to compare our results to an expectation of a Gaussian model, which we set up with the help of the measured data. We define a multivariate Gaussian distribution by using the two-point correlator as the covariance matrix. From this, we draw new samples with the same size of statistics but with Gaussian fluctuations. The data from this Gaussian model is processed in exactly the same way as the experimental data; the result we call *finite statistics bias*. Knowing the distribution allows us to repeat the procedure of calculating the finite statistics bias with different data to reduce the statistical error on the bias estimation to zero. In Fig. 10.3 we also show the calculated finite statistics bias as a function of used samples and find convergence. We will show the finite statistics bias in the following plots always as lower bounds and call points which are in 1 s.d. above this value statistically significant.

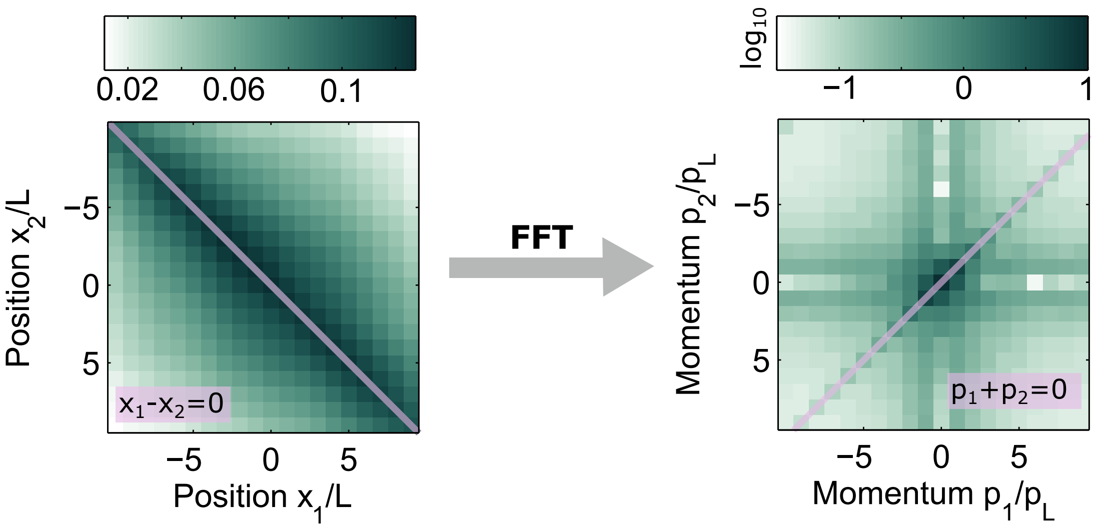

Figure 10.4: **Structure of two-point correlator.** Left panel: Two-point correlator $C^{(2)}_{t=18\,\mathrm{s}}(x_1, x_2)$ with colour-coded amplitude. Purple line indicates the direction of $x_1 - x_2 = \text{const}$. Right panel: Fourier transformed two-point correlator with log scale amplitude. We predominantly observe a signal when $p_1 + p_2 = 0$ (purple line) which indicates a momentum conserving structure due to the translation invariance in the left panel.

Additionally we want to give another way for judging the statistical significance which is not primarily for quantitative purposes but can give qualitative insights. The idea is to "normalize" the data to its covariance matrix [150] in the following fashion

$$F'_\perp(y') = \sum_y \sqrt{C^{-1}_{yy'}}\,(F_\perp(y) - \langle F_\perp(y)\rangle)\ . \tag{10.13}$$

Here, $C_{yy'} = \langle F^*_\perp(y) F_\perp(y')\rangle_C$ is the covariance matrix and the procedure leads to $C'_{yy'} = \langle F'^*_\perp(y) F'_\perp(y')\rangle_C = \delta_{yy'}$. The method is called *standardization* if the true value of the covariance matrix is known; in case of only having an estimator it is called *studentization*. For a comparison this method is in particular capable of removing a strong momentum dependence of the correlators which generates also strongly momentum dependent finite statistics biases.

10.5 Structure of the 1PI vertex

After defining the relevant observables, we start by examining the structure of the correlation functions. An n-point correlation function is in general an n-dimensional object and with that hard to visualize for $n > 2$. Identifying symmetries helps to ease visualization and also lets us learn something about the system's dynamics. Translational invariance, i.e. invariance of the observables under changing the space coordinate like $x_i \to x'_i = x_i + \delta x\,(i = 1, \ldots, n)$, leads in momentum space to a "momentum conserving" structure. This means we only find non-zero entries for an n-point correlator when $p_1 + p_2 + \cdots + p_n = 0$.

Connected two-point correlator

First we have look at the connected two-point correlator which can be displayed in two dimensions. The left panel of Fig. 10.4 shows the two-point correlator $C^{(2)}_{t=18\,\mathrm{s}}(x_1, x_2)$ where the amplitude is colour-coded. The approximate homogeneity along the purple line ($x_1 - x_2 = 0$) indicates translational invariance. In momentum space (right panel: logarithm of amplitude) we predominantly find a signal on the *momentum conserving diagonal* with $p_1 + p_2 = 0$ which is indicated by the purple line. We attribute the cross structure to finite size effects in the Fourier transform.

Here, in contrast to the preceding chapters, we calculate the full two-dimensional two-point correlator. In accordance with the spectra shown so far, we also find a strong momentum dependence with maximal amplitude at $p_1 = p_2 = 0$. We will show later that we indeed find universal dynamics consistent with the results presented earlier.

1PI Four-point correlator

Having identified the momentum conserving structure of the two-point correlator we directly analyse the four-point correlators in their 1PI form. We start by presenting in Fig. 10.5 part of the full "tensor" for the experimental data as well as the associated Gaussian model. In each square marked by the grey lines we fix two momenta p_1 and p_2 and vary p_3 and p_4. The amplitude of the correlator is colour-coded (see colorbar on the right). We identify an overall momentum dependence. Within each square the amplitudes increase with increasing momenta; the same holds in the big square. The Gaussian model shows a qualitatively similar behaviour. This means that the strongly momentum-dependent two-point correlator leads to a strongly momentum-dependent finite statistics bias for the four-point 1PI correlator. Taking a closer look at the squares with low ($p/p_L < 3$) momenta p_1 and p_2 we further find a prominent contribution on the momentum conserving diagonal.

For a more detailed analysis of the structure we show in Fig. 10.6a the central square $\Gamma^{(4)}_{t=18s}(0, 0, p_3, p_4)$. We find a momentum conserving structure identified by a prominent signal on the diagonal $p_3 + p_4 = 0$. Further we observe a strongly momentum dependent cross structure. For identifying its nature, we plot the same slice for the Gaussian model. Even the Gaussian shows the strongly momentum dependent cross structure but not the momentum conserving diagonal elements.

The experimental extraction of the 1PI four-point correlations requires sufficiently many experimental realizations to ensure the statistical significance of the results. For judging the statistical significance of the observed effects we divide the experimental data by the Gaussian model at each momentum (see Fig. 10.6b). We find the momentum conserving diagonal to be statistically significant. Still, there is a reminiscent signal from the cross structure. In Fig. 10.6c we show different slices by varying the momenta p_1 and p_2 to give an overview of the whole matrix. Only low momenta show statistically significant diagonals; we attribute this to the high oscillation frequencies which are harder to resolve with statistical significance for a fixed amount of statistics.

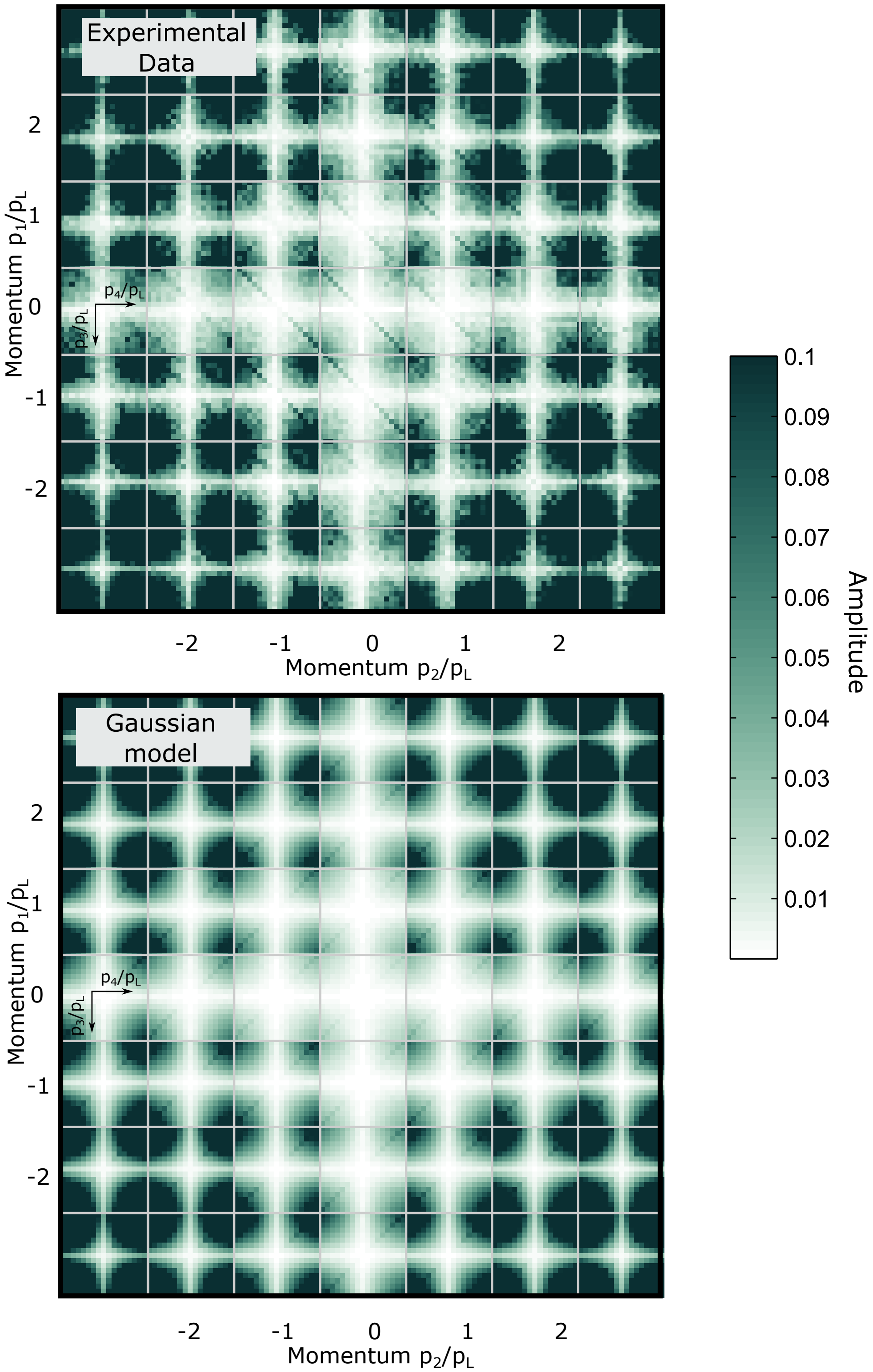

Figure 10.5: **Full matrix of four-vertex.** We show the full four-point 1PI matrix in a two-dimensional plot by fixing the momenta p_1 and p_2 in each square (marked by the grey horizontal and vertical lines) and showing the dependence on p_3 and p_4. The upper panel shows the results for the experimental data and the lower panel is the Gaussian model calculated from the experimentally obtained two-point function. The grey diagonals indicate $p_1 + p_2 + p_3 + p_4 = 0$. Figure taken and adapted from [86].

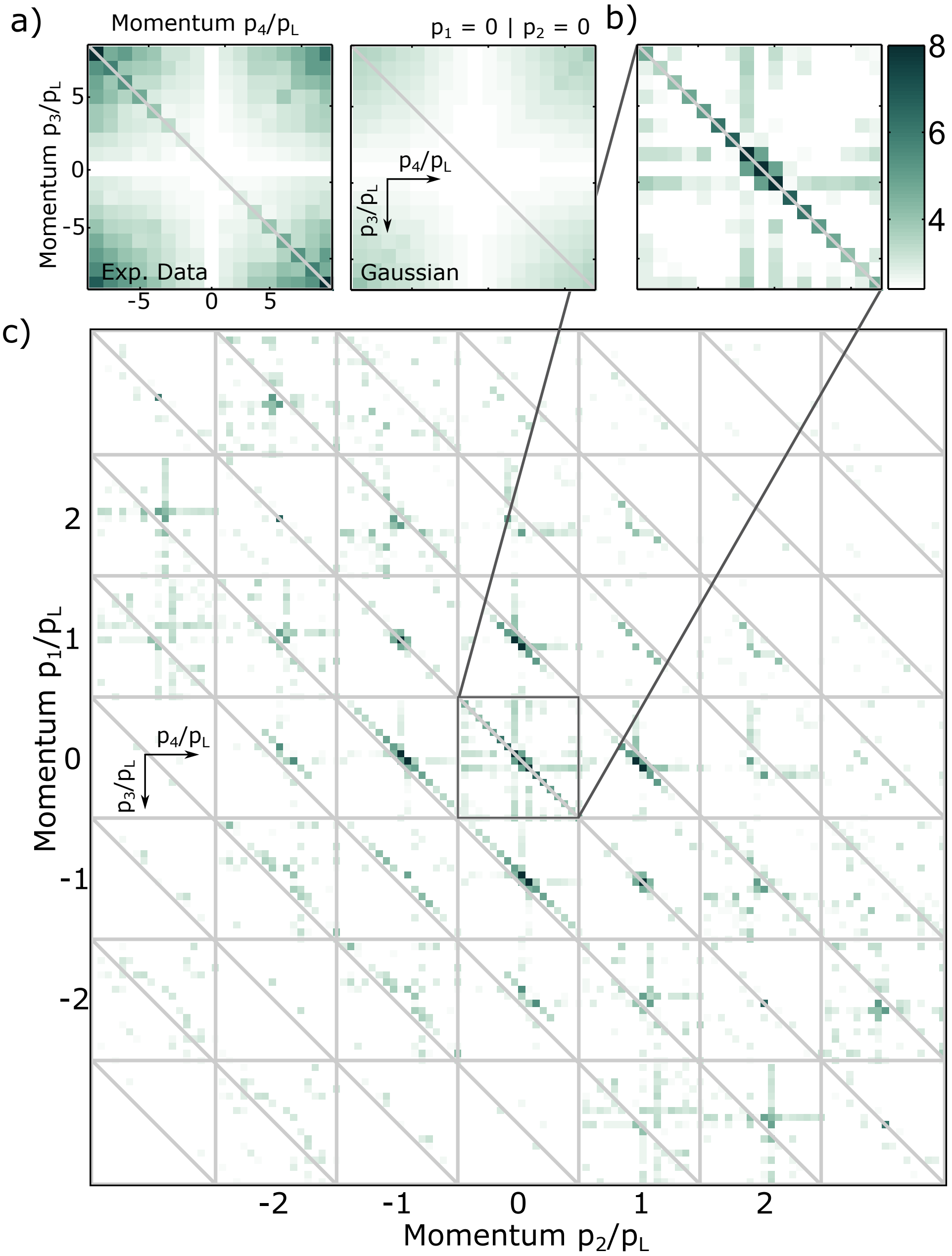

Figure 10.6: **Statistical significance of the four-point 1PI correlator in momentum space.** a) 1PI four-vertex $\Gamma^{(4)}_{t=18s}(0, 0, p_3, p_4)$ for experimental data (left panel) as a function of the two momenta p_3 and p_4. For comparison we show the same slice for the Gaussian model with same statistics (right panel). We normalize all momenta to $p_L = 1/L$, the momentum corresponding to the size L of the evaluation region. b) For judging the statistical significance of the inferred signal we plot the ratio of experimental data and Gaussian model. c) $\Gamma^{(4)}_{t=18s}(p_1, p_2, p_3, p_4)$ for different p_1 and p_2 (fixed in each grey square) divided by the Gaussian bias. An overall momentum conserving structure is revealed by the signal being predominantly on the momentum conserving diagonals $p_1 + p_2 + p_3 + p_4 = 0$. Diagonals indicate $p_3 + p_4 = 0$. Figure taken and adapted from [86].

10.6 Identification of running couplings

In the analyzed regime the system is still far from equilibrium. One can anticipate that the quantum effective action is a time-evolving object as well. However, it is insightful to look at Γ_t for fixed time t as this allows for a characterisation of the state. This becomes also apparent thinking of thermal equilibrium, where the quantum effective action is a powerful concept and the system does not evolve in time.

1PI two-point correlator

From Eq. (10.10) one sees that the 1PI two-vertex is in our case the matrix inverse of the connected two-point correlator. With this in mind we expect to find a strongly momentum dependent signal in the infrared which stems from the high occupations. In Fig. 10.7a we first show the momentum conserving diagonal $\Gamma^{(2)}_{t=18\,\mathrm{s}}(p,-p)$. The double-logarithmic scale allows for the identification of a power-law functional form $\propto p^2$. We find a momentum dependent amplitude over nearly two orders of magnitude and observe a suppression in the infrared [18, 19] up to a characteristic momentum set by the inverse of the length scale $l_s \sim 30\,\mu\mathrm{m}$.

1PI four-point correlator

For the four-vertex we have different choices of momentum conserving diagonals. We show three different ones in Fig. 10.7b-d. Statistical significance is only found for over-all low momenta (cf. Fig. 10.6). We compare to the finite statistics bias obtained from the Gaussian model which is indicated by the grey shaded region. The complex order parameter allows us to distinguish between the case $(0,0,p,-p)$ and $(0,p,0,-p)$. Further we show one diagonal with a fixed non-zero momentum, namely $(p_L,0,p-p_L,-p)$, to stress that the observed phenomena are generic and not restricted to diagonals with two momenta equal to zero.

In Fig. 10.8 we further show the same diagonals for different employed evolution times. This allows to judge the influence of statistics (see table 10.1). The times with lower statistics feature larger statistical errors and less difference to the Gaussian model.

In the infrared, we observe a strongly reduced amplitude of the correlators. Every reduction is always meant with respect to a constant 4-vertex which is expected in the perturbative regime [151] usually recovered for momenta above a certain scale. In this regime, the 4-vertex equals to the bare coupling of the microscopic theory. The current amount of statistics does not allow us to resolve that regime. As already discussed in section 3.5, this momentum-dependence indicates running couplings which are defined as momentum dependent expansion coefficients of the quantum effective action. This is in accordance with the fact that renormalization effects lead to scale-dependent descriptions.

These observations demonstrate that the infrared regime exhibits a strongly suppressed interaction vertex in this far-from-equilibrium situation. This was expected from analytical calculations and numerical simulations for the $O(N)$-model [15, 68, 90, 136]. There are no analytical or numerical predictions applicable for a

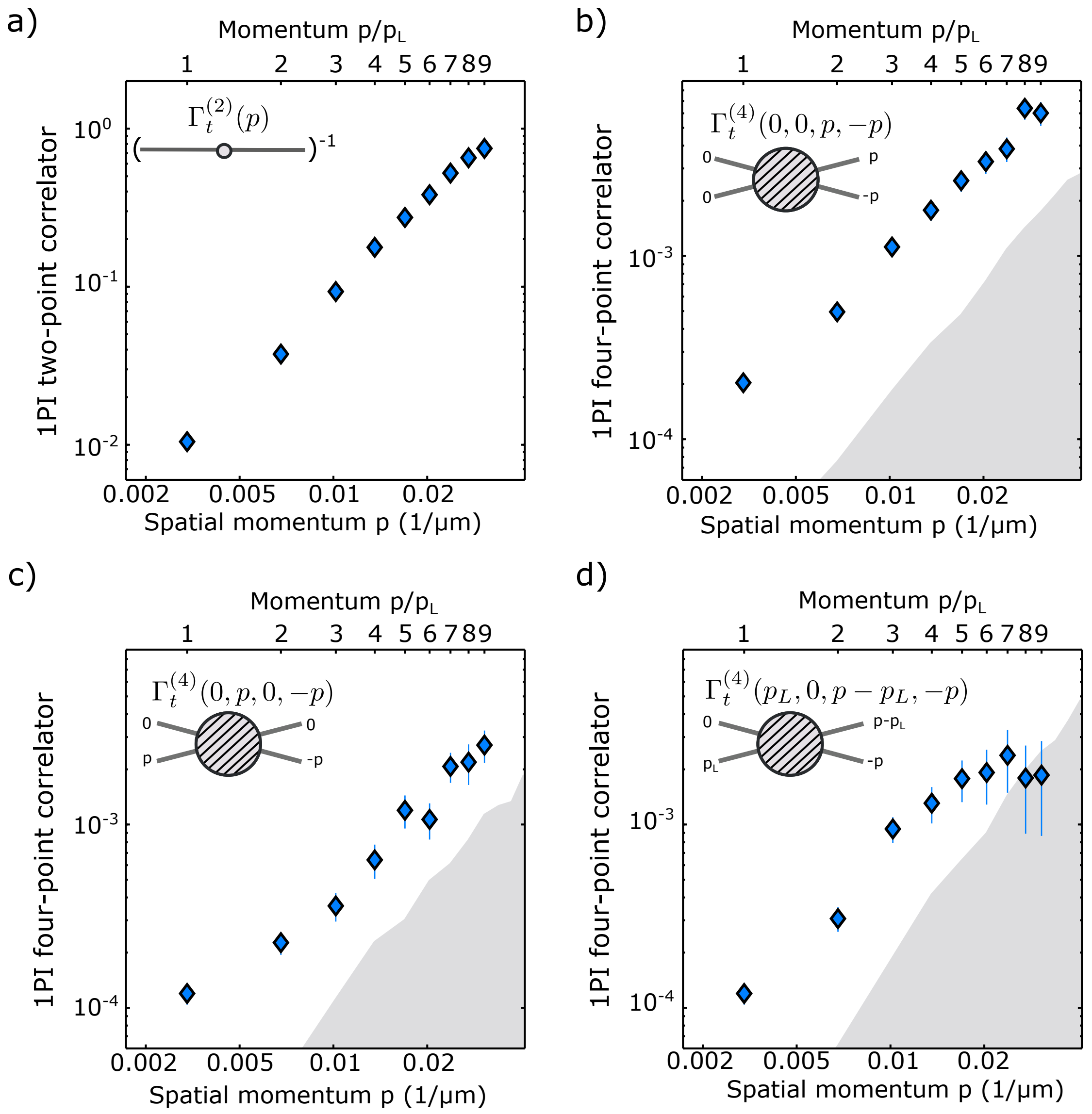

Figure 10.7: **Momentum dependence of two- and four-point 1PI correlator.** Momentum conserving diagonals of two- and four-point 1PI correlator as a function of the spatial momentum p on a double-logarithmic scale. a) $\Gamma^{(2)}_{t=18\,\mathrm{s}}(p,-p)$ shows a strong momentum dependence with a strong reduction in the infrared; the low amplitudes correspond to the high occupations found in the infrared for the structure factor (cf. Fig. 9.3). b)-d) $\Gamma^{(4)}_{t=18s}(p_1,p_2,p_3,p_4)$ with two fixed momenta as indicated. The complex-valued field allows the distinction between case b) and c). The upper limit of the grey area is the result obtained from the Gaussian model with same statistics. We find statistically significant data in the infrared. The correlators feature a momentum dependence over almost two orders of magnitude indicating the dramatic renormalization of the (running) couplings. All error bars shown are 1 s.d. calculated from bootstrap resampling. Figure taken and adapted from [86].

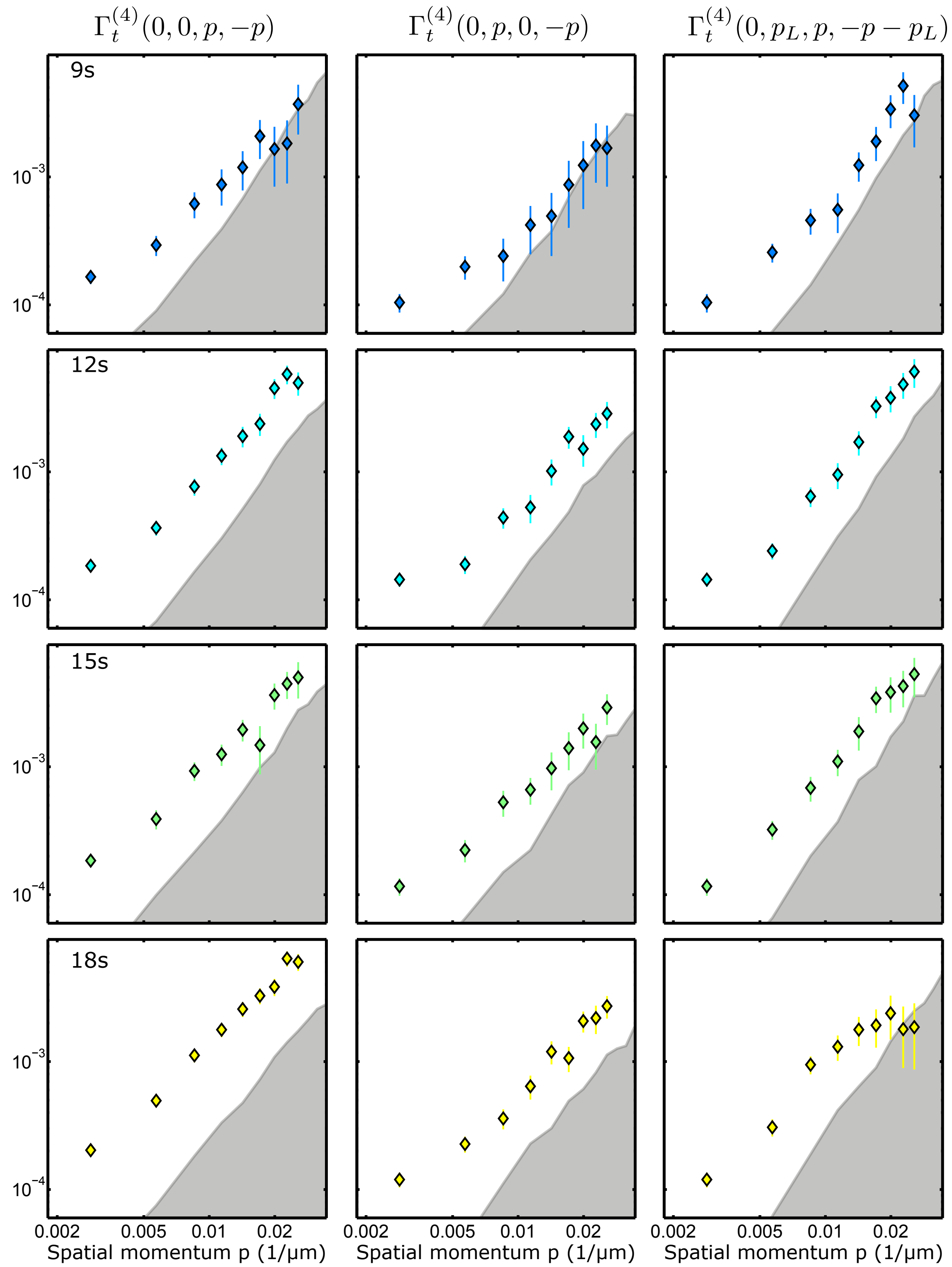

Figure 10.8: **Momentum conserving diagonals of 1PI four-point correlator for all employed times.** Same diagonals as shown in Fig. 10.7b-d but for different times between 9 s and 18 s. The different employed statistic shows an effect on the statistical error bar and the significance(see table 10.1 for statistics). Figure taken and adapted from [86].

comparison with our system. The analytical predictions for the $O(N)$-model [90] are not applicable in one dimension and on the numerical side, the extraction of 1PI correlation functions is not explored in great detail.

10.7 Time evolution of 1PI correlators

In section 3.4 we outlined a derivation of the full quantum evolution equation for the distribution function. Our method in principle presents the means for explicitly solving this equation experimentally. For this, one would have to measure the effective action for all evolution times. This can be seen in the spirit of a quantum computation defined in chapter 4.

In general, the solution of the time evolution is an unfeasible task, as the time resolution that is necessary to resolve the relevant dynamics can be infinitesimally small. However, we now show that in the vicinity of a non-thermal fixed point also the dynamics of the 1PI correlators becomes universal and with that the dynamical evolution of the quantum effective action. The simple description inherent to universal dynamics allows us to resolve the evolution for a long time interval by measuring a few evolution times only.

Full quantum evolution equation

In section 3.4 we detailed the derivation of an exact evolution equation for the two-point function $C_t^{(2)}(p)$ of the one-component Bose gas:

$$\begin{aligned}\partial_t C_t^{(2)}(p) = g \int_{q,r,l} i \left[\Gamma_t^{(4)}(p,q,-r,-l) - \Gamma_t^{(4)}(l,r,-q,-p)\right] \times \\ \times C_t^{(2)}(p) C_t^{(2)}(q) C_t^{(2)}(r) C_t^{(2)}(l)\ .\end{aligned} \tag{10.14}$$

Here, $C_t^{(2)}(p)$ has the interpretation of an occupation number distribution. In the theoretical model the total number $\int_p C_t^{(2)}(p)$ is conserved because of the assumed $U(1)-$symmetry. Experimentally the conservation corresponds to the equality of the found universal exponents α and β.

Eq. (10.14) determines the time evolution of $C_t^{(2)}(p)$ in a kinetic description in the framework of quantum field theory. The numerical solution of such equations is hard as they usually involve length scales over several orders of magnitude. This, combined with the fact that the four vertex $\Gamma_t^{(4)}$ is in general time-dependent, limits the practical use. One has to find either approximate solutions for limiting cases or directly determine parts of this equation experimentally. The latter approach is pursued here.

Finally, let us comment on the structure of the integrand. The difference in the collision integral may be interpreted as the imaginary part of the correlator. Exploring the phases of the complex-valued correlators rather than (just) the absolute value, which we have done so far, may lead to interesting insights in the future. For instance, the correlation functions can oscillate in time which is possibly important for the dynamics.

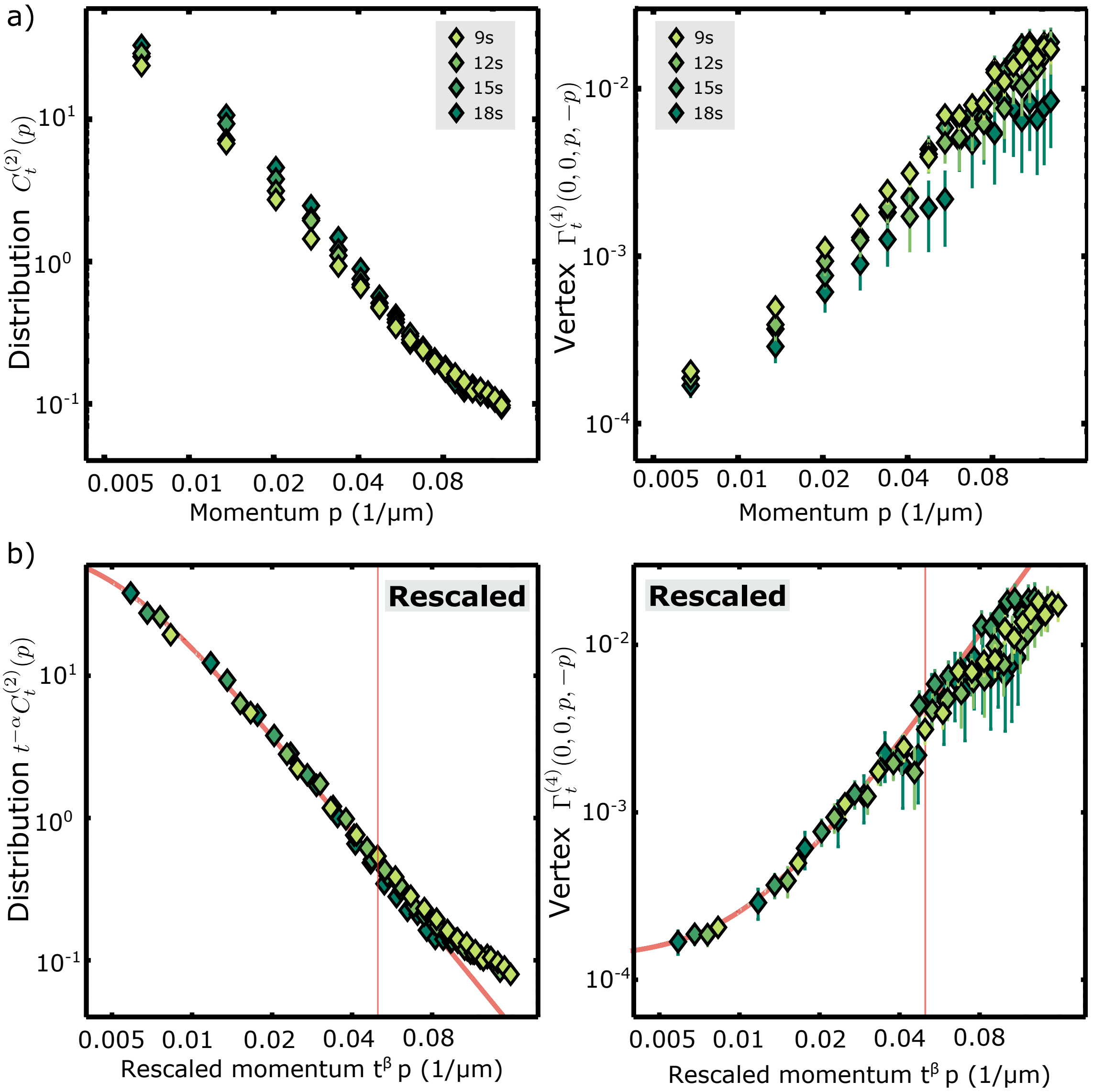

Figure 10.9: **Universal dynamics of building blocks of full quantum evolution equation.** a) Time evolution of the distribution function (left panel) and the 1PI 4-vertex for the diagonal $(0, 0, p, -p)$. We find a characteristic shift in time towards the infrared. b) Same data as in a) but rescaled according to Eq. (10.17) and 10.18. For the distribution we use $\alpha = \beta = 1/2$; the 4-vertex is rescaled with $\beta = 1/2$ and $\gamma = 0$. We fit the universal scaling function (see main text) up to $\sim 0.04\,\mu\text{m}^{-1}$ (red line). Figure taken and adapted from [86].

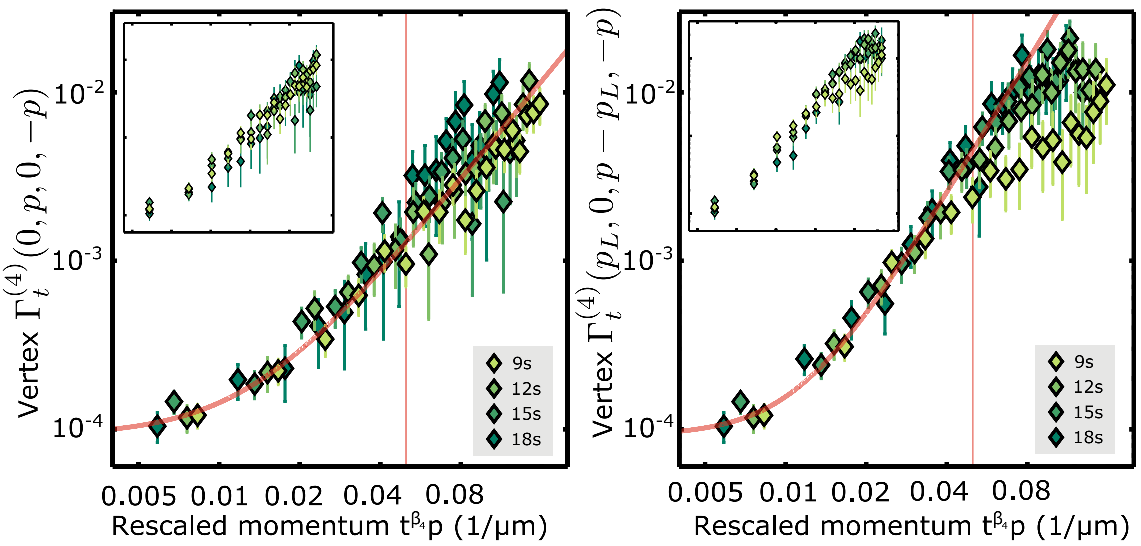

Figure 10.10: **Universal dynamics of 4-vertices.** Rescaled data ($\beta = 1/2$ and $\gamma = 0$) for the two additional diagonals shown in Fig. 10.7c-d. The inset shows the unscaled data. Figure taken and adapted from [86].

Dynamics in the highly occupied regime

For the distribution function $C^{(2)}(p)$ we observed high occupation numbers and even transport towards the infrared. In general, it is an open question how a system dynamically counteracts an ever growing occupation due to the Bose-enhancement from the high occupancies at low momenta. This scenario cannot be captured by "standard" kinetic theory; "standard" means taking a Boltzmann-equation with an interaction constant not depending on momentum. With our results we have determined (parts of) the defining parameters $\Gamma_t^{(4)}(p_1, p_2, p_3, p_4)$ of the presented evolution equation. Indeed, Figs. 10.7, 10.9 and 10.10 show that the momentum-dependent vertex $\Gamma_t^{(4)}$ drops by almost two orders of magnitude as the occupancy grows strongly towards lower momenta. The reduced effective interaction strength diminishes the rate of change of the distribution $C^{(2)}(p)$ according to Eq. (10.14).

Expectations for scaling

The full quantum evolution equation is derived for a one-component Bose gas assuming the described correspondence. Unfortunately, the current level of statistics does not allow us to explicitly test this equation as the finite statistics bias dominates when integrating (summing) the right hand side.

One can think of different ways to verify the evolution equation by testing relations of the scaling exponents. The simplest ansatz is assuming a constant amplitude scaling factor γ for all diagonals of the 4-vertex. By counting powers of time one can deduce a value of $\gamma = 1$. It is important to note that it was shown in [90] that the 4-vertex in different momentum regimes may exhibit different amplitude scaling exponents and functional power laws[1].

---

[1] Result transferred from unequal time formalism.

The scaling as well can be checked for the collision integral $\mathcal{C}_p\left[C_t^{(2)}, \Gamma_t^{(4)}\right]$ which is the right hand side of Eq. (10.14). Inserting the scaling relation for the distribution function we find

$$\begin{aligned} t^\eta \mathcal{C}_S\left[C_t^{(2)}, \Gamma_t^{(4)}\right] = \mathcal{C}_p\left[C_t^{(2)}, \Gamma_t^{(4)}\right] &= \partial_t C_t^{(2)}(p) & (10.15)\\ &= \partial_t t^\alpha C_S(t^{\beta_2} p) & (10.16)\\ &= t^{\alpha-1} g(t^{\beta_2} p) \end{aligned}$$

with a function g depending only on $t^{\beta_2}p$. The amplitude scaling exponent of the collision integral is then found to be $\eta = \alpha - 1$.

Universal dynamics of 1PI four-vertices

Finally, we want to report on the observations concerning scaling of the experimentally accessible parts. As expected in the employed regime, we find scaling for the two-point correlator:

$$C_t^{(2)} = t^\alpha C_S(t^{\beta_2} p) \tag{10.17}$$

with $C_S \propto \left(1 + (p/p_S)^{\zeta_2}\right)^{-1}$. The exponent is found by employing a rescaling analysis which assumes $\alpha = \beta_2$. The analysis yields that β_2 is in the error consistent with the expected exponent 1/2 [18, 68] (see Fig. 10.9a left panel). Moreover, in our experiment we find self-similar dynamics for the statistically accessible diagonals of $\Gamma_t^{(4)}$ according to

$$\Gamma_t^{(4)}(0, 0, p, -p) = t^\gamma \Gamma_S(0, 0, t^{\beta_4} p, -t^{\beta_4} p) \tag{10.18}$$

with scaling exponents γ and β_4. In Fig. 10.9 we show the time evolution (right panel of a) and the rescaled data (right panel of b) with $\gamma = 0$ and $\beta_4 = 1/2$ revealing a scaling collapse onto the function $\Gamma_S \propto 1 + (p/p_S)^{\zeta_4}$ with $\zeta_4 = 2.2$. Intuitively the scaling exponent β describes how fluctuations on different length scales are connected in the universal regime. Thus, we anticipate that $C_t^{(2)}$ and $\Gamma_t^{(4)}$ have the same momentum scaling exponents, i.e. $\beta_2 = \beta_4$. We use this assumption for constraining the scaling analysis of $\Gamma_t^{(4)}$ to find γ being consistent with 0.

Part IV

Concluding Remarks

Chapter 11

Summary

In this thesis we have investigated the possibility of experimentally testing quantum field theoretical concepts. To set the stage, we first introduced the relevant concepts in Part I. We presented ideas for many-body systems that are well-known from equilibrium and generalized to situations far from equilibrium. We proceeded by giving an overview of QFT from an experimentalist's point of view which aims to be both intuitive and concise. To meet the capabilities of ultracold atom experiments, we employed a formulation of QFT based only on equal-time correlation functions. Within the Wigner formalism, we derived a full quantum evolution equation for the particle number distribution. We concluded by introducing the concept of renormalization and running couplings. In the end we gave our definitions of quantum computation and quantum simulation to put the experimental studies into context.

In Part II we presented the experimental platform used within this thesis: a spinor Bose-Einstein condensate confined in a quasi-one-dimensional trap geometry. We introduced the electronic groundstate hyperfine manifold in a magnetic field and the possibilities for controlling the effective quadratic Zeeman shift which is the experimental control parameter for employing quenches. The microscopic Hamiltonian describing the dynamics is presented based on spin-1 matrices. Because an appropriate readout of the relevant degrees of freedom is important for doing quantum simulations, we discussed the experimental techniques for accessing the transversal spin field in detail. Finally, we commented on the long time scales employed, which are experimentally challenging.

Part III is concerned with the experimental results obtained during this thesis. First we probed the phase diagram by using quenches from the polar state into the different phases and by measuring the spin fluctuations for long evolution times. Based on this measurements, we studied the instabilities occurring for short evolution times. We found qualitative agreement between theoretical expectations from Bogoliubov theory and experiment. The results verify a high degree of control for preparing the system far from equilibrium. For long times after the quench we observed universal dynamics in the angular orientation of the transversal spin. This dynamics were indicated by rescaling of the correlation functions in momentum space with universal exponents $\alpha = 0.33$ and $\beta = 0.54$. We probed the expected insensitivity to microscopic details by preparing different initial conditions. Using a new spin readout we investigated universal dynamics for the complex valued transversal spin field up to 40 s. Enhanced coherence times after optimizing the trapping potentials facilitated the long evolution times. Moreover, we discussed the similarities between the transversal spin field and a one-component Bose gas which are reasonable given the small fluctuations in density and spin length observed in the experiments. Finally we reported on the extraction of the quantum effective action. Based on the notion of low energy effective theories, the transversal spin field was identified as the emergent relevant degree of freedom. We detailed the experimental procedure for extracting one-particle irreducible correlation functions and presented methods for judging their statistical significance. The structure of the 2- and 4-vertex is investigated and in the infrared regime we find a strong suppression of the 4-vertex. We studied the time evolution of the system and found universal dynamics also for the 4-vertex in accordance with the derived full quantum evolution equation.

This thesis is just the starting point of further insightful experimental studies of quantum field theory. In the following chapter, we present an outlook on various experiments which we have already set up and performed first measurements as well as some that may be accomplished in the near future.

Chapter 12

Outlook and challenges

The experimental applicability shown in this thesis now opens up new paths not only for detailed studies of the observed phenomena, but also for the exploration of new features. In this concluding chapter we present some ideas for future investigations.

Universal dynamics of non-linear excitations

The observed universal phenomenon featured constant spin length in the transversal spin plane and excitations in the Larmor phase. However, we already noted that for specific initial conditions, i.e. a spin wave with short wavelength, we are able to produce non-linear excitations in the transversal spin. Those were found to be characterized by a reduction of spin length and a jump in the Larmor phase. In numerical simulations we observed that these excitations can lead to new universal phenomena with different scaling exponents [132]. Tuning the wavelength to change the number of produced excitations, we, however, came across an unexpected behaviour: in the experiments the non-linear excitations tend to move towards the edges of the harmonic trap, where they stop and decay. This raises the question of the lifetime of these defects, especially employing homogeneous box-like trapping potentials. Using arguments based on the similarity with solitonic excitations, a system closer to a one-dimensional situation should exhibit longer lifetimes. Thus, it would be advantageous to bring the system closer to being one-dimensional by lowering the atom number or increasing the transversal trapping confinement.

Trapping potentials and local control

Throughout this thesis, we evaluated only the central region of the harmonic trapping potential in order to reduce the change in atom number in the evaluation region. It would be advantageous to directly employ a box-like trapping potential. In our experiment, we have already implemented a setup containing an acusto-optical deflector (AOD) which allows the reflection of light through the imaging objective onto the atoms [152]. This gives the possibility to shine blue detuned light on the edges of the harmonic trap effectively generating walls for a box-like trapping potential. In this trapping potential, one can now investigate universal dynamics and look for phenomena emerging when engineering different initial conditions, for example featuring non-linear excitations.

The AOD not only allows for creating a box-like potential but also for local control of the spin degree of freedom: using light at the magic wavelength and performing amplitude modulation with the Larmor frequency one can employ local spin rotations [153]. This opens the possibility for creating new initial conditions. Further, a controlled generation of non-linear excitations is feasible, paving a way for a microscopic study of their inherent properties.

Statistical significance

A big challenge for future experiments is the amount of statistics necessary for reliably estimating higher order correlation functions. Quantitative tests of predictions, e.g. the full quantum evolution equation, will only be possible with a significantly higher number of measurements. In our case, the factor preventing us from employing more statistics is the cycle time of the experiment (about $\sim 35\,\mathrm{s}$). Considering the long evolution times, one might gain a factor of two by using an all optical setup and thus having faster condensation. However, the more promising ansatz is to do many experiments at once by using for example a one-dimensional lattice of tubes or an array of waveguides created by an AOD. Finding creative and practicable solutions like those is necessary for rendering correlation functions a valuable concept for characterizing many-body systems.

Studying thermalization

In the beginning, we introduced universal dynamics as a transient phenomenon on the way to thermalization. The achieved long evolution times in the experiment may give access to a regime approaching thermal equilibrium. An ansatz for probing this might be the observation that the fluctuation-dissipation theorem is broken in the vicinity of a non-thermal fixed point [94]. So probing this relation can give insights whether the system has already thermalized. However, this theorem is usually formulated based on unequal time correlation functions hard to access experimentally. This directly implies two challenges, one on the experimental and one on the theoretical side: Experimentally, it would be of great interest to find general schemes measuring unequal time correlation functions which would have also direct applications to other problems as for example studying information scrambling [154]. On the theoretical side a formulation of the fluctuation-dissipation theorem in terms of equal time correlation functions would be desirable.

The quantum effective action might be a new tool in this direction as in thermal equilibrium it is indeed connected to the microscopic Hamiltonian [91]. Together with enhanced statistical significance this might enable a detailed study of the thermalization process.

Appendix A

Details on Bogoliubov theory

In this section we give an intuitive picture of the operators defined for studying the Bogoliubov modes around the transversal spin in the easy-plane ferromagnetic phase. Further we show how the $\hat{F}_z$ operator is expressed in the Bogoliubov operators found in the demixing case.

A.1 Bogoliubov modes in the easy-plane ferromagnetic phase

For an elegant description of the excitations around the easy-plane ferromagnetic ground state we introduced in chapter 7 the following three operators

$$\hat{a}_{k,d} = \frac{\sin\theta}{\sqrt{2}}\left(\hat{a}_{k,1} + \hat{a}_{k,-1}\right) + \cos\theta\hat{a}_{k,0} \tag{A.1}$$

$$\hat{a}_{k,\theta} = \frac{\cos\theta}{\sqrt{2}}\left(\hat{a}_{k,1} + \hat{a}_{k,-1}\right) - \sin\theta\hat{a}_{k,0} \tag{A.2}$$

$$\hat{a}_{k,f_z} = \frac{1}{\sqrt{2}}\left(\hat{a}_{k,1} - \hat{a}_{k,-1}\right) . \tag{A.3}$$

Here, we want to argue in the classical field limit that the mode $\hat{a}_{k,\theta}$ is connected to spin length excitations and the mode $\hat{a}_{k,f_z}$ is connected to Larmor phase excitations. This is important for justifying the presented mexican hat picture.

In the classical field limit we replace the operators of the three hyperfine states by c-numbers (see Eq. (6.3)):

$$\hat{a}_{k,\pm1} \rightarrow \sqrt{N_{\pm1}}\mathrm{e}^{-i(\phi_{\pm1}+\delta\phi_{\pm1})} = \frac{\sin\theta}{\sqrt{2}}\mathrm{e}^{-i(\phi_{\pm1}+\delta\phi_{\pm1})} \tag{A.4}$$

$$\hat{a}_{k,0} \rightarrow \sqrt{N_0}\mathrm{e}^{-i(\phi_0+\delta\phi_0)} = \cos\theta\mathrm{e}^{-i(\phi_0+\delta\phi_0)} \tag{A.5}$$

where $\phi_i = 0\,(i = 0, \pm 1)$ for a spin pointing in x-direction and we introduced phase fluctuations $\delta\phi_i\,(i = 0, \pm 1)$. With this we find that

$$\begin{aligned} \hat{a}_{k,\theta} &\rightarrow \frac{\cos\theta\sin\theta}{2}\left(\mathrm{e}^{-i\delta\phi_{+1}} + \mathrm{e}^{-i\delta\phi_{-1}} - 2\mathrm{e}^{-i\delta\phi_0}\right) && \text{(A.6)} \\ &\simeq \frac{i\cos\theta\sin\theta}{2}\left(\delta\phi_{+1} + \delta\phi_{-1} - 2\delta\phi_0\right) && \text{(A.7)} \\ &\simeq \frac{i\cos\theta\sin\theta}{2}\delta\phi_S\,, && \text{(A.8)} \end{aligned}$$

where we used $\mathrm{e}^x \simeq 1 + x$ assuming small phase fluctuations $\delta\phi_i\,(i = 0, \pm 1)$ around the ground state. The phase difference $\delta\phi_S = \delta\phi_{+1} + \delta\phi_{-1} - 2\delta\phi_0$ is the spinor phase which changes the length of a spin in the transversal spin plane for fixed populations [155]. We analogously find that

$$\begin{aligned} \hat{a}_{k,f_z} &\rightarrow \frac{\sin\theta}{2}\left(\mathrm{e}^{-i\delta\phi_{+1}} - \mathrm{e}^{-i\delta\phi_{-1}}\right) && \text{(A.9)} \\ &\simeq -\frac{i\sin\theta}{2}\left(\delta\phi_{+1} - \delta\phi_{-1}\right) && \text{(A.10)} \\ &\simeq -\frac{i\sin\theta}{2}\delta\phi_L\,. && \text{(A.11)} \end{aligned}$$

So the $\hat{a}_{k,f_z}$ mode is connected to fluctuations of the Larmor phase $\delta\phi_L = \delta\phi_{+1} - \delta\phi_{-1}$. The found gapless dispersion relation for $\hat{a}_{k,f_z}$ and the gapped dispersion for $\hat{a}_{k,\theta}$ are in accordance with the mexican hat picture.

A.2 Demixing instability

For the demixing instability we introduced the Bogoliubov quasi-particle operator

$$\hat{b}_{k,-1} = u_{k,-}\frac{\hat{a}_{k,1} - \hat{a}_{k,-1}}{\sqrt{2}} + v_{k,-}\frac{\hat{a}^\dagger_{-k,1} - \hat{a}^\dagger_{-k,-1}}{\sqrt{2}} \tag{A.12}$$

with an most unstable momentum mode $k_{\mathrm{mu}} = \frac{\sqrt{2mhn|c_1|}}{h}$. In the presented experimental study we measured the F_z operator which is expressed in the original particle operator as $\hat{F}_z = \hat{a}^\dagger_{k,+1}\hat{a}_{k,+1} - \hat{a}^\dagger_{k,-1}\hat{a}_{k,-1}$. For obtaining an expectation for its unstable momentum modes we here express it in terms of the Bogoliubov operators.

It is necessary to introduce an additional, not yet discussed, Bogoliubov mode to invert the transformation. It reads

$$\hat{b}_{k,+1} = u_{k,+}\frac{\hat{a}_{k,1} + \hat{a}_{k,-1}}{\sqrt{2}} + v_{k,+}\frac{\hat{a}^\dagger_{-k,1} + \hat{a}^\dagger_{-k,-1}}{\sqrt{2}} \tag{A.13}$$

and describes density excitations in the two condensates in $m_F = \pm 1$ (for all details see [116]). Inverting the Bogoliubov transformation we find

$$\begin{aligned} \hat{a}^\dagger_{k,+1} &= \frac{1}{\sqrt{2}}\left(u_{k,+}\hat{b}^\dagger_{k,+} - v_{k,+}\hat{b}_{-k,+} + u_{k,-}\hat{b}^\dagger_{k,-} - v_{k,-}\hat{b}_{-k,-}\right) && \text{(A.14)} \\ \hat{a}^\dagger_{k,-1} &= \frac{1}{\sqrt{2}}\left(u_{k,+}\hat{b}^\dagger_{k,+} - v_{k,+}\hat{b}_{-k,+} - u_{k,-}\hat{b}^\dagger_{k,-} + v_{k,-}\hat{b}_{-k,-}\right)\,. && \text{(A.15)} \end{aligned}$$

Inserting these relations into the definition of $\hat{F}_z$ we obtain the final result:

$$\begin{aligned}\hat{F}_z = \sqrt{2}\Big\{ &\Big(u^*_{k,+}u_{k,-}\hat{b}^\dagger_{k,+}\hat{b}_{k,-} + u_{k,+}u^*_{k,-}\hat{b}^\dagger_{k,-}\hat{b}_{k,+}\Big) \\ &+ \Big(v^*_{k,+}v_{k,-}\hat{b}^\dagger_{k,+}\hat{b}_{k,-} + v_{k,+}v^*_{k,-}\hat{b}^\dagger_{k,-}\hat{b}_{k,+}\Big)\Big\}\end{aligned} \tag{A.16}$$

The mode $\hat{b}_{k,+}$ is not unstable and all occupation is in the condensate mode $k = 0$. Thus we see that $\hat{F}_z$ is linear in the unstable mode $\hat{b}_{k,-}$ and we expect the most unstable mode growing in $\hat{F}_z$ to be $k_{\mathrm{mu}} = \frac{\sqrt{2mhn|c_1|}}{h}$.

Appendix B

Additional plots on universal dynamics

In this appendix we give supplementary plots to the observation of universal dynamics in chapter 8. In Fig. B.1 we show the correlation functions $f_\theta(k)$ in the scaling regime for all momenta accessible in the experiment. We observe that the data collapses only in the infrared up to momenta $\sim 0.04\mu\mathrm{m}^{-1}$.

In Figures B.2, B.3 and B.4 we show the correlation functions $f_\theta(k)$ for the three different initial conditions. In contrast to Fig. 8.10, the optimal values found for each initial condition are used for rescaling (see inset of Fig. 8.10).

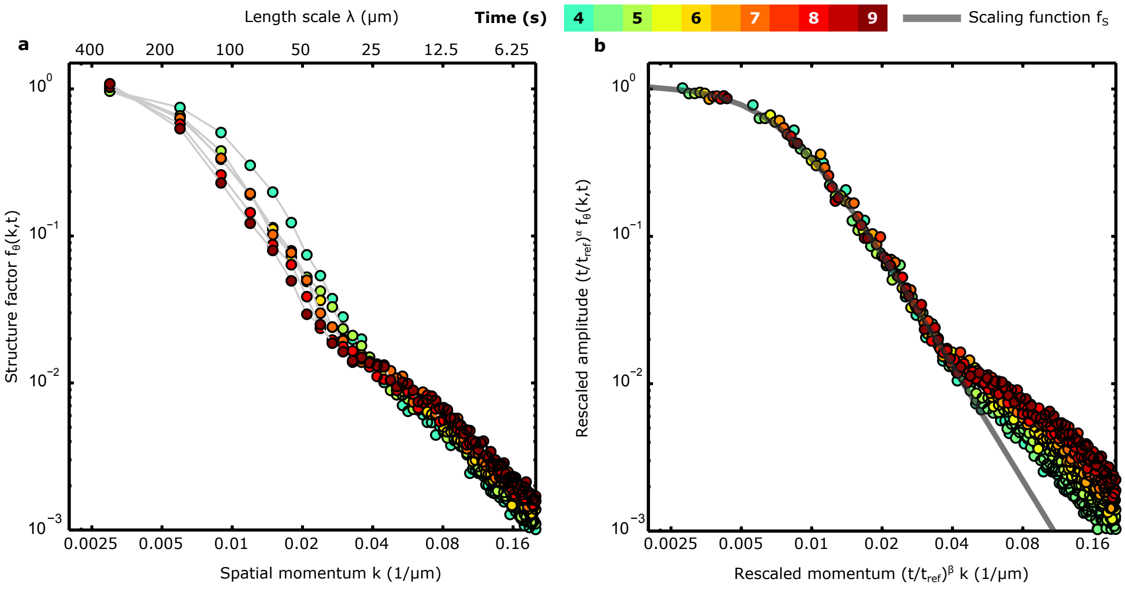

Figure B.1: **Rescaled spectra for all momenta for polar initial condition.**

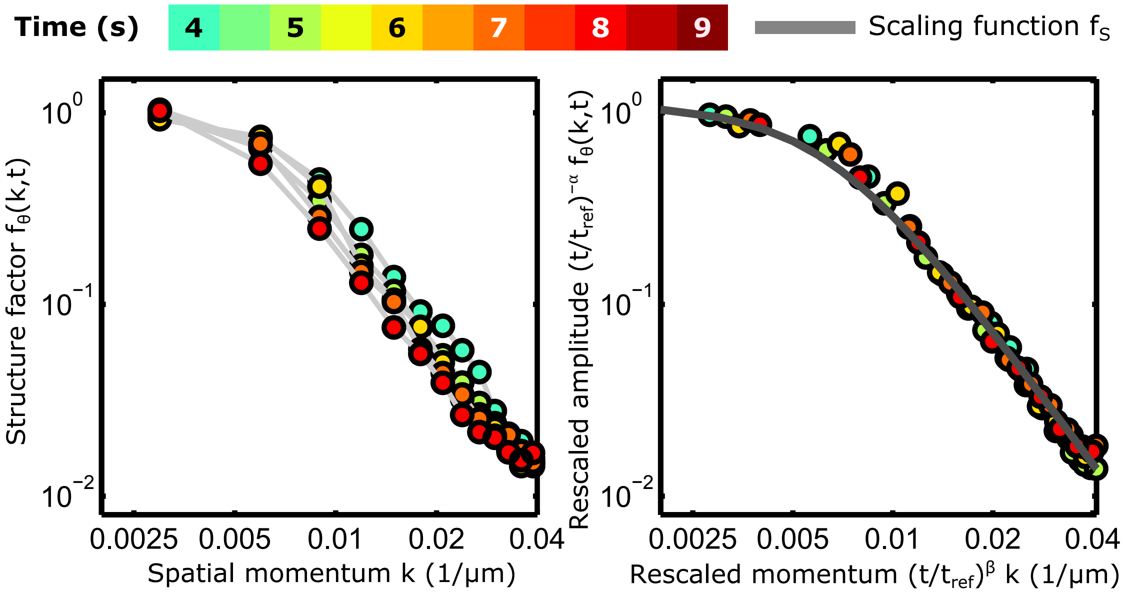

Figure B.2: **Universal dynamics of initial condition 1.**

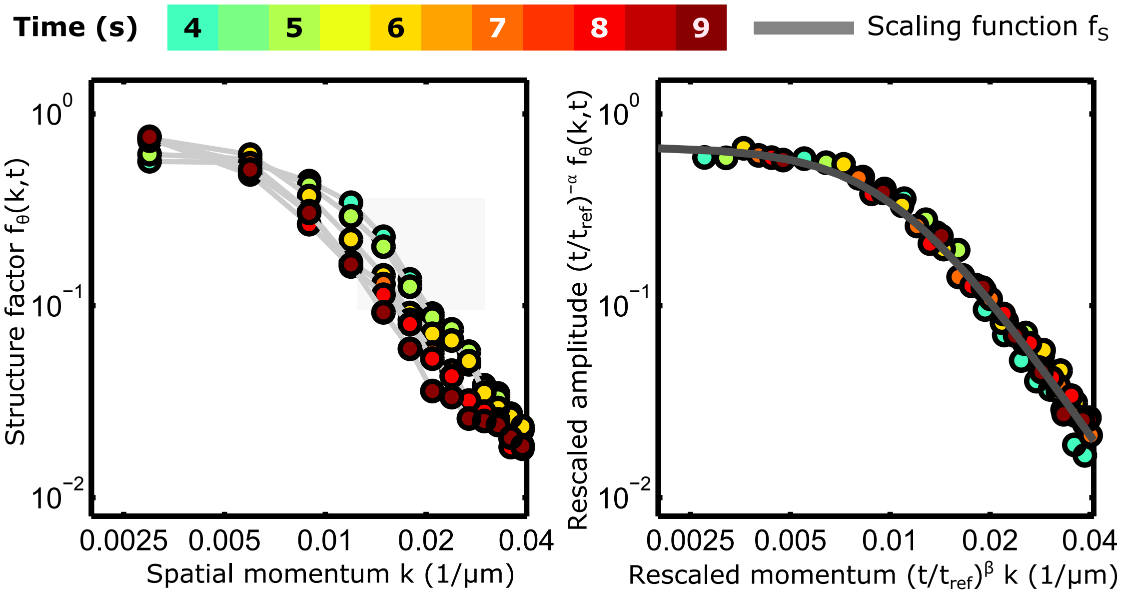

Figure B.3: **Universal dynamics of initial condition 2.**

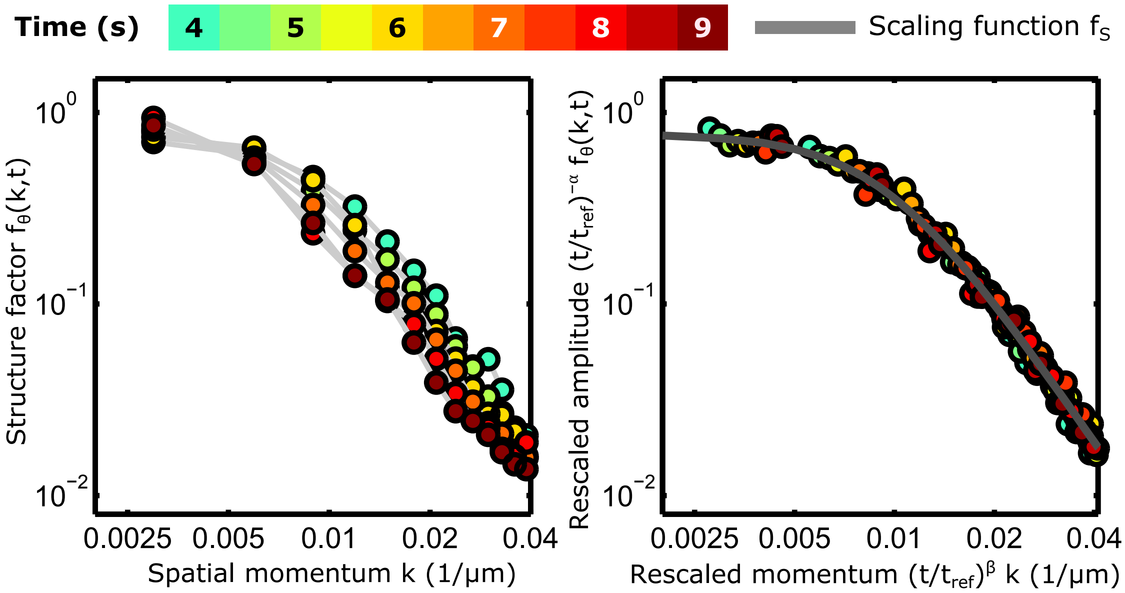

Figure B.4: **Universal dynamics of initial condition 3.**

Appendix C

Reduction to momentum conserving objects

In the main text we only show momentum conserving diagonals of the 1PI correlators. In principle the identification of the momentum conserving structure yields a reduction of the dimensionality of the objects by one. This means we can define new objects $\widetilde{\Gamma}_t^{(2)}(p_1)$ and $\widetilde{\Gamma}_t^{(4)}(p_1, p_2, p_3)$ which are defined by (with d = 1)

$$\Gamma_t^{(2)}(p_1, p_2) \equiv (2\pi)\, \delta\left(p_1 + p_2\right) \widetilde{\Gamma}_t^{(2)}(p_1) \tag{C.1}$$

$$\Gamma_t^{(4)}(p_1, p_2, p_3, p_4) \equiv (2\pi)\, \delta\left(p_1 + p_2 + p_3 + p_4\right) \widetilde{\Gamma}_t^{(4)}(p_1, p_2, p_3)\,. \tag{C.2}$$

The δ-function becomes important when comparing results, especially scaling, for systems with different volumes. For example looking at the momentum conserving diagonal of $\Gamma^{(2)}$ we find

$$\Gamma_t^{(2)}(p, -p) = 2\pi\, \delta(0)\, \widetilde{\Gamma}_t^{(2)}(p) = V\, \widetilde{\Gamma}_t^{(2)}(p)\,. \tag{C.3}$$

For rescaling of the correlators we have to take care as

$$\begin{aligned}
\Gamma_t^{(2)}(p_1, p_2) &= t^a \Gamma_S^{(2)}(t^\beta p_1, t^\beta p_2) && \text{(C.4)}\\
&= t^a (2\pi)\, \delta\left(t^\beta (p_1 + p_2)\right) \widetilde{\Gamma}_S\left(t^\beta p\right) && \text{(C.5)}\\
&= t^a (2\pi)\, t^{-\beta} \delta\left((p_1 + p_2)\right) \widetilde{\Gamma}_S\left(t^\beta p\right) && \text{(C.6)}\\
& && \text{(C.7)}
\end{aligned}$$

with the scaling function carrying subscript S. It follows that

$$\widetilde{\Gamma}_t\,(p) = t^{a-\beta} \widetilde{\Gamma}_S\left(t^\beta p\right). \tag{C.8}$$

We see that we cannot infer the “right” value for α from the scaling of the two-dimensional object as its amplitude scales with $a = \alpha + \beta \neq \alpha$. Here, we keep the length of the evaluation region (“volume”) fixed and with that just plot the obtained results. In this work we analyse only relative values between different momenta and times, keeping everything else fixed.

Bibliography

[1] Dowling, J. P. & Milburn, G. J. Quantum technology: the second quantum revolution. *Philosophical Transactions of the Royal Society of London. Series A: Mathematical, Physical and Engineering Sciences* **361**, 1655–1674 (2003).

[2] Frisch, U. & Kolmogorov, A. *Turbulence: the legacy of AN Kolmogorov* (Cambridge University Press, 1995).

[3] Manohar, A. V. Effective field theories. In *Perturbative and nonperturbative aspects of quantum field theory*, 311–362 (Springer, 1977).

[4] Navier, C. Mémoire sur les lois du mouvement des fluides. *Mémoires de l'Académie Royale des Sciences de l'Institut de France* **6**, 389–440 (1823).

[5] Schäfer, T. & Teaney, D. Nearly perfect fluidity: from cold atomic gases to hot quark gluon plasmas. *Reports on Progress in Physics* **72**, 126001 (2009).

[6] Zinn-Justin, J. *Quantum Field Theory and Critical Phenomena* (Clarendon Press, Oxford, 2002).

[7] Altland, A. & Simons, B. D. *Condensed matter field theory* (Cambridge university press, 2010).

[8] Wilson, K. G. The renormalization group: Critical phenomena and the Kondo problem. *Rev. Mod. Phys.* **47**, 773–840 (1975).

[9] Wilson, K. G. The renormalization group and critical phenomena. *Reviews of Modern Physics* **55**, 583 (1983).

[10] D'Alessio, L., Kafri, Y., Polkovnikov, A. & Rigol, M. From quantum chaos and eigenstate thermalization to statistical mechanics and thermodynamics. *Advances in Physics* **65**, 239–362 (2016).

[11] Braun-Munzinger, P. & Stachel, J. The quest for the quark–gluon plasma. *Nature* **448**, 302 (2007).

[12] Heinz, U. & Snellings, R. Collective flow and viscosity in relativistic heavy-ion collisions. *Annual Review of Nuclear and Particle Science* **63**, 123–151 (2013).

[13] Andronic, A., Braun-Munzinger, P., Redlich, K. & Stachel, J. Decoding the phase structure of QCD via particle production at high energy. *Nature* **561**, 321–330 (2018).

[14] Ketterle, W., Durfee, D. S. & Stamper-Kurn, D. Making, probing and understanding Bose-Einstein condensates. *arXiv preprint cond-mat/9904034* (1999).

[15] Berges, J., Rothkopf, A. & Schmidt, J. Nonthermal fixed points: effective weak coupling for strongly correlated systems far from equilibrium. *Phys. Rev. Lett.* **101**, 041603 (2008).

[16] Nowak, B., Sexty, D. & Gasenzer, T. Superfluid turbulence: Nonthermal fixed point in an ultracold Bose gas. *Phys. Rev. B* **84**, 020506(R) (2011).

[17] Navon, N., Gaunt, A. L., Smith, R. P. & Hadzibabic, Z. Emergence of a turbulent cascade in a quantum gas. *Nature* **539**, 72–75 (2016).

[18] Prüfer, M., Kunkel, P., Strobel, H., Lannig, S., Linnemann, D., Schmied, C.-M., Berges, J., Gasenzer, T. & Oberthaler, M. K. Observation of universal dynamics in a spinor Bose gas far from equilibrium. *Nature* **563**, 217–220 (2018).

[19] Erne, S., Bücker, R., Gasenzer, T., Berges, J. & Schmiedmayer, J. Universal dynamics in an isolated one-dimensional Bose gas far from equilibrium. *Nature* **563**, 225–229 (2018).

[20] Navon, N., Eigen, C., Zhang, J., Lopes, R., Gaunt, A. L., Fujimoto, K., Tsubota, M., Smith, R. P. & Hadzibabic, Z. Synthetic dissipation and cascade fluxes in a turbulent quantum gas. *Science* **366**, 382–385 (2019).

[21] Jordan, S. P., Lee, K. S. & Preskill, J. Quantum algorithms for quantum field theories. *Science* **336**, 1130–1133 (2012).

[22] Polkovnikov, A., Sengupta, K., Silva, A. & Vengalattore, M. Colloquium: Nonequilibrium dynamics of closed interacting quantum systems. *Rev. Mod. Phys.* **83**, 863–883 (2011).

[23] Sachdev, S. Quantum phase transitions. *Handbook of Magnetism and Advanced Magnetic Materials* (2007).

[24] Bitko, D., Rosenbaum, T. F. & Aeppli, G. Quantum critical behavior for a model magnet. *Phys. Rev. Lett.* **77**, 940–943 (1996).

[25] Greiner, M., Mandel, O., Esslinger, T., Hänsch, T. W. & Bloch, I. Quantum phase transition from a superfluid to a Mott insulator in a gas of ultracold atoms. *Nature* **415**, 39 (2002).

[26] Sadler, L. E., Higbie, J. M., Leslie, S. R., Vengalattore, M. & Stamper-Kurn, D. M. Spontaneous symmetry breaking in a quenched ferromagnetic spinor Bose-Einstein condensate. *Nature* **443**, 312–315 (2006).

[27] Roch, N., Florens, S., Bouchiat, V., Wernsdorfer, W. & Balestro, F. Quantum phase transition in a single-molecule quantum dot. *Nature* **453**, 633 (2008).

[28] Baumann, K., Guerlin, C., Brennecke, F. & Esslinger, T. Dicke quantum phase transition with a superfluid gas in an optical cavity. *Nature* **464**, 1301 (2010).

[29] Calabrese, P. & Cardy, J. Quantum quenches in extended systems. *Journal of Statistical Mechanics: Theory and Experiment* **2007**, P06008 (2007).

[30] Bloch, I., Dalibard, J. & Nascimbène, S. Quantum simulations with ultracold quantum gases. *Nat. Phys.* **8**, 267–276 (2012).

[31] Rigol, M., Dunjko, V. & Olshanii, M. Thermalization and its mechanism for generic isolated quantum systems. *Nature* **452**, 854–858 (2008).

[32] Mori, T., Ikeda, T. N., Kaminishi, E. & Ueda, M. Thermalization and prethermalization in isolated quantum systems: a theoretical overview. *Journal of Physics B: Atomic, Molecular and Optical Physics* **51**, 112001 (2018).

[33] Kaufman, A. M., Tai, E. M., Lukin, A., Rispoli, M., Schittko, R., Preiss, P. M. & Greiner, M. Quantum thermalization through entanglement in an isolated many-body system. *Science* **353**, 794–800 (2016).

[34] Rigol, M., Dunjko, V., Yurovsky, V. & Olshanii, M. Relaxation in a completely integrable many-body quantum system: An ab initio study of the dynamics of the highly excited states of 1d lattice hard-core bosons. *Phys. Rev. Lett.* **98**, 050405 (2007).

[35] Calabrese, P., Essler, F. H. & Fagotti, M. Quantum quench in the transverse-field ising chain. *Phy. Rev. Lett.* **106**, 227203 (2011).

[36] Berges, J., Borsányi, S. & Wetterich, C. Prethermalization. *Phys. Rev. Lett.* **93**, 142002 (2004).

[37] Kollar, M., Wolf, F. A. & Eckstein, M. Generalized gibbs ensemble prediction of prethermalization plateaus and their relation to nonthermal steady states in integrable systems. *Phys. Rev. B* **84**, 054304 (2011).

[38] Gring, M., Kuhnert, M., Langen, T., Kitagawa, T., Rauer, B., Schreitl, M., Mazets, I., Smith, D. A., Demler, E. & Schmiedmayer, J. Relaxation and Prethermalization in an Isolated Quantum System. *Science* **337**, 1318–1322 (2012).

[39] Langen, T., Erne, S., Geiger, R., Rauer, B., Schweigler, T., Kuhnert, M., Rohringer, W., Mazets, I. E., Gasenzer, T. & Schmiedmayer, J. Experimental observation of a generalized Gibbs ensemble. *Science* **348**, 207–211 (2015).

[40] Rauer, B., Erne, S., Schweigler, T., Cataldini, F., Tajik, M. & Schmiedmayer, J. Recurrences in an isolated quantum many-body system. *Science* **360**, 307–310 (2018).

[41] Schreiber, M., Hodgman, S. S., Bordia, P., Lüschen, H. P., Fischer, M. H., Vosk, R., Altman, E., Schneider, U. & Bloch, I. Observation of many-body localization of interacting fermions in a quasirandom optical lattice. *Science* **349**, 842–845 (2015).

[42] Smith, J., Lee, A., Richerme, P., Neyenhuis, P., B. Hess, Hauke, P., Heyl, M., Huse, D. & Monroe, C. Many-body localization in a quantum simulator with programmable random disorder. *Nature Physics* **12**, 907–911 (2016).

[43] Lukin, A., Rispoli, M., Schittko, R., Tai, M. E., Kaufman, A. M., Choi, S., Khemani, V., Léonard, J. & Greiner, M. Probing entanglement in a many-body–localized system. *Science* **364**, 256–260 (2019).

[44] Rispoli, M., Lukin, A., Schittko, R., Kim, S., Tai, M. E., Léonard, J. & Greiner, M. Quantum critical behaviour at the many-body localization transition. *Nature* **573**, 385–389 (2019).

[45] Langen, T., Gasenzer, T. & Schmiedmayer, J. Prethermalization and universal dynamics in near-integrable quantum systems. *Journal of Statistical Mechanics: Theory and Experiment* **2016**, 064009 (2016).

[46] Schmied, C.-M., Mikheev, A. N. & Gasenzer, T. Non-thermal fixed points: Universal dynamics far from equilibrium. *arXiv preprint arXiv:1810.08143* (2018).

[47] Feigenbaum, M. Universality in complex discrete dynamics. Tech. Rep., LA-6816-PR, LASL Theoretical Division Annual Report July 1975 (1976).

[48] Kadanoff, L. P. Scaling and universality in statistical physics. *Physica A: Statistical Mechanics and its Applications* **163**, 1–14 (1990).

[49] Stauffer, D., Ferer, M. & Wortis, M. Universality of second-order phase transitions: The scale factor for the correlation length. *Phys. Rev. Lett.* **29**, 345–349 (1972).

[50] Hohenberg, P. C. & Halperin, B. I. Theory of dynamic critical phenomena. *Rev. Mod. Phys.* **49**, 435–479 (1977).

[51] Stanley, H. E. Scaling, universality, and renormalization: Three pillars of modern critical phenomena. *Rev. Mod. Phys.* **71**, S358–S366 (1999).

[52] Donner, T., Ritter, S., Bourdel, T., Öttl, A., Köhl, M. & Esslinger, T. Critical behavior of a trapped interacting bose gas. *Science* **315**, 1556–1558 (2007).

[53] Kibble, T. W. Topology of cosmic domains and strings. *Journal of Physics A: Mathematical and General* **9**, 1387 (1976).

[54] Zurek, W. H. Cosmological experiments in superfluid helium? *Nature* **317**, 505 (1985).

[55] Zurek, W. H., Dorner, U. & Zoller, P. Dynamics of a quantum phase transition. *Phys. Rev. Lett.* **95**, 105701 (2005).

[56] Navon, N., Gaunt, A. L., Smith, R. P. & Hadzibabic, Z. Critical dynamics of spontaneous symmetry breaking in a homogeneous bose gas. *Science* **347**, 167–170 (2015).

[57] Clark, L. W., Feng, L. & Chin, C. Universal space-time scaling symmetry in the dynamics of bosons across a quantum phase transition. *Science* **354**, 606–610 (2016).

[58] Anquez, M., Robbins, B. A., Bharath, H. M., Boguslawski, M., Hoang, T. M. & Chapman, M. S. Quantum Kibble-Zurek Mechanism in a Spin-1 Bose-Einstein Condensate. *Phys. Rev. Lett.* **116**, 155301 (2016).

[59] Keesling, A. *et al.* Quantum Kibble–Zurek mechanism and critical dynamics on a programmable Rydberg simulator. *Nature* **568**, 207 (2019).

[60] Bray, A. J. Theory of phase-ordering kinetics. *Advance in Physics* **51**, 481–587 (2002).

[61] Kofman, L., Linde, A. & Starobinsky, A. A. Reheating after Inflation. *Phys. Rev. Lett.* **73**, 3195–3198 (1994).

[62] Micha, R. & Tkachev, I. I. Relativistic Turbulence: A Long Way from Preheating to Equilibrium. *Phys. Rev. Lett.* **90**, 121301 (2003).

[63] Baier, R., Mueller, A. H., Schiff, D. & Son, D. "Bottom-up" thermalization in heavy ion collisions. *Phys. Lett. B* **502**, 51–58 (2001).

[64] Berges, J., Boguslavski, K., Schlichting, S. & Venugopalan, R. Turbulent thermalization process in heavy-ion collisions at ultrarelativistic energies. *Phys. Rev. D* **89**, 074011 (2014).

[65] Lamacraft, A. Quantum Quenches in a Spinor Condensate. *Phys. Rev. Lett.* **98**, 160404 (2007).

[66] Barnett, R., Polkovnikov, A. & Vengalattore, M. Prethermalization in quenched spinor condensates. *Phys. Rev. A* **84**, 023606 (2011).

[67] Hofmann, J., Natu, S. S. & Das Sarma, S. Coarsening Dynamics of Binary Bose Condensates. *Phys. Rev. Lett.* **113**, 095702 (2014).

[68] Piñeiro Orioli, A., Boguslavski, K. & Berges, J. Universal self-similar dynamics of relativistic and nonrelativistic field theories near nonthermal fixed points. *Phys. Rev. D* **92**, 025041 (2015).

[69] Williamson, L. A. & Blakie, P. B. Universal Coarsening Dynamics of a Quenched Ferromagnetic Spin-1 Condensate. *Phys. Rev. Lett.* **116**, 025301 (2016).

[70] Bourges, A. & Blakie, P. B. Different growth rates for spin and superfluid order in a quenched spinor condensate. *Phys. Rev. A* **95**, 023616 (2017).

[71] Schmied, C.-M., Gasenzer, T. & Blakie, P. B. Violation of single-length-scaling dynamics via spin vortices in an isolated spin-1 Bose gas. *Phys. Rev. A* **100**, 033603 (2019).

[72] Williamson, L. A. & Blakie, P. B. Anomalous phase ordering of a quenched ferromagnetic superfluid. *SciPost Phys.* **7**, 29 (2019).

[73] Cramer, M., Plenio, M. B., Flammia, S. T., Somma, R., Gross, D., Bartlett, S. D., Landon-Cardinal, O., Poulin, D. & Liu, Y.-K. Efficient quantum state tomography. *Nature communications* **1**, 149 (2010).

[74] Gross, D., Liu, Y.-K., Flammia, S. T., Becker, S. & Eisert, J. Quantum state tomography via compressed sensing. *Phys. Rev. Lett.* **105**, 150401 (2010).

[75] Lanyon, B. *et al.* Efficient tomography of a quantum many-body system. *Nature Physics* **13**, 1158 (2017).

[76] Schweigler, T., Kasper, V., Erne, S., Mazets, I., Rauer, B., Cataldini, F., Langen, T., Gasenzer, T., Berges, J. & Schmiedmayer, J. Experimental characterization of a quantum many-body system via higher-order correlations. *Nature* **545**, 323–326 (2017).

[77] Hodgman, S. S., Khakimov, R. I., Lewis-Swan, R. J., Truscott, A. G. & Kheruntsyan, K. V. Solving the quantum many-body problem via correlations measured with a momentum microscope. *Phys. Rev. Lett.* **118**, 240402 (2017).

[78] Preiss, P. M., Becher, J. H., Klemt, R., Klinkhamer, V., Bergschneider, A., Defenu, N. & Jochim, S. High-Contrast Interference of Ultracold Fermions. *Phys. Rev. Lett.* **122**, 143602 (2019).

[79] Matthew, D. *et al. Quantum Gases: Finite temperature and non-equilibrium dynamics*, vol. 1 (World Scientific, 2013).

[80] Rammer, J. *Quantum field theory of non-equilibrium states* (Cambridge University Press, 2007).

[81] Abrikosov, A. A., Gorkov, L. P. & Dzyaloshinski, I. E. *Methods of quantum field theory in statistical physics* (Courier Corporation, 2012).

[82] Schrödinger, E. An undulatory theory of the mechanics of atoms and molecules. *Physical review* **28**, 1049 (1926).

[83] Weinberg, S. *The quantum theory of fields* (Cambridge University Press, 1995).

[84] Amit, D. J. & Martin-Mayor, V. *Field Theory, the Renormalization Group, and Critical Phenomena: Graphs to Computers Third Edition* (World Scientific Publishing Company, 2005).

[85] Bodet, C., Kronenwett, M., Nowak, B., Sexty, D. & Gasenzer, T. Functional-integral approach to non-equilibrium quantum many-body dynamics. In *Quantum Gases: Finite Temperature and Non-Equilibrium Dynamics*, 241–255 (World Scientific, 2013).

[86] Prüfer, M., Zache, T. V., Kunkel, P., Lannig, S., Bonnin, A., Strobel, H., Berges, J. & Oberthaler, M. K. Experimental extraction of the quantum effective action for a non-equilibrium many-body system. *arXiv preprint arXiv:1909.05120* (2019).

[87] Wetterich, C. Nonequilibrium time evolution in quantum field theory. *Phys. Rev. E* **56**, 2687 (1997).

[88] Polkovnikov, A. Phase space representation of quantum dynamics. *Annals of Physics* **325**, 1790–1852 (2010).

[89] Hillery, M., O'Connell, R. F., Scully, M. O. & Wigner, E. P. Distribution functions in physics: fundamentals. *Physics Reports* **106**, 121–167 (1984).

[90] Walz, R., Boguslavski, K. & Berges, J. Large-N kinetic theory for highly occupied systems. *Phys. Rev. D* **97**, 116011 (2018).

[91] Zache, T. V., Schweigler, T., Erne, S., Schmiedmayer, J. & Berges, J. Extracting the field theory description of a quantum many-body system from experimental data. *arXiv preprint arXiv:1909.12815* (2019).

[92] Berges, J. & Mesterhazy, D. Introduction to the nonequilibrium functional renormalization group. *Nuclear Physics B-Proceedings Supplements* **228**, 37–60 (2012).

[93] Gasenzer, T., Keßler, S. & Pawlowski, J. M. Far-from-equilibrium quantum many-body dynamics. *The European Physical Journal C* **70**, 423–443 (2010).

[94] Piñeiro Orioli, A. & Berges, J. Breaking the fluctuation-dissipation relation by universal transport processes. *Phys. Rev. Lett.* **122**, 150401 (2019).

[95] Nowak, B., Schole, J. & Gasenzer, T. Universal dynamics on the way to thermalization. *New journal of physics* **16**, 093052 (2014).

[96] Karl, M. & Gasenzer, T. Strongly anomalous non-thermal fixed point in a quenched two-dimensional bose gas. *New Journal of Physics* **19**, 093014 (2017).

[97] Schmied, C.-M., Mikheev, A. N. & Gasenzer, T. Prescaling in a Far-from-Equilibrium Bose Gas. *Phys. Rev. Lett.* **122**, 170404 (2019).

[98] Feynman, R. P. Simulating physics with computers. *International journal of theoretical physics* **21**, 467–488 (1982).

[99] Georgescu, I. M., Ashhab, S. & Nori, F. Quantum simulation. *Rev. Mod. Phys.* **86**, 153–185 (2014).

[100] Nielsen, M. A. & Chuang, I. Quantum computation and quantum information (2002).

[101] Lloyd, S. Universal quantum simulators. *Science* 1073–1078 (1996).

[102] Gross, C. & Bloch, I. Quantum simulations with ultracold atoms in optical lattices. *Science* **357**, 995–1001 (2017).

[103] Horsman, C., Stepney, S., Wagner, R. C. & Kendon, V. When does a physical system compute? *Proceedings of the Royal Society A: Mathematical, Physical and Engineering Sciences* **470**, 20140182 (2014).

[104] Berges, J., Boguslavski, K., Mace, M. & Pawlowski, J. M. Gauge-invariant condensation in the nonequilibrium quark-gluon plasma. *arXiv preprint arXiv:1909.06147* (2019).

[105] Weller, A. *Dynamics and Interaction of Dark Solitons in Bose-Einstein Condensates.* Ph.D. thesis, University Heidelberg (2009).

[106] Zibold, T. *Classical Bifurcation and Entanglement Generation in an Internal Bosonic Josephson Junction.* Ph.D. thesis, University Heidelberg (2012).

[107] Nicklas, E. *A new tool for miscibility control: Linear coupling.* Ph.D. thesis, University Heidelberg (2013).

[108] Muessel, W. *Spin Squeezing for Quantum-Enhanced Magnetometry with Bose-Einstein Condensates.* Ph.D. thesis, University Heidelberg (2014).

[109] Steck, D. A. Rubidium 87 D line data (2001).

[110] Stamper-Kurn, D. M. & Ueda, M. Spinor Bose gases: Symmetries, magnetism, and quantum dynamics. *Rev. Mod. Phys.* **85**, 1191–1244 (2013).

[111] Petrich, W., Anderson, M. H., Ensher, J. R. & Cornell, E. A. Stable, tightly confining magnetic trap for evaporative cooling of neutral atoms. *Physical Review Letters* **74**, 3352 (1995).

[112] Nicklas, E., Karl, M., Höfer, M., Johnson, A., Muessel, W., Strobel, H., Tomkovič, J., Gasenzer, T. & Oberthaler, M. K. Observation of Scaling in the Dynamics of a Strongly Quenched Quantum Gas. *Phys. Rev. Lett.* **115**, 245301 (2015).

[113] Dalfovo, F., Giorgini, S., Pitaevskii, L. P. & Stringari, S. Theory of Bose-Einstein condensation in trapped gases. *Reviews of Modern Physics* **71**, 463 (1999).

[114] Muessel, W., Strobel, H., Joos, M., Nicklas, E., Stroescu, I., Tomkovič, J., Hume, D. B. & Oberthaler, M. K. Optimized absorption imaging of mesoscopic atomic clouds. *Appl. Phys. B* **113**, 69–73 (2013).

[115] Linnemann, D. *Quantum-Enhanced Sensing Based on Time Reversal of Entangling Interactions* (Springer, 2018).

[116] Kawagushi, Y. & Ueda, M. Spinor Bose-Einstein condensates. *Phys. Rep.* **520**, 253–381 (2012).

[117] Hamley, C. D., Gerving, C. S., Hoang, T. M., Bookjans, E. M. & Chapman, M. S. Spin-nematic squeezed vacuum in a quantum gas. *Nat. Phys.* **8**, 305–308 (2012).

[118] Gerbier, F., Widera, A., Fölling, S., Mandel, O. & Bloch, I. Resonant control of spin dynamics in ultracold quantum gases by microwave dressing. *Phys. Rev. A* **73**, 041602(R) (2006).

[119] Kunkel, P., Prüfer, M., Lannig, S., Rosa-Medina, R., Bonnin, A., Gärttner, M., Strobel, H. & Oberthaler, M. K. Simultaneous Readout of Noncommuting Collective Spin Observables beyond the Standard Quantum Limit. *Phys. Rev. Lett.* **123**, 063603 (2019).

[120] Reinaudi, G., Lahaye, T., Wang, Z. & Guéry-Odelin, D. Strong saturation absorption imaging of dense clouds of ultracold atoms. *Optics letters* **32**, 3143–3145 (2007).

[121] Kunkel, P. *Splitting a Bose-Einstein condensate enables EPR steering and simultaneous readout of conjugate observables*. Ph.D. thesis, University Heidelberg (2019).

[122] Strobel, H. *Fisher Information and entanglementof non-Gaussian spin states*. Ph.D. thesis, Heidelberg University (2015).

[123] Mukerjee, S., Xu, C. & Moore, J. E. Dynamical models and the phase ordering kinetics of the $s = 1$ spinor condensate. *Phys. Rev. B* **76**, 104519 (2007).

[124] Kawaguchi, Y., Phuc, N. T. & Blakie, P. B. Finite-temperature phase diagram of a spin-1 Bose gas. *Physical Review A* **85**, 053611 (2012).

[125] Guzman, J., Jo, G.-B., Wenz, A. N., Murch, K. W., Thomas, C. K. & Stamper-Kurn, D. M. Long-time-scale dynamics of spin textures in a degenerate $F = 1$ ^{87}Rb spinor Bose gas. *Phys. Rev. A* **84**, 063625 (2011).

[126] Klempt, C., Topic, O., Gebreyesus, G., Scherer, M., Henninger, T., Hyllus, P., Ertmer, W., Santos, L. & Arlt, J. J. Multiresonant spinor dynamics in a Bose-Einstein condensate. *Phys. Rev. Lett.* **103**, 195302 (2009).

[127] Bogoljubov, N., Tolmachov, V. V. & Širkov, D. A new method in the theory of superconductivity. *Fortschritte der Physik* **6**, 605–682 (1958).

[128] Uchino, S., Kobayashi, M. & Ueda, M. Bogoliubov theory and Lee-Huang-Yang corrections in spin-1 and spin-2 Bose-Einstein condensates in the presence of the quadratic Zeeman effect. *Physical Review A* **81**, 063632 (2010).

[129] Schmied, C.-M., Gasenzer, T., Oberthaler, M. & Kevrekidis, P. Stability analysis of ground states in a one-dimensional trapped spin-1 Bose gas. *arXiv preprint arXiv:1905.03069* (2019).

[130] Leslie, S. R., Guzman, J., Vengalattore, M., Sau, J. D., Cohen, M. L. & Stamper-Kurn, D. M. Amplification of fluctuations in a spinor Bose-Einstein condensate. *Phys. Rev. A* **79**, 043631 (2009).

[131] Kevrekidis, P. G., Frantzeskakis, D. J. & Carretero-González, R. *Emergent nonlinear phenomena in Bose-Einstein condensates: theory and experiment*, vol. 45 (Springer Science & Business Media, 2007).

[132] Schmied, C.-M., Prüfer, M., Oberthaler, M. K. & Gasenzer, T. Bidirectional universal dynamics in a spinor bose gas close to a nonthermal fixed point. *Phys. Rev. A* **99**, 033611 (2019).

[133] Miller, R. G. The jackknife–a review. *Biometrika* **61**, 1–15 (1974).

[134] Berges, J. & Sexty, D. Bose-einstein condensation in relativistic field theories far from equilibrium. *Phys. Rev. Lett.* **108**, 161601 (2012).

[135] Nowak, B., Schole, J., Sexty, D. & Gasenzer, T. Nonthermal fixed points, vortex statistics, and superfluid turbulence in an ultracold bose gas. *Phys. Rev. A* **85**, 043627 (2012).

[136] Chantesana, I., Orioli, A. P. n. & Gasenzer, T. Kinetic theory of nonthermal fixed points in a Bose gas. *Phys. Rev. A* **99**, 043620 (2019).

[137] Boguslavski, K. & Orioli, A. P. Unraveling the nature of universal dynamics in $O(N)$ theories. *arXiv preprint arXiv:1911.04506* (2019).

[138] Berges, J., Boguslavski, K., Schlichting, S. & Venugopalan, R. Universality Far from Equilibrium: From Superfluid Bose Gases to Heavy-Ion Collisions. *Phys. Rev. Lett.* **114**, 061601 (2015).

[139] Bookjans, E. M., Vinit, A. & Raman, C. Quantum Phase Transition in an Antiferromagnetic Spinor Bose-Einstein Condensate. *Phys. Rev. Lett.* **107**, 195306 (2011).

[140] Vinit, A., Bookjans, E. M., Sá de Melo, C. A. R. & Raman, C. Antiferromagnetic spatial ordering in a quenched one-dimensional spinor gas. *Phys. Rev. Lett.* **110**, 165301 (2013).

[141] Fujimoto, K., Hamazaki, R. & Ueda, M. Flemish Strings of Magnetic Solitons and a Nonthermal Fixed Point in a One-Dimensional Antiferromagnetic Spin-1 Bose Gas. *Phys. Rev. Lett.* **122**, 173001 (2019).

[142] Symes, L. M. & Blakie, P. B. Nematic ordering dynamics of an antiferromagnetic spin-1 condensate. *Phys. Rev. A* **96**, 013602 (2017).

[143] Pimentel, R. F. R.-M. *Probing Long-Time Spin Dynamics in a ^{87}Rb Bose-Einstein Condensate*. Master's thesis, Heidelberg University (2018).

[144] Pitaevskii, L. & Stringari, S. *Bose-Einstein condensation and superfluidity*, vol. 164 (Oxford University Press, 2016).

[145] Kunkel, P., Prüfer, M., Strobel, H., Linnemann, D., Frölian, A., Gasenzer, T., Gärttner, M. & Oberthaler, M. K. Spatially distributed multipartite entanglement enables EPR steering of atomic clouds. *Science* **360**, 413–416 (2018).

[146] Wiener, N. *et al.* Generalized harmonic analysis. *Acta mathematica* **55**, 117–258 (1930).

[147] Mazeliauskas, A. & Berges, J. Prescaling and far-from-equilibrium hydrodynamics in the quark-gluon plasma. *Phys. Rev. Lett.* **122**, 122301 (2019).

[148] Domino, K., Gawron, P. & Pawela, Ł. Efficient computation of higher-order cumulant tensors. *SIAM Journal on Scientific Computing* **40**, A1590–A1610 (2018).

[149] Efron, B. Bootstrap methods: another look at the jackknife. In *Breakthroughs in statistics*, 569–593 (Springer, 1992).

[150] Anderson, T. W. An introduction to multivariate statistical analysis. Tech. Rep., Wiley New York (1962).

[151] Pitaevskii, L. & Lifshitz, E. *Physical kinetics*, vol. 10 (Butterworth-Heinemann, 2012).

[152] Frölian, A. *Implementation of local addressability in a Bose-Einstein condensate.* Master's thesis, Heidelberg University (2017).

[153] Marti, G. E. & Stamper-Kurn, D. Spinor Bose-Einstein gases. *Quantum Matter at Ultralow Temperatures* **191**, 221 (2016).

[154] Swingle, B., Bentsen, G., Schleier-Smith, M. & Hayden, P. Measuring the scrambling of quantum information. *Physical Review A* **94**, 040302 (2016).

[155] Lannig, S. *Experimental Control of a Spin-1 Bose-Einstein Condensate.* Master's thesis, Heidelberg University (2017).

“Mein Problem ist,
dass ich immer sehr selbstkritisch bin,
auch mir selbst gegenüber.”
Andreas Möller

Danksagung

Diese Arbeit hätte niemals das werden können, was sie heute ist, ohne mein Umfeld – bestehend aus vielen verschiedenen Leuten. Daher ist es mir eine große Freude, all jenen hier explizit zu danken!

Zuallererst möchte ich Markus danken, dass er mir von Beginn an dieses Projekt anvertraut hat. Ich habe in den letzten Jahren unglaublich viel von ihm gelernt, sowohl auf der experimentellen und theoretischen Ebene, als auch darüber, wie man ein Projekt vorantreibt - und wann der richtige Zeitpunkt für den Abschluss ist. Sein Wille, bei jeder Arbeit etwas Neues zu produzieren und den Dingen einen neuen Twist zu geben, erstaunt mich jeden Tag wieder. Außerdem hatte er trotz seiner vielen sonstigen Verpflichtungen immer Zeit für ein persönliches Gespräch.

Ganz besonders möchte ich auch Thomas danken. Von ihm durfte ich unglaublich viel über theoretische Dinge, vor allem Bogoliubov Theorie, lernen. Er hat immer eine offene Tür für eine spontane Diskussion und aus “Kann ich ganz kurz mal etwas fragen?” wird nicht selten eine mehrstündige Diskussion.

Jürgen danke ich für die interessanten Kollaborationen und die vielen Diskussionen zu Quantenfeldtheoriekonzepten.

Stefan Flörchinger danke ich für die Bereitschaft, das Zweitgutachten für meine Promotionsprüfung zu übernehmen.

Ohne das tolle Teamwork am BEC Experiment wäre diese Arbeit niemals in der Art und Weise möglich gewesen. Alle, die in den letzten Jahren Teil des Experiments waren, haben zum Gelingen beigetragen. Beginnend bei Wolfgang, der mich an meinen ersten Tagen eingearbeitet und mir schlussendlich mein Projekt übergeben hat. Helmut war immer Teil dieses Teams und wird es wohl auch immer bleiben. Seine Sicht auf komplizierte physikalische Zusammenhänge und sein schier unerschöpfliches Wissen zu experimentellen Details war und ist von großem Wert. Auch unsere Masterstudenten Anika und Rodrigo haben immer zu einer guten Atmosphäre in Büro und Labor beigetragen. Großer Dank gilt Stefan (oder Lannig)! Unvergessen ist für mich unser Auslandstelefonat während der Scalingmessung.

Ganz im Besonderen möchte ich mich bei Philipp bedanken! Es gibt wohl wenige Menschen mit denen ich in den letzten Jahren so viel Zeit verbracht habe. Du bist inzwischen nicht einfach nur ein Kollege, sondern auch ein guter Freund. Ich wusste immer, dass ich mich auf dich verlassen konnte und lange Freitagabende im Labor waren unterhaltsam ebenso wie unsere Kochabende (hier geht wohl auch ein Dank an

deinen jagenden Bruder). Deine besonnene und diplomatische Art war ein hilfreiches Korrektiv!

Ein großer Dank gebührt auch meinen zwei Theoretikern. Christian, ich finde es ganz wunderbar, dass wir uns am Anfang unserer Bachelorarbeiten kennen gelernt haben und seitdem nicht nur zusammen Arbeiten. Aus endlosen Abenden im Mohren mit Kränzen voll Kölsch wurden nun Footballabende an jedem verdammten Sonntag auf unserer Couch sowie tolle Laufevents. Torsten, trotz dem, dass wir uns nun schon ein paar Tage länger kennen, habe ich die intensive Zusammenarbeit speziell in diesem Jahr sehr genossen. Besonders entspannend sind unsere Mittagessen, die mir ermöglichem dem alltäglichen Mensatrott zu entkommen.

Nun ein großer Dank an alle good-old-Matterwaver und SYNQSler! Es ist toll, dass wir so ein verschworener Haufen waren und sind. Wir hatten so viele unvergessliche (oder schon am nächsten Morgen vergessene) Grillabende und Abschlussfeiern. Aber auch einfach für ein gemeinsames Abendessen und ein Spaß-Bier ist immer jemand zu finden.

Christiane und Dagmar, vielen Dank, dass ihr uns tagtäglich den Rücken frei haltet. Dadurch, dass alles Organisatorische und Bürokratische uns nur minimal berührt, erspart ihr uns viel Arbeit und Ärger.

Ich danke auch allen Geldgebern, die uns es ermöglichen Forschung zu betreiben. Insbesondere der HGSFP für das Stipendium während meines ersten Jahres und dem SFB ISOQUANT für die vielfältigen Möglichkeiten im YRC. Hier geht auch ein großer Dank an Tina für die tolle Orga! STRUCTURES danke ich für den Travel fund, der mir meine spontane USA Reise kurz vor der Abgabe ermöglicht hat. Außerdem war es mir möglich, spannende Konferenzen und Schulen zu besuchen, bei denen ich viele interessante Leute kennenlernen durfte.

Nicht nur meine Kollegen haben die letzten Jahre zu ganz besonderen gemacht. Schon während meines Studiums hatte ich das Glück, einige tolle Leute kennen zu lernen: Der ganzen Bande um Nils und Tanja, Katrin, Jonathan, dem Dicken Nils, Alex, Daniel, Marius und Fabi danke ich für viele unvergessliche Geschichten. Auch wenn ihr alle nicht mehr in HD seid, freue ich mich immer wieder euch zu sehen und tolle Zeiten zu haben!

Ein Dank geht auch an alle, die das (fast tägliche) Triathlontraining zu Spaß zweiter Ordnung machen!

Und dann sind da noch Moritz, Kevin, Dennis, Benne und Jan. Euch kenne ich schon so lange und trotzdem passt es bei uns noch so gut, wenn wir uns sehen! Sei es beim Besuch von einer Rekordanzahl an Cafes an zwei Tagen in Berlin, dem Kickern in der Krone oder dem Fifa Abend - bei dem ich chancenlos bin.

Ein großer Dank gebührt wohl meinen Eltern. Sie haben mich immer so sein lassen, wie ich bin und mich in meinem Tun unterstützt. Mama und Uwe, Papa und Eva - vielen Dank für alles! Ich bin auch stolz so tolle Großeltern zu haben!

Schlussendlich möchte ich Mareike danken. Sie ist meine Frau, Freundin, Coach und viele andere Dinge gleichzeitig. Ich bin stolz, dass wir so ein tolles Team sind :)

“Was da so ab und zu zwischen uns läuft,
ist wirklich schwer zu beschreiben in einem Text.
Nur wer bei deinem Blick mal kurz zwischen den Zeilen liest
Ist völlig hin, hin und weg und perplex”
Clueso Fanpost